Check for updates

ADVANCED SUSTAINABLE SYSTEMS
www.advsustainsys.com

Advancing Photocatalysis: Insights from 2D Materials and Operational Parameters for Organic Pollutants Removal

*Bachir Yaou Balarabe and Timur Sh. Atabaev**

Photocatalysis plays a crucial role in tackling environmental challenges by efficiently breaking down organic pollutants in water. This study highlights the significant contribution of 2D materials in advancing photocatalytic technology for sustainable environmental remediation. It explores various aspects of photocatalytic processes, including important performance metrics such as reaction rate, quantum yield, space yield, energy consumption, and figure of merit. The main focus is on 2D materials-based structures, such as metal oxide supported on graphene and graphene oxides, MXene, or MoS_2 (referred as 2D-MO NPs), as well as more complex nanocomposite configurations (referred as 2D-MO NCs). Furthermore, the research examines the complex interaction between compositional and operational factors that influence photocatalytic activity, as well as different photocatalytic mechanisms and active species. Finally, it addresses the current limitations of photocatalytic organic pollutants degradation for field applications and discusses the prospects of this technology.

1. Introduction

Due to industrial growth and higher living standards, organic pollutants, such as dyes and pharmaceuticals, have become significant environmental threats in recent decades.[1–5] These pollutants persist in the environment, disrupt ecosystems, and pose health risks to humans and wildlife, causing irreversible harm to aquatic species.[6–10] Various decomposition methods have been implemented to convert these pollutants into harmless substances to mitigate these concerns. Techniques including biodegradation, electrochemical processes, adsorption, and chemical oxidation have been extensively utilized.[11–14] Among these, photocatalytic methods stand out because of their green chemistry, cost-effectiveness, and safety. This approach is considered a key sustainable technology for the future and is part of the advanced oxidative processes.[15–20] The innovative use of renewable resources to treat water pollution is demonstrated using semiconductor-based photocatalysts and light-driven materials for water purification.[21–27] Semiconductor metal oxides, such as CuO, TiO_2, ZnO, Fe_2O_3, and many others, have been extensively studied since groundbreaking work of Fujishima et al. in 1972.[28–33] These metal oxides possess versatile physicochemical properties and offer a pathway for sustainable and clean ecosystems. However, the effectiveness of these metal oxides in removing organic pollutants is hindered by certain limitations, such as wide bandgaps and low conductivity.[26,27,34,35] Improving the performance of these metal oxides can be accomplished through two primary strategies: inhibiting the recombination of photoinduced positive holes and electrons to facilitate redox reactions and hydroxyl radical generation and narrowing the bandgap to increase visible light absorption and harness a wider solar spectrum.[17,36–40] Given that the solar spectrum primarily comprises infrared and visible light, with only a minor fraction attributed to ultraviolet light, enhancing the absorption of visible light plays a crucial role in optimizing photocatalytic performance.[41] Researchers have investigated various methods to enhance the effectiveness of metal oxides in photocatalysis. The discovery of exceptional properties of graphene in 2004 was a significant scientific breakthrough and led to exploration of 2D materials applications in photocatalysis, electrocatalysis, lithium-ion batteries, supercapacitors, and electrical devices.[42–46] Researchers have increasingly focused on a range of 2D materials due to their promising capabilities in degrading organic pollutants. Among these materials are hexagonal boron nitride (h-BN),[47] transition metal dichalcogenides such as WS_2 and WSe_2,[48] graphitic carbon nitride (g-C_3N_4),[49] bismuth oxychloride (BiOCl),[50–52] black phosphorus (BP),[53] and molybdenum ditelluride ($MoTe_2$).[54] These materials excel in photocatalysis owing to their adjustable bandgaps, large surface areas, and efficient charge transport. They generate reactive oxygen species under light and effectively remove organic compounds for environmental remediation. Their performance can be improved through structural modifications or material integration, advancing pollution control efforts.[55] Further exploration of 2D materials has included molybdenum disulfide (MoS_2), which has a similar 2D structure as graphene but has improved catalytic activity along its edges. This characteristic significantly enhances the photocatalytic performance of metal oxide such as TiO_2 by increasing the number of active surface sites and allowing for faster separation of charge carriers within the metal oxide.[56]

B. Y. Balarabe, T. S. Atabaev
Department of Chemistry
School of Science and Technology
Nazarbayev University
Astana 010000, Kazakhstan
E-mail: timur.atabaev@nu.edu.kz

The ORCID identification number(s) for the author(s) of this article can be found under https://doi.org/10.1002/adsu.202400483

© 2024 The Author(s). Advanced Sustainable Systems published by Wiley-VCH GmbH. This is an open access article under the terms of the Creative Commons Attribution-NonCommercial-NoDerivs License, which permits use and distribution in any medium, provided the original work is properly cited, the use is non-commercial and no modifications or adaptations are made.

DOI: 10.1002/adsu.202400483

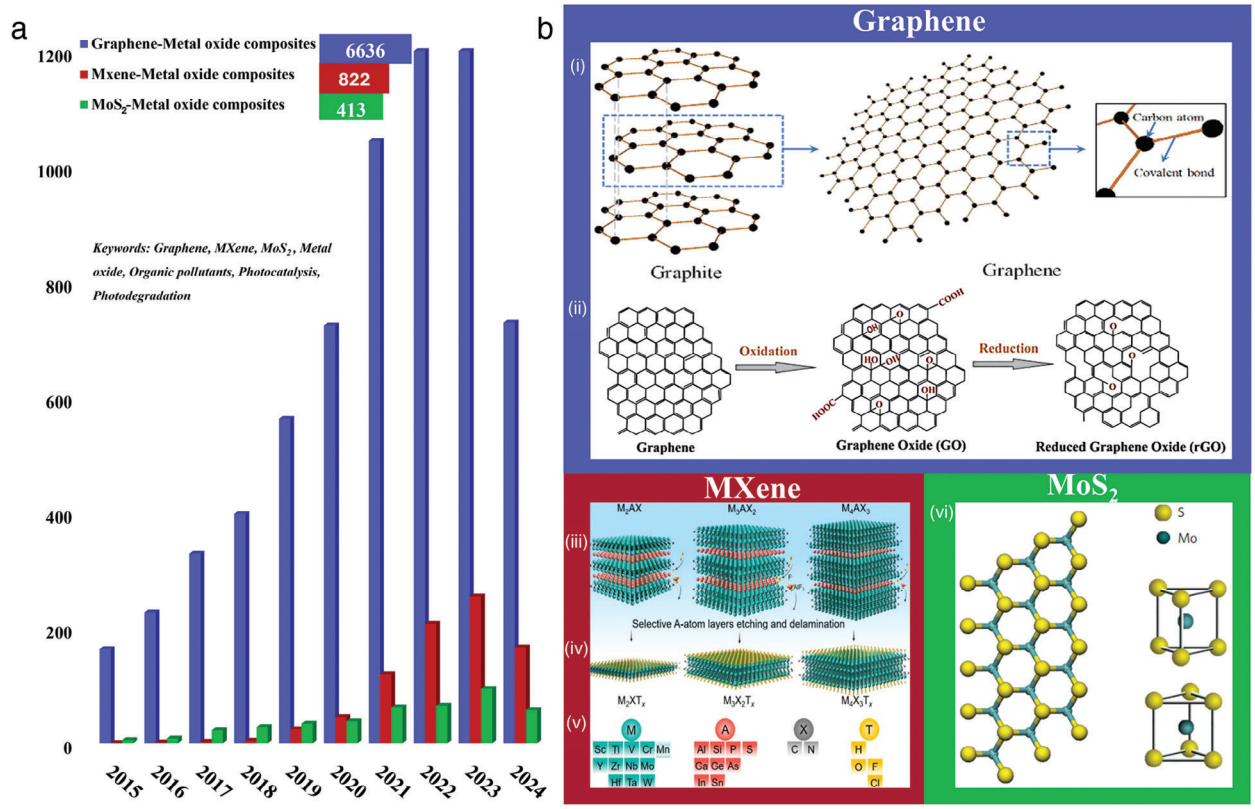

Figure 1. a) Graphene, MXene, and MoS_2 metal oxide composite publications: a decadal analysis (2015–2024). b) (i) Structural representation of graphene. Reproduced under the term of the CC-BY license.[67] Copyright 2023, MDPI. (ii) Structural dynamics of graphene-based materials—graphene, graphene oxide (GO), and reduced graphene oxide (rGO). Reproduced with permission.[71] Copyright 2021, RSC. Overview of MXene precursors and synthesis: (iii) three mono-M MAX phase structures (M_2AX, M_3AX_2, and M_4AX_3) and selective etching of A-group layers (depicted in red). (iv) Formation of MXenes postselective etching and surface terminations (illustrated in yellow) labeled as T. (v) Potential elements for M, A, X, and T in the MAX and MXene phases. Reproduced with permission.[101] Copyright 2020, Springer. (vi) Monolayer and bulk unit cell structures of MoS_2, highlighting spatial inversion symmetry break in monolayers; left: monolayer and right: bulk unit cell. Reproduced with permission.[106] Copyright 2012, Nature.

In 2011, significant advances occurred with the discovery of MXene, a transition metal carbide, nitride, and carbonitride. MXene quickly became a focus of study in the field of photocatalysts because of its three important features: abundant functional groups resulting from the wet chemical etching process, the ability to modify its bandgap through surface chemistry, and enhanced conductivity provided by its conductive metal cores.[57–59] As a result, MXene has established itself as a competitive material in 2D photocatalysts, particularly in pollutant degradation.[60–62] MXene exhibits exceptional electrical conductivity owing to electron confinement, which improves photocatalysis by aiding charge separation. Their large surface area is ideal for preventing catalyst growth and aggregation. Significant progress has been made in the past year in removing organic pollutants using metal oxide-supported 2D materials. A review of relevant works from scientific literature between 2015 and 2024 identified 7871 publications. It is important to note that although graphene is a pioneering material, ongoing research interest remains high, as shown in **Figure** 1a. Following graphene, MXene emerged, followed by MoS_2. This sequence demonstrates the continued curiosity and investigation of these materials. Thus, this review thoroughly examines and compares the photocatalytic performances of metal oxide-supported graphene, MXene, MoS_2, and their composites in the degradation of organic pollutants. Moreover, it comprehensively explores the morphological evolution of these metal oxides, describes their synthesis methods, analyses the key factors influencing the photocatalytic removal of organic pollutants, and explains the complex mechanisms that drive this degradation process. Thus, this study addresses the United Nations' Sustainable Development Goal # 6 (Clean Water and Sanitation).

2. 2D Materials

2.1. Graphene

Graphene, with its unique 2D hexagonal lattice of sp^2-bonded carbon atoms, has revolutionized various fields such as electronics, energy, and materials science. This is primarily due to its extraordinary properties, including an impressive theoretical specific surface area that exceeds 2600 $m^2\ g^{-1}$.[63–66] Pure graphene and its derivatives, such as graphene oxide, reduced graphene oxide, and graphene nanosheets, have been widely studied. Graphite, commonly used as the starting material for graphene synthesis, comprises stacked graphene layers tightly bonded to form a carbon lattice (Figure 1b(i)). The weak van

© 2024 The Author(s). Advanced Sustainable Systems published by Wiley-VCH GmbH

23667486, 2024, 12, Downloaded from https://advanced.onlinelibrary.wiley.com/doi/10.1002/adsu.202400483 by Nazarbayev University, Wiley Online Library on [08/07/2025]. See the Terms and Conditions (https://onlinelibrary.wiley.com/terms-and-conditions) on Wiley Online Library for rules of use; OA articles are governed by the applicable Creative Commons License

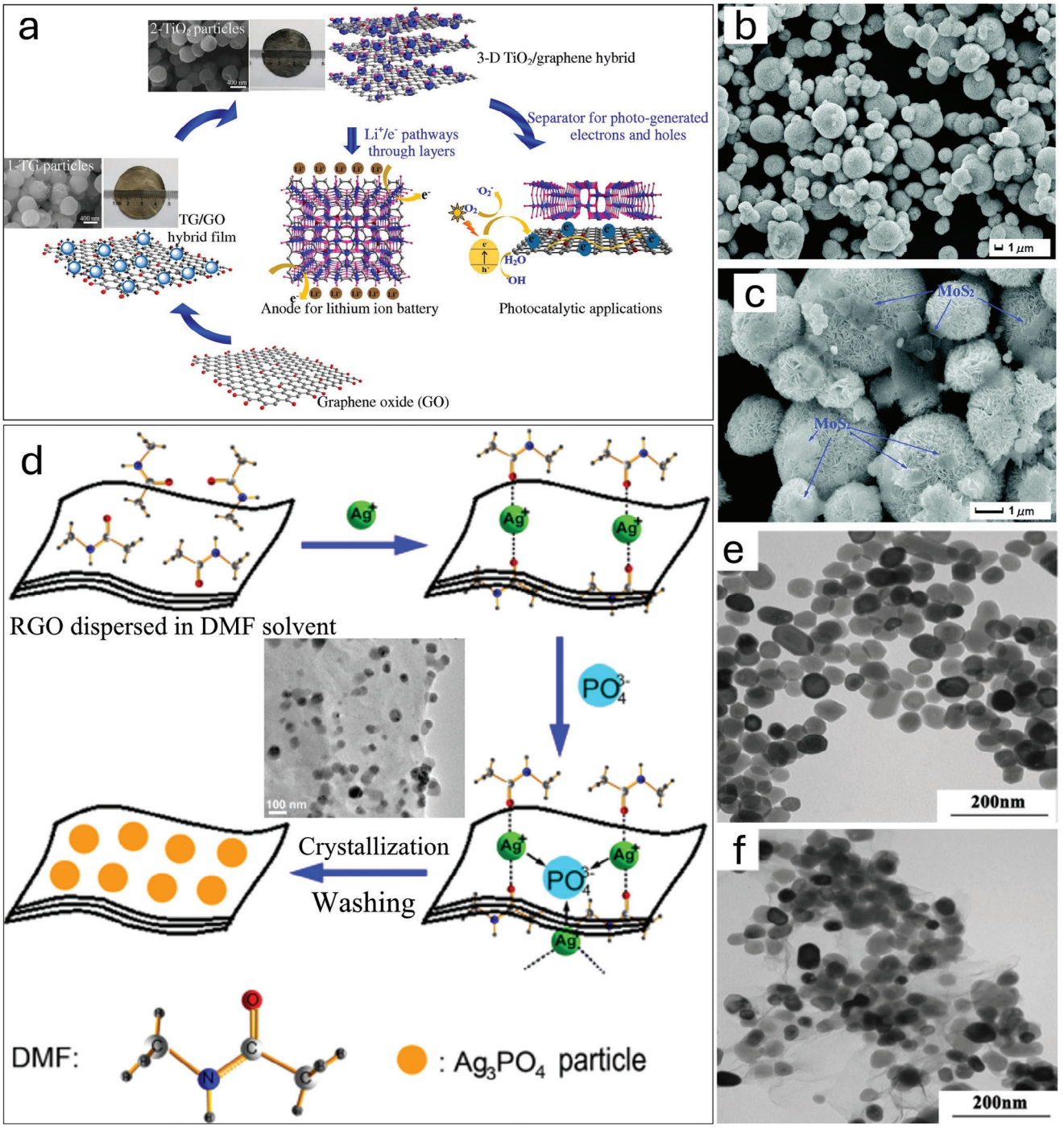

Figure 2. a) Graphic representation: self-assembly and functionalities of TiO_2/GR hybrid systems. Reproduced with permission.[160] Copyright 2018, Elsevier. SEM images of MoS_2/BiOBr sphere-like structures: b) low magnification view, and c) top view. Reproduced with permission.[154] Copyright 2014, RSC. d) Procedure for synthesizing Ag_3PO_4/rGO nanocomposite. Inset: TEM image of Ag_3PO_4/rGO. Reproduced with permission.[145] Copyright 2013, Elsevier. e,f) TEM images of ZnO and Ag–ZnO/rGO nanocomposites, respectively. Reproduced with permission.[161] Copyright 2018, Springer.

der Waals forces hold these layers together. When graphene is isolated into a single layer, it becomes an ultrathin material that is only one atom thick.[67] This transformation highlights graphene's exceptional mechanical, electrical, and thermal properties, broadening its potential for environmental applications. For example, graphene can be used in advanced oxidation processes to decompose dyes in wastewater treatment.[68,69] Graphene oxide (GO) is a significant variation of graphene and is synthesized using Hummers' method (Figure 1b(ii)). This method causes oxidation and reduction, resulting in a decrease

© 2024 The Author(s). Advanced Sustainable Systems published by Wiley-VCH GmbH

23667486, 2024, 12, Downloaded from https://advanced.onlinelibrary.wiley.com/doi/10.1002/adsu.202400483 by Nazarbayev University, Wiley Online Library on [08/07/2025]. See the Terms and Conditions (https://onlinelibrary.wiley.com/terms-and-conditions) on Wiley Online Library for rules of use; OA articles are governed by the applicable Creative Commons License

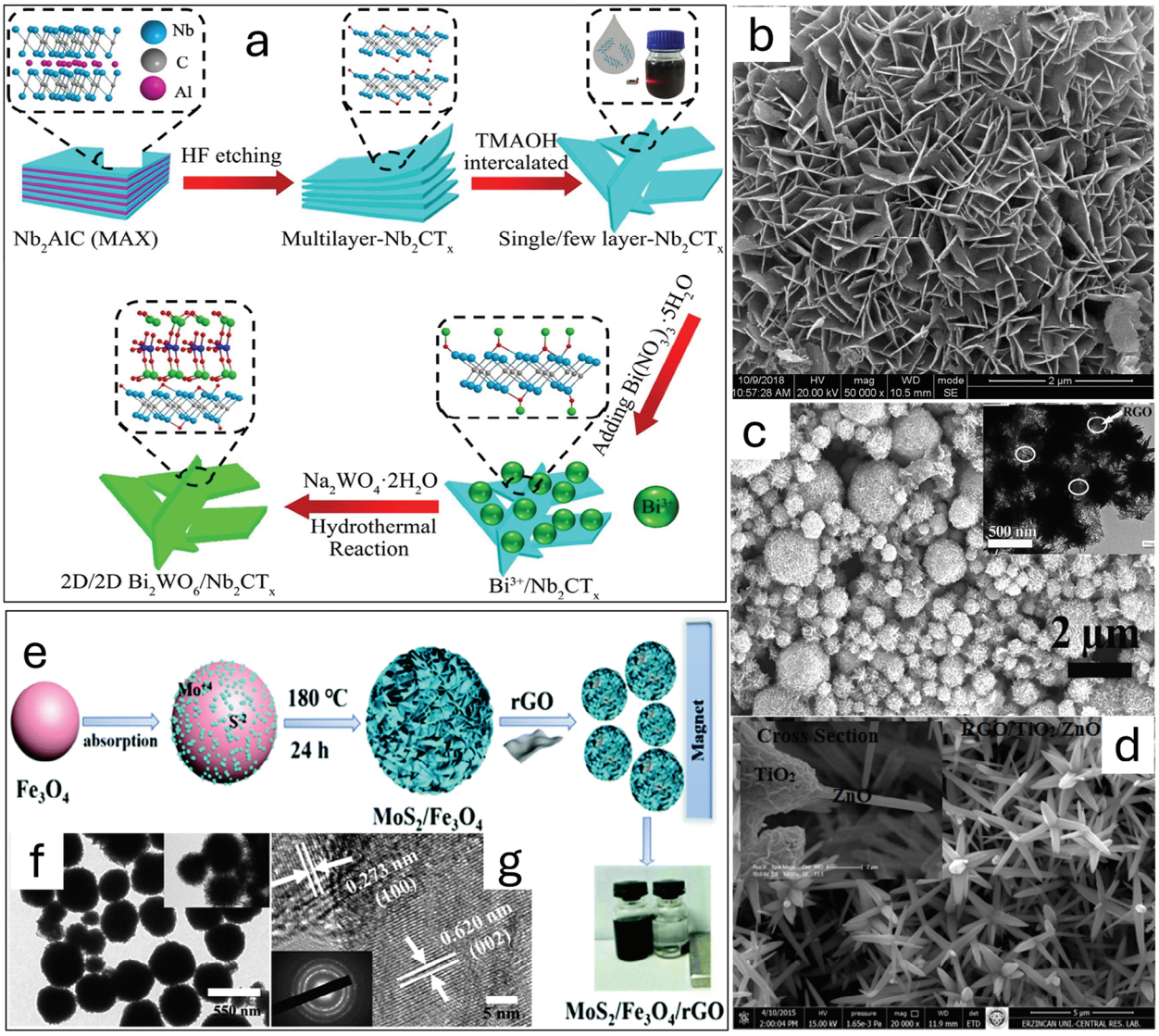

Figure 3. a,b) Synthesis of 2D/2D Bi_2WO_6/Nb_2CT_x flower-like structure and SEM image. Reproduced with permission.[162] Copyright 2020, Elsevier. c) SEM image of WO_3@rGO nanoflower, (inset) TEM image. Reproduced with permission.[163] Copyright 2016, Elsevier. d) SEM image displaying the flower-like structure of ZnO within the rGO/TiO_2/ZnO nanostructure Reproduced with permission.[164] Copyright 2018, Elsevier. e–g) Experimental setup and TEM images at low and high MoS_2/Fe_3O_4/rGO magnifications, respectively. Reproduced with permission.[166] Copyright 2018, RSC.

in electrical and thermal conductivities. Nonetheless, the properties of GO can be reinstated to mimic graphene by reducing it, leading to the formation of reduced graphene oxide (rGO).[70,71] Enhancing graphene oxide's conductivity through oxidation and reduction methods has opened new possibilities in optoelectronics, mechanical engineering, biomedicine, and sensing applications. Integrating GO with metal oxides in nanocomposites is also valuable for photocatalytic applications, particularly in water treatment. These composites offer high efficiency, stability, and magnetic recoverability, making them ideal for such uses. However, challenges such as production expenses, nanoparticle clumping, environmental concerns, and scalability must be addressed. Current research is dedicated to refining these materials to effectively control water pollution on a broader scale.[72–77]

2.2. MXene

MXenes are a class of 2D transition-metal carbides or carbonitrides. These materials are synthesized by selectively etching specific atomic layers from parent MAX phases through the use of hydrofluoric acid or a combination of hydrochloric acid (HCl) with sodium fluoride (NaF), lithium fluoride (LiF), or ammonium fluoride (NH_4F).[78–80] MXenes possess the structural formula $M_{n+1}X_nT_x$, where the early transition metals titanium (Ti), vanadium (V), zirconium (Zr), and niobium (Nb) are combined with carbon and/or nitrogen. Furthermore, they exhibit surface functional groups such as —O, —OH, and —F.[81,82] Based on the atomic layer numbers, MXenes display the characteristic structures of M_2XT_x, $M_3X_2T_x$, and $M_4X_3T_x$. Initially investigated for energy conversion and storage applications, MX-

© 2024 The Author(s). Advanced Sustainable Systems published by Wiley-VCH GmbH

23667486, 2024, 12, Downloaded from https://advanced.onlinelibrary.wiley.com/doi/10.1002/adsu.202400483 by Nazarbayev University, Wiley Online Library on [08/07/2025]. See the Terms and Conditions (https://onlinelibrary.wiley.com/terms-and-conditions) on Wiley Online Library for rules of use; OA articles are governed by the applicable Creative Commons License

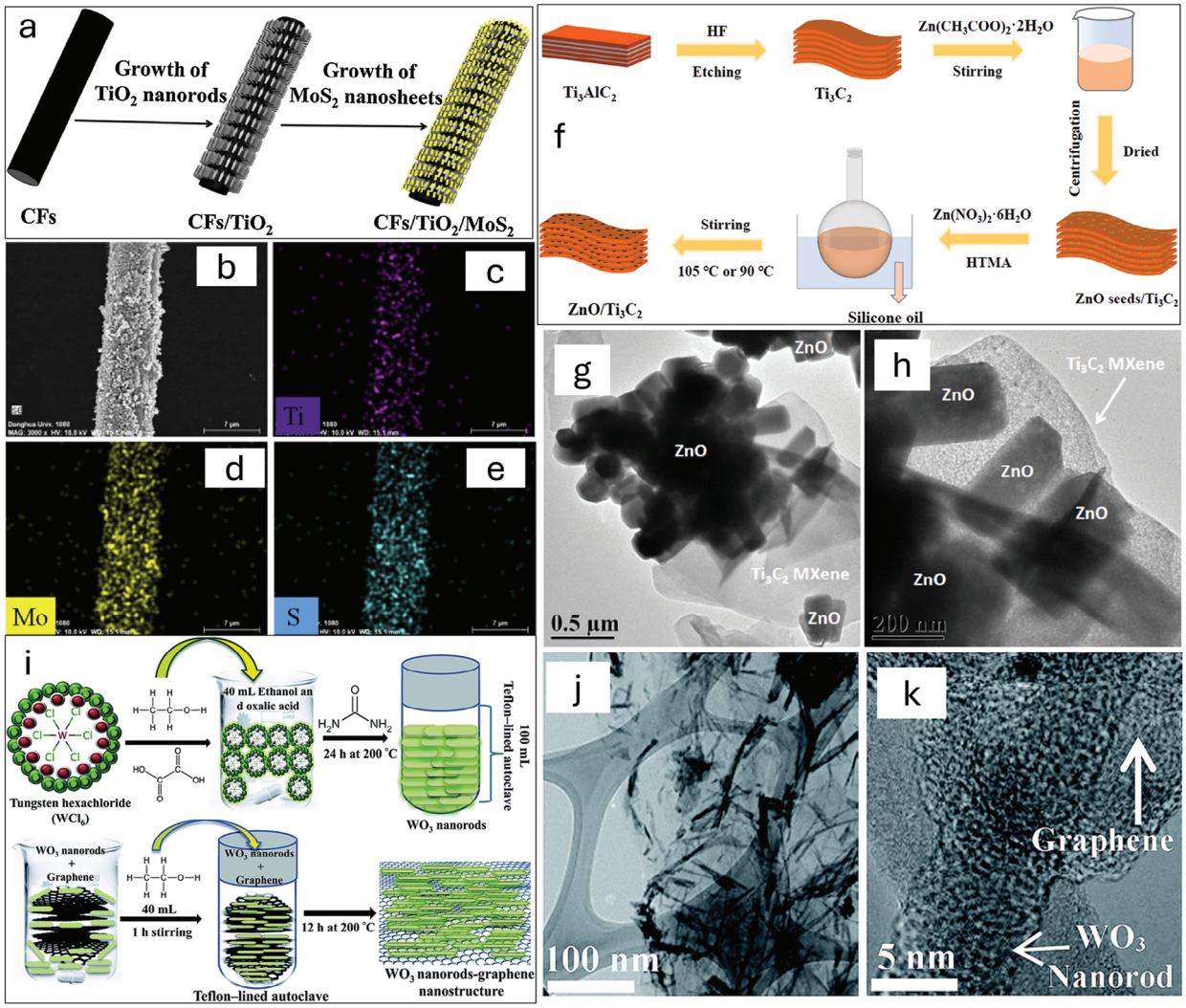

Figure 4. a) $CFs/TiO_2/MoS_2$ nanostructures synthesis, and b–e) mapping images of $CFs/TiO_2/MoS_2$ nanocomposites. Reproduced with permission.[171] Copyright 2019, Elsevier. f) ZnO microrods/MXene synthesis procedure, and g,h) TEM images of the ZnO microrods/MXene nanostructures. Reproduced with permission.[180] Copyright 2021, Elsevier. i) WO_3 nanorods–graphene nanostructure schematic representation and j,k) different scale TEM images. Reproduced with permission.[178] Copyright 2016, RSC.

enes have garnered interest in photocatalysis owing to their plentiful functional groups, adjustable bandgap, and metallic conductivity.[83–85] MXenes have many applications in multiple fields, including water splitting, CO_2 reduction, pollutant degradation, and N_2 fixation. They significantly enhance photocatalytic activity through several mechanisms, such as facilitating charge carrier separation, providing structural support, controlling catalyst size, and improving reactant adsorption.[86–89] Although MXenes are primarily recognized as photogenerated electron acceptors, their role in photocatalysis extends beyond this function due to their high specific surface area and surface chemistry.[90–92] MAX phases comprise $M_{n+1}X_n$ atomic layers bonded to A-group elements from groups 13 to 16 in the periodic table. Figure 1b(i) shows three structures: M_2AX, M_3AX_2, and M_4AX_3.[93] In addition to primary M–A bonds, selective chemical etching of the A elements allows for delamination of the $M_{n+1}X_n$ layers without disrupting the M–X bonds. This removes the A-group layers and exposes the transition metals in $M_{n+1}X_n$, which are then terminated by surface functional groups (T_x). This leads to the formation of $M_{n+1}X_nT_x$ (Figure 1b(ii). The nature of these surface terminations varies depending on factors such as etching differences, post-treatment chemistry, and specific transition metals. Notably, the composition of MXenes derived from MAX phase precursors exhibits some variability. For a comprehensive list of elements relevant to M, X, T, and select A-group elements of MAX phases (Figure 1b(iii).[94–101]

2.3. MoS_2

MoS_2 has attracted significant attention because of its hexagonal lattice structure, which resembles graphene with a promising applicability in many fields.[102,103] The intricate crystal structure of MoS_2, depicted in Figure 1b(vi), consists of S–Mo–S

© 2024 The Author(s). Advanced Sustainable Systems published by Wiley-VCH GmbH

23667486, 2024, 12, Downloaded from https://advanced.onlinelibrary.wiley.com/doi/10.1002/adsu.202400483 by Nazarbayev University, Wiley Online Library on [08/07/2025]. See the Terms and Conditions (https://onlinelibrary.wiley.com/terms-and-conditions) on Wiley Online Library for rules of use; OA articles are governed by the applicable Creative Commons License

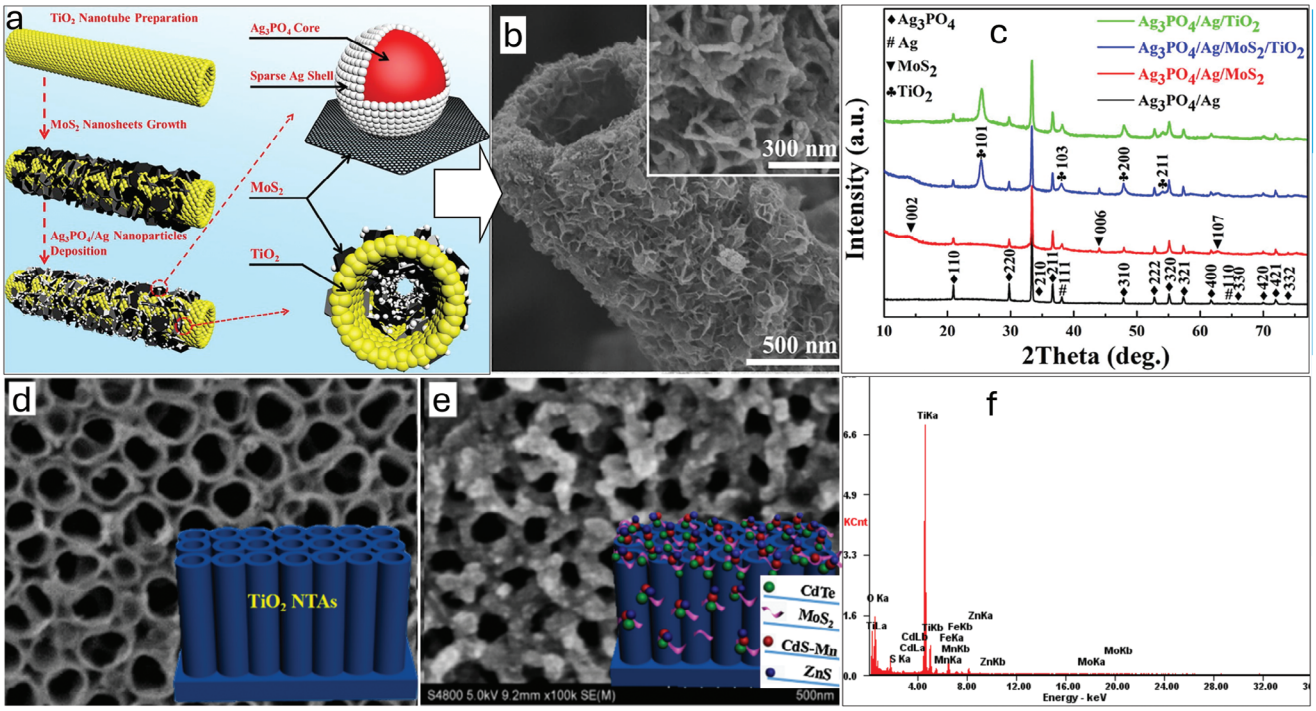

Figure 5. a) Schematic formation, b) SEM image and c) XRD pattern of the $Ag_3PO_4/Ag/MoS_2/TiO_2$ nanoheterojunction. Reproduced with permission.[181] Copyright 2018, Elsevier. d,e) SEM images of TiO_2 nanotube arrays and CdSMn/MoS2/CdTe/TiO2 composite with schematic representations (inset). f) EDX analysis of $CdS–Mn/MoS_2/CdTe/TiO_2$ composite. Reproduced with permission.[182] Copyright 2016, Elsevier.

layers stabilized by covalent bonds and van der Waals forces. This arrangement offers a complex terrain for both challenges and opportunities.[104–106] Despite the indirect bandgap of MoS_2 in its bulk form, integrating its 2D nanosheets into heterostructures with materials such as graphene has demonstrated significant potential as photocatalysts.[107] A range of methodologies, such as mechanical and chemical exfoliation,[108–110] chemical vapor deposition,[111–114] and hydrothermal and solvothermal techniques,[115–119] have been extensively employed for the synthesis of MoS_2, each possessing unique advantages and limitations. However, MoS_2 encounters various challenges as a photocatalyst, including a restricted solvent-accessible surface area, accelerated carrier recombination rates, and susceptibility to degradation. Researchers have conducted extensive investigations into multiple techniques to address these obstacles comprehensively. These techniques include creating heterocomposites, integrating metallic oxides, utilizing cocatalysts, designing core/shell structures, and implementing nonmetal doping. The primary objective of these strategies is to improve the photocatalytic efficiency and durability of MoS_2, thereby expanding its potential applications within the domain of photocatalysis.[120]

3. Metal Oxide Structures with Controlled Morphologies Coupled to 2D Nanostructures

Research on 2D metal oxide nanostructures is highly significant in materials science due to their unique properties and wide range of applications.[121] In synthesizing these materials, the morphology can be manipulated, which enables the modification of physical attributes, such as dimensions, configuration, and constitution. This ultimately enhances their functional properties.[122] Achieving consistent morphology remains a challenge despite the availability of these opportunities. Studies have shown that incorporating materials, such as ZnO, Ag_2WO_4, and TiO_2, into composites with MoS_2, Ti_3C_2, and graphene results in irregular morphologies. However, these composites consistently exhibit improved photocatalytic activity in degrading various pollutants, such as methylene blue, tetracycline hydrochloride, and phenol.[123–125] Over the past decade, significant progress has been made in the deliberate fabrication of composite materials employing 2D substances, such as graphene, MXene, and MoS_2. These nanomaterials demonstrated a remarkable enhancement in their overall functionality.

3.1. Spherical Structures

Extensive research has been conducted on 2D materials supported by well-designed spherical metal oxide nanoparticles. These nanoparticles include materials such as TiO_2,[126–131] ZnO,[132–138] $CoFe_2O_4$,[139,140] Ag_3PO_4,[141–145] CoO,[146] Fe_3O_4,[147,148] $MgFe_2O_4$,[149] $MnFe_2O_4$,[150] $NiCo_2O_4$,[151] ZrO_2,[152] Ag_2VO_4,[153] BiOBr,[154,155] $NiFe_2O_4$,[156] CuO,[157] $BiVO_4$,[158] and CeO_2[159] among others. These nanocomposites have significant potential for photocatalytic removal of organic pollutants owing to their distinct structural and synergistic properties. For instance, synthesizing TiO_2/graphene hybrids involved the initial preparation of graphene oxide via a suspension and dialysis process. The next step involved mixing tetrabutyl titanate with ethylene glycol and acetone to produce TiO_2/graphene (TG).

© 2024 The Author(s). Advanced Sustainable Systems published by Wiley-VCH GmbH

23667486, 2024, 12, Downloaded from https://advanced.onlinelibrary.wiley.com/doi/10.1002/adsu.202400483 by Nazarbayev University, Wiley Online Library on [08/07/2025]. See the Terms and Conditions (https://onlinelibrary.wiley.com/terms-and-conditions) on Wiley Online Library for rules of use; OA articles are governed by the applicable Creative Commons License

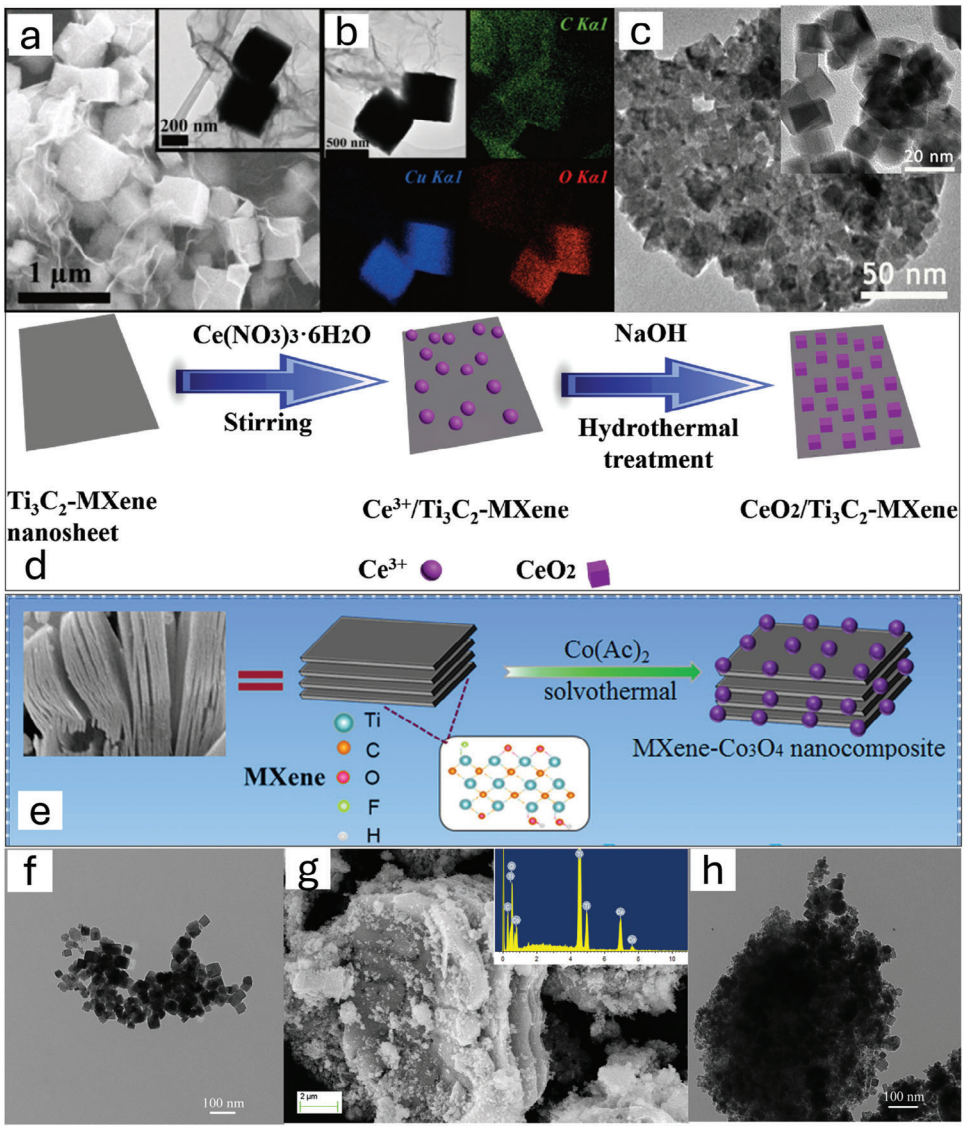

Figure 6. Cu_2O–rGO nanocomposites were examined using a) SEM and TEM (inset) imaging and b) elemental mapping with TEM-EDS analysis. Reproduced with permission.[185] Copyright 2017, Elsevier. c,d) TEM imaging and synthesis of CeO_2/MXene composites. Reproduced with permission.[186] Copyright 2019, Elsevier. e) Schematic synthesis of MXene–Co_3O_4 nanocomposites. f) TEM image of Co_3O_4 small cube. g,h) SEM and TEM images of the MXene–Co_3O_4 nanocomposites. Reproduced with permission.[187] Copyright 2019, ACS Omega.

TG was then combined with graphene oxide to form a film, which was subsequently treated with hydrazine hydrate to obtain TiO_2/GR hybrids, as shown in **Figure 2a**.[160] Furthermore, in synthesizing the MoS_2/BiOBr composites, MoS_2 was added to an ethylene glycol solution containing the ionic liquid C16mimBr. This solution was then reacted with $Bi(NO_3)_3{\cdot}5H_2O$ in a Teflon-lined autoclave, resulting in the sphere-like shape of the particles (Figure 2b,c).[154] Similarly, the synthesis of Ag_3PO_4/rGO sheet nanocomposites involved the dispersion of rGO in a solvent, followed by adding $AgNO_3$. Subsequently, H_3PO_4 was introduced under stirring, as depicted in Figure 2d.[145] The spherical ZnO structure in Figure 2e,f within the Ag–ZnO/rGO nanocomposites was achieved step-by-step. Zinc acetate, GO, and silver nitrate were initially combined with ethylene glycol and stirred at 70 °C. This mixture was then ultrasonicated for 2 h. Then, sodium hydroxide was added, and the mixture was autoclaved at 160 °C for 20 h.[161]

3.2. Flower-Like Structures

The synthesis methods for flower-morphology nanocomposites vary depending on the constituent materials. Bi_2WO_6/Nb_2CT_x nanosheets were synthesized by dissolving Nb_2AlC in a hydrogen fluoride solution and then dispersing it in tetramethylammonium hydroxide to obtain Nb_2CT_x nanosheets. These nanosheets were then mixed with solutions containing sodium tungstate dihydrate ($Na_2WO_4{\cdot}2H_2O$), bismuth nitrate pentahydrate ($Bi(NO_3)_3{\cdot}5H_2O$), and cetyltrimethylammonium bromide (CTAB), followed by autoclave treatment (**Figure 3a,b**).[162]

© 2024 The Author(s). Advanced Sustainable Systems published by Wiley-VCH GmbH

23667486, 2024, 12, Downloaded from https://advanced.onlinelibrary.wiley.com/doi/10.1002/adsu.202400483 by Nazarbayev University, Wiley Online Library on [08/07/2025]. See the Terms and Conditions (https://onlinelibrary.wiley.com/terms-and-conditions) on Wiley Online Library for rules of use; OA articles are governed by the applicable Creative Commons License

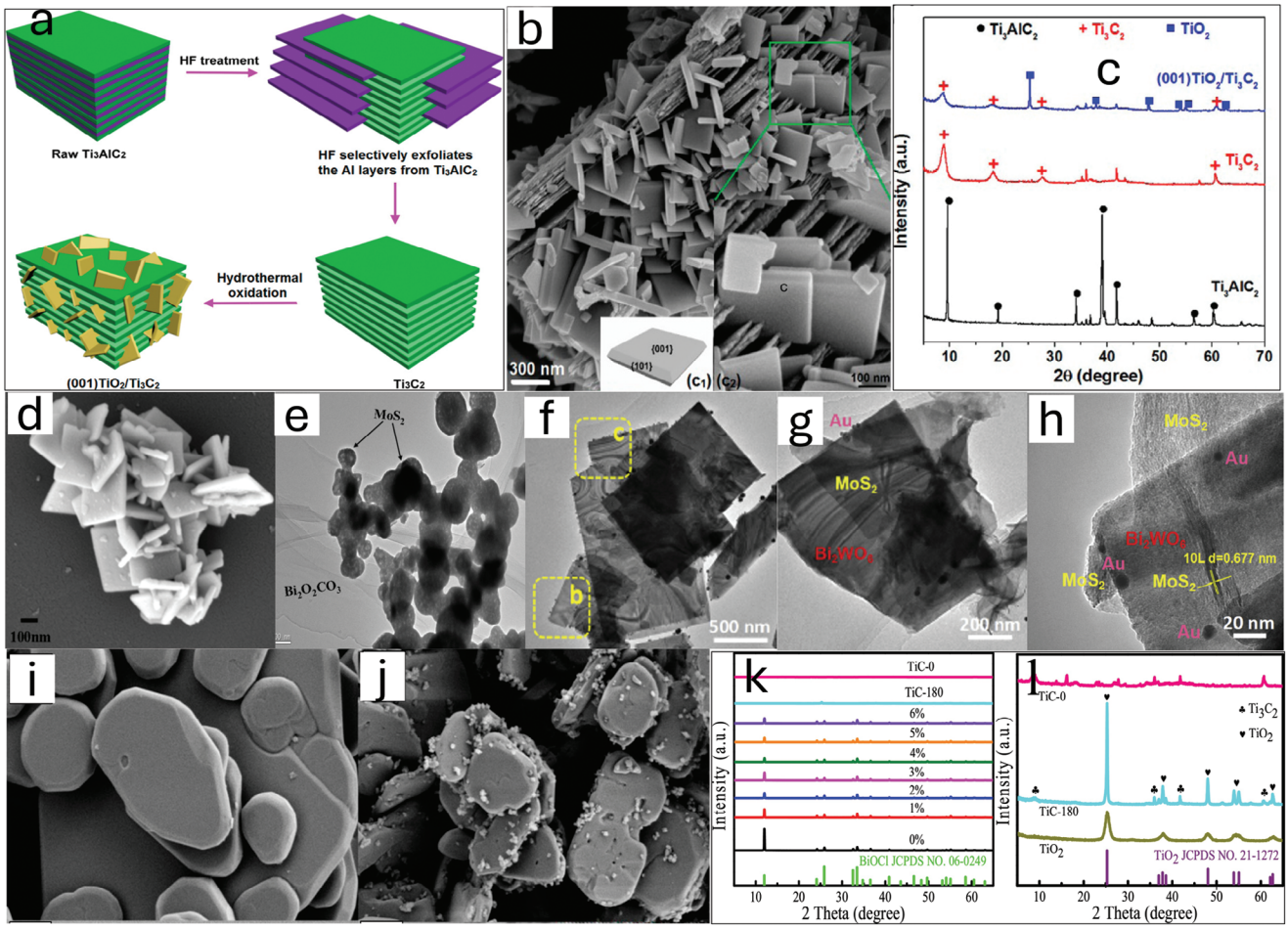

Figure 7. a–c) Schematic exfoliation of Ti_3AlC_2 and (001)TiO_2/Ti_3C_2 hybrid formation, along with FESEM image and corresponding XRD analysis. Reproduced with permission.[188] Copyright 2016, American Chemical Society. d,e) SEM and TEM images of $Bi_2O_2CO_3$ in $MoS_2/Bi_2O_2CO_3$ composites. Reproduced with permission.[199] Copyright 2014, Elsevier. f,g) TEM images of Au/Bi_2WO_6 and Au/Bi_2WO_6–MoS_2 nanocomposites, and h) HRTEM image of Au/Bi_2WO_6–MoS_2 nanocomposites. Reproduced with permission.[200] Copyright 2020, Elsevier. i) BiOCl and j) Ti_3C_2/TiO_2/BiOCl SEM images and k,l) XRD patterns corresponding to these materials. Reproduced with permission.[62] Copyright 2020, Elsevier.

Conversely, the WO_3@rGO flower nanostructure was prepared via a one-step hydrothermal reaction. Initially, a suspension of graphene oxide was combined with tungstic acid and hydrogen peroxide to produce a colloidal solution, which was subsequently subjected to a heating process at 180 °C for 12 h to facilitate the formation of the composites (Figure 3c).[163] The synthesis of the hybrid nanostructure on an FTO substrate involved three essential stages: the application of rGO, hydrothermal synthesis for mesoporous TiO_2, and the promotion of ZnO nanostructure growth within the TiO_2 matrix. These steps aimed to enhance stability and optimize electron transport through controlled growth (Figure 3d).[164] Similarly, a hydrothermal synthesis method produced Fe-doped ZnO nanoparticles with a flower-like morphology. Subsequently, a MoS_2–FeZnO nanocomposite was fabricated by combining the Fe-doped ZnO nanoparticles with different weight ratios of MoS_2/FeZnO.[165] The MoS_2/Fe_3O_4/rGO composite resembling a flower was synthesized through the sequential combination of Fe_3O_4 nanoparticles with Na_2MoO_4 and L-cysteine, followed by the addition of a suspension of rGO and subsequent execution of a hydrothermal reaction. A comprehensive depiction of the procedure can be found in Figure 3e, while the resulting morphology and the HRTEM analysis are illustrated in Figure 3f,g.[166]

3.3. Rods-Like Structures

The synthesis of rod-shaped nanomaterials has attracted considerable attention in materials science and nanotechnology. Recent research has focused on combining metal oxide nanorods with 2D materials, specifically ZnO,[161,167–169] TiO_2,[136,170,171] Bi_2O_3,[172,173] SnO_2,[174] CeO_2,[174,175] Nb_2O_5,[176,177] and WO_3.[178,179] For instance, modifying carbon fibers (CFs) using a hydrothermal process to introduce TiO_2 nanorods. MoS_2 nanosheets are deposited hydrothermally onto the CFs/TiO_2 framework, as shown in **Figure 4a–e**.[171] Similarly, synthesizing composites consisting of ZnO microrods/MXene involved an initial step in preparing MXene through selective etching. Subsequently, the ZnO seeds were grown in ethanol and annealed with MXene in water (Figure 4f). This sequential

© 2024 The Author(s). Advanced Sustainable Systems published by Wiley-VCH GmbH

23667486, 2024, 12, Downloaded from https://advanced.onlinelibrary.wiley.com/doi/10.1002/adsu.202400483 by Nazarbayev University, Wiley Online Library on [08/07/2025]. See the Terms and Conditions (https://onlinelibrary.wiley.com/terms-and-conditions) on Wiley Online Library for rules of use; OA articles are governed by the applicable Creative Commons License

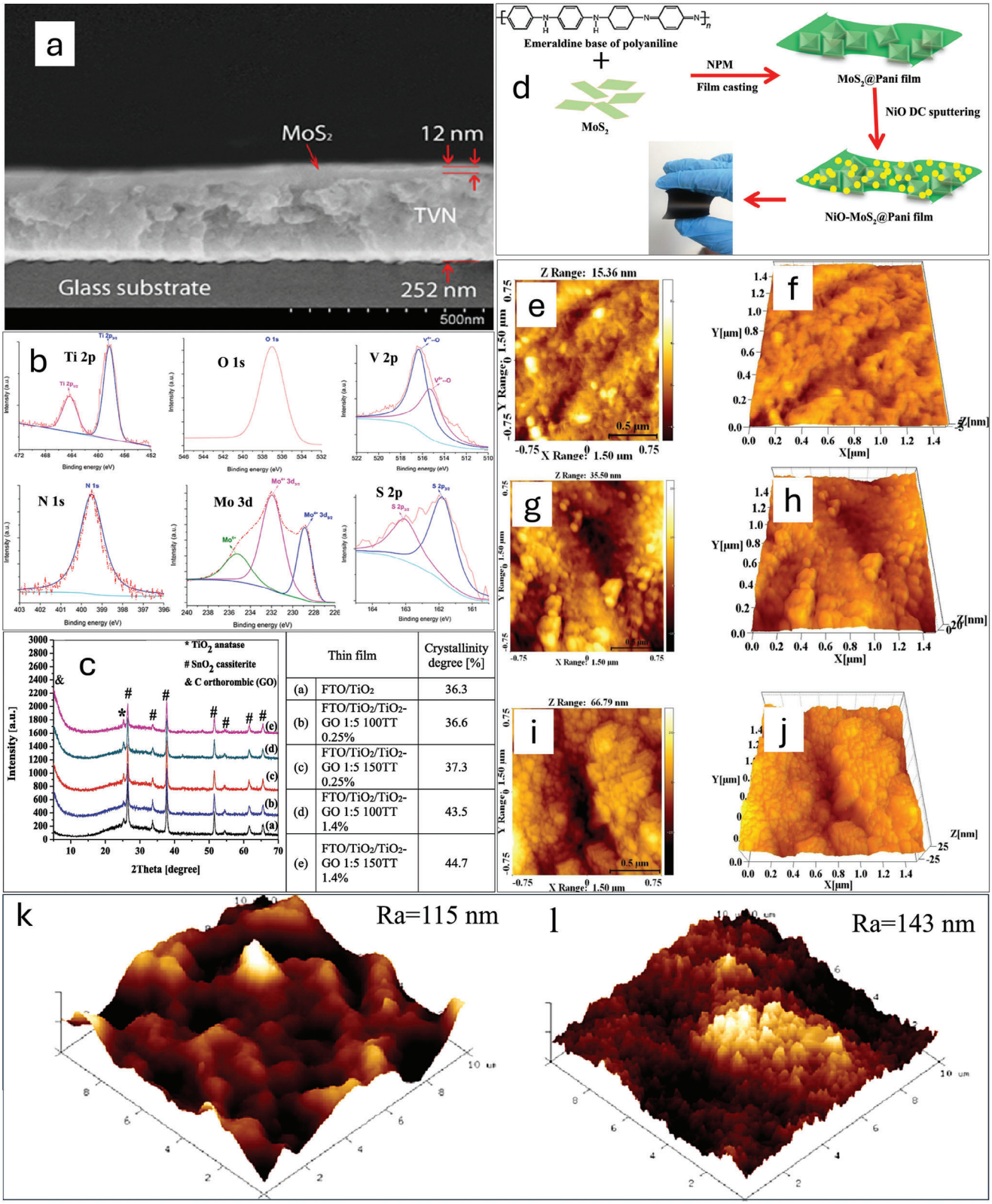

Figure 8. a) SEM images and b) XPS of MoS_2/V, N codoped TiO_2 45 thin films. Reproduced with permission.[201] Copyright 2018, Elsevier. c) XRD patterns of the thin films. Reproduced with permission.[202] Copyright 2021, Elsevier. d) Synthesis of NiOMoS_2@PANI nanocomposite films. AFM topographical images of: e,f) PANI, g,h) MoS_2@PANI, and i,j) NiO–MoS_2@PANI nanocomposite films. Reproduced with permission.[203] Copyright 2021, Elsevier. k,l) AFM images of MXene@PVDF and MXene–PVA–TiO_2@PVDF membranes. Reproduced with permission.[204] Copyright 2023, Elsevier.

© 2024 The Author(s). Advanced Sustainable Systems published by Wiley-VCH GmbH

23667486, 2024, 12, Downloaded from https://advanced.onlinelibrary.wiley.com/doi/10.1002/adsu.202400483 by Nazarbayev University, Wiley Online Library on [08/07/2025]. See the Terms and Conditions (https://onlinelibrary.wiley.com/terms-and-conditions) on Wiley Online Library for rules of use; OA articles are governed by the applicable Creative Commons License

Table 1. Different reported metal oxide structures on 2D materials.

No.	Metal oxide structure	Metal oxide	Composite material	Synthesis method	SEM/TEM images of the composite	Refs.
1	Wire	$Bi_{20}TiO_{32}$	rGO/$Bi_{20}TiO_{32}$	One-pot hydrothermal		[205]
2	Leaf-like lamellas	$BiVO_4$	$BiVO_4$–GR	Hydrothermal	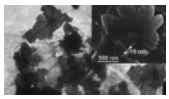	[206]
3	Octahedral	TiO_2	(111) TiO_2/Ti_3C_2	Hydrothermal	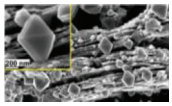	[207]
4	Hexagonal bipyramidal	α-Fe_2O_3	α-Fe_2O_3/MoS_2/Ag	One-pot hydrothermal and postdeposition	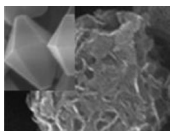	[208]
5	Polyhedron	TiO_2	$TiO_2/Ti_3C_2T_x$	In situ solvothermal	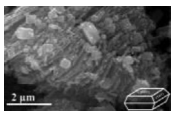	[209]
6	Nanonuts	$CuFe_2O_4$	$CuFe_2O_4/Ti_3C_2$	Ultrasonication	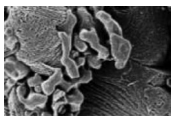	[210]
7	Rice crust-like	ZnO	$ZnO/Ti_3C_2T_x$	Calcination	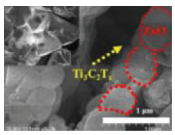	[211]
8	Decahedral	Fe–TiO_2	Fe–$TiO_2/Ti_3C_2T_x$	Hydrothermal acid treatment and Fe sputtering	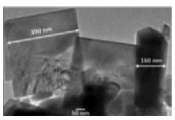	[212]
9	Spindle	α-Fe_2O_3	α-$Fe_2O_3/ZnFe_2O_4/Ti_3C_2$	Ultrasonic-assisted self-assemble	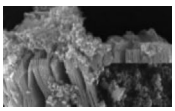	[213]
10	Irregular Flaky and wrinkled	$ZnFe_2O_4$ Fe_2O_3	rGO–Fe_2O_3–MoS_2	Two-step hydrothermal	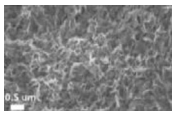	[195]
11	Thin shell	Fe_3O_4–MoS_2	Fe_3O_4–MoS_2/Ag_3PO_4	Hydrothermal and chemical precipitation	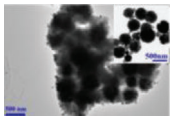	[214]
12	Spherical Nanobelts	Ag_3PO_4 TiO_2	Ag/MoS_2/TiO_{2-x}	Hydrothermal–photochemical reduction	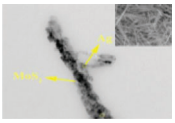	[215]

(*Continued*)

© 2024 The Author(s). Advanced Sustainable Systems published by Wiley-VCH GmbH

23667486, 2024, 12, Downloaded from https://advanced.onlinelibrary.wiley.com/doi/10.1002/adsu.202400483 by Nazarbayev University, Wiley Online Library on [08/07/2025]. See the Terms and Conditions (https://onlinelibrary.wiley.com/terms-and-conditions) on Wiley Online Library for rules of use; OA articles are governed by the applicable Creative Commons License

Table 1. (Continued)

No.	Metal oxide structure	Metal oxide	Composite material	Synthesis method	SEM/TEM images of the composite	Refs.
13	Well-defined core/shell	Fe_3O_4@TiO_2	Fe_3O_4@TiO_2–GO	Hydrothermal	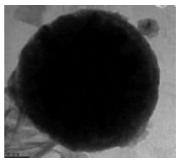	[216]
14	Nanoslices	CuO	MoS_2/CuO	Hydrothermal	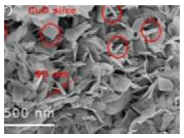	[217]
15	Nanofibers	TiO_2	MoS_2/TiO_2	Hydrothermal	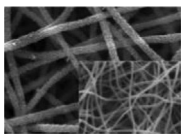	[218]
16	Fibrous	TiO_2@PMMA	MoS_2@TiO_2@PMMA	Hydrothermal	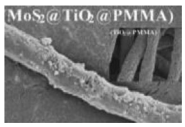	[219]
17	Walnut-like	$CaTiO_3$	$CaTiO_3$/MoS_2/RG	Ultrasonication	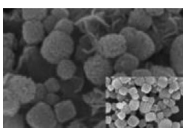	[220]

process yields composites exhibiting hierarchical architectures, as illustrated in Figure 4g,h.[180] A different approach for synthesizing WO_3 nanorods–graphene nanostructures involves precisely controlling the hydrothermal method (Figure 4i). This process utilizes WCl_6, ethanol, oxalic acid, and urea to form WO_3 nanopowder. The obtained powder is mixed with graphene nanosheets through ultrasonic treatment to form the rod shape (Figure 4j,k).[178]

3.4. Nanotube-Like Structures

Fabricating metal oxide-nanotube-based nanocomposites requires a systematic and customized approach considering each constituent material's properties and desired applications. To illustrate, the synthesis of a nanoheterojunction incorporating Ag_3PO_4/Ag/MoS_2/TiO_2 involves the integration of TiO_2 nanotubes via electrospinning, followed by the hydrothermal codeposition of Ag_3PO_4/Ag and MoS_2 (**Figure** 5a,b). This technique yielded a remarkably efficient nanoheterojunction with enhanced photocatalytic characteristics. XRD analysis in Figure 5c reveals distinct peaks for Ag_3PO_4, metallic Ag, MoS_2, and TiO_2, confirming that the 3D Z-scheme Ag_3PO_4/Ag/MoS_2/TiO_2 nanoheterojunction was successfully synthesized and that the materials are well-integrated into a cohesive heterojunction structure.[181] Furthermore, the fabrication of layered (CdS–Mn/MoS_2/CdTe)-promoted TiO_2 nanotube arrays involves anodization and annealing to form TiO_2 nanotubes. Subsequently, CdTe nanoparticles were pulse-electrodeposited and annealed. Next, MoS_2 nanosheets were synthesized hydrothermally on CdTe/TiO_2, followed by successive ionic layer adsorption and reaction (SILAR) coating of CdS–Mn nanoparticles onto MoS_2/CdTe/TiO_2. Figure 5d,e depicts the morphological structure of this synthesis.[182] In the meantime, the synthesis of the ternary MoS_2–TiO_2 nanotubes-Bi_2S_3 system utilizes microwave-assisted heating to generate a mixture containing TiO_2 nanotubes, $Bi(NO_3)_3$, and sodium molybdate dihydrate. The resulting compositions, distinguished by different solution volumes, exhibit variations.[183] Similarly, a ZnS/CdS–Mn/MoS_2/TiO_2 heterostructure was synthesized by deposition of MoS_2 onto TiO_2 nanotubes. Subsequently, SILAR was used to deposit the CdS–Mn layers, which were then topped with a ZnS capping layer. This intricate fabrication technique yields a heterostructure with improved functionalities. The EDX analysis in Figure 5f revealed the presence of O, S, Cd, Ti, Mn, Mo, and Zn in the nanotube arrays, though Te was missing, likely because of sample preparation losses.[184]

3.5. Cubic Structures

Composite material-based cubic metal oxide morphologies have been successfully synthesized using various methods. One example is the synthesis of Cu_2O–rGO nanoheterostructures

© 2024 The Author(s). Advanced Sustainable Systems published by Wiley-VCH GmbH

23667486, 2024, 12, Downloaded from https://advanced.onlinelibrary.wiley.com/doi/10.1002/adsu.202400483 by Nazarbayev University, Wiley Online Library on [08/07/2025]. See the Terms and Conditions (https://onlinelibrary.wiley.com/terms-and-conditions) on Wiley Online Library for rules of use; OA articles are governed by the applicable Creative Commons License

Table 2. Calculation of catalyst performance metrics under different light sources.

Catalysts	Pollutant, molecular weight [g mol^{-1}]	Light source	Wavelength [m]	Catalyst mass [mg]	Rxn time [min]	Lamp power [W]	Pollutant solution [mL]	Pollutant concern. [mg L^{-1}]	Removal eff. [%]	Amount of pollutant removed [mol]	Amount of pollutant removed [molecules]	Kinetic Rate [k; µmol g^{-1} h^{-1}]	Number of photons consumed	Quantum yield [QY; mol Photon^{-1}]	Space yield (SY; mol photon^{-1} mg^{-1}]	Energy consumption [Ec; Wh µmol^{-1}]	Figure of merit [FOM; mL g^{-1} µmol^{-1} Wh^{-1} h^{-1}]
TiO_2–GO	Phenol, 94.11	Visible light	4.60×10^{-07}	2000	120	33	80	10	48	4.08×10^{-06}	2.46×10^{18}	1.02	5.50×10^{23}	4.47×10^{-06}	2.24×10^{-09}	16.18	1.24
TiO_2/Ti_3C_2	Methylene Blue 319.85	UV light	3.65×10^{-07}	50	60	40	50	10	90	1.53×10^{-06}	9.23×10^{17}	30.64	2.64×10^{23}	3.49×10^{-06}	6.98×10^{-08}	26.11	38.30
$Bi_2S_3/MoS_2/TiO_2$	Methylene Blue 319.85	Solar light	5.00×10^{-07}	100	4	250	200	10	99	6.19×10^{-06}	3.73×10^{18}	928.56	1.51×10^{23}	2.47×10^{-05}	2.47×10^{-07}	1.03×10^{02}	290.77

The QY values use the peak wavelength reported in the paper. For reference, without specific wavelength information, 365 nm was used for UV light and 500 nm for visible and solar light. Similarly, the Ec values used for the lamp power were reported or assumed to be 300 W for UV/vis light and 1000 W for solar light.

through photochemical reduction. This process involved dissolving $Cu(OAc)_2$ in a solution of ethylene glycol and water, followed by the addition of GO powder and subsequent ultrasonication. The resulting mixture was then exposed to UV irradiation. The morphological structure of the synthesized materials is depicted in **Figure 6**a,b.[185] Meanwhile, CeO_2/MXene composites were synthesized by dispersing MXene nanosheets in water, incorporating $Ce(NO_3)_3{\cdot}6H_2O$, and subjecting the resulting suspension to hydrothermal treatment, as depicted in Figure 6c,d.[186] Similarly, MXene–Co_3O_4 cubic nanocomposites have been synthesized. First, MXene was dissolved in water, and then, a solution containing $Co(Ac)_2$ was added. The resulting mixture was then subjected to autoclave heating at a temperature of 120 °C for 8 h (Figure 6e–h).[187]

3.6. Layered Structures

Metal oxide nanosheets of multiple shapes have been synthesized successfully, including square,[188,189] rectangular,[190] lamellar,[62] nanoflakes,[126,191–193] and nanoplates structures.[194–198] For instance, the synthesis of square TiO_2 nanosheets on Ti_3C_2 involves selective exfoliation of Ti_3C_2 from Ti_3AlC_2, followed by purification steps. The exfoliated Ti_3C_2 is then hydrothermally oxidized in a Teflon-lined autoclave, resulting in the formation of (001)TiO_2/Ti_3C_2 nanosheets, as shown in **Figure 7**a,b and further confirmed by XRD analysis in Figure 7c.[188] Similarly, Wang et al. successfully synthesized $MoS_2/Bi_2O_2CO_3$ composites with a nanosheet-like morphology, as shown in Figure 7d,e, using a hydrothermal method.[199] Meanwhile, the synthesis of square nanosheet nanostructures of Au/Bi_2WO_6 nanosheet–MoS_2 heterojunctions, as illustrated in Figure 7f,g and supported by HRTEM analysis in Figure 7h, involves several steps. Initially, precursor solutions were prepared. Subsequently, microwave-assisted synthesis and directed assembly strategies are implemented to incorporate MoS_2 nanosheets into the heterostructure matrix.[200] Conversely, the formation of a Ti_3C_2/TiO_2/BiOCl thick lamellar structure, as depicted in Figure 7i,j, involves suspending Ti_3C_2 in acetic acid (HAc). Subsequently, $Bi(NO_3)_3{\cdot}5H_2O$ and KCl were added during the ultrasonication. The mixture was then transferred to a Teflon-lined autoclave and maintained at 180 °C for one day. The resulting products were then subjected to filtration, washing, and drying, yielding heterostructures with different mass ratios of Ti_3C_2 and BiOCl. The XRD analysis in Figure 7k,l demonstrates that Ti_3C_2 was partially converted to TiO_2, leading to Ti_3C_2/TiO_2/BiOCl heterojunction formation. This transformation enhances the material's photocatalytic efficiency.[62]

3.7. Film Structures

Developing and analyzing heterostructure thin films and composites have shown marked improvements in photocatalytic activity and crystallinity. MoS_2/V, N codoped TiO_2 heterostructure thin films were synthesized using sol–gel and chemical bath deposition techniques, followed by annealing at 500 °C. Scanning electron microscopy (**Figure 8**a) revealed that a 12 nm thick MoS_2 layer, optimally deposited over 45 min, significantly enhanced the

© 2024 The Author(s). Advanced Sustainable Systems published by Wiley-VCH GmbH

23667486, 2024, 12, Downloaded from https://advanced.onlinelibrary.wiley.com/doi/10.1002/adsu.202400483 by Nazarbayev University, Wiley Online Library on [08/07/2025]. See the Terms and Conditions (https://onlinelibrary.wiley.com/terms-and-conditions) on Wiley Online Library for rules of use; OA articles are governed by the applicable Creative Commons License

Table 3. Comparative analysis of performance evaluation criteria intervals.

Remarks score	Total score	Score	*k*	QY	SY	Ec	FOM
Poor	5–8	1	≤10	$\leq 0.25 \times 10^{-6}$	$\leq 0.6 \times 10^{-8}$	≥800	≤1
Fair	9–12	2	10–50	$0.25–3 \times 10^{-6}$	$0.61–5 \times 10^{-8}$	290–800	1–15
Good	13–16	3	51–300	$3–15 \times 10^{-6}$	$5–35 \times 10^{-8}$	110–290	15–100
Excellent	17–20	4	≥300	$\geq 15 \times 10^{-6}$	$\geq 36 \times 10^{-8}$	≤ 110	≥100

k: kinetic rate; QY: quantum yield; SY: space yield; Ec: energy consumption; FOM: figure of merit.

photocatalytic performance. Elemental analysis in Figure 8b confirmed the successful synthesis of the heterostructure.[201] In contrast, a study on anatase TiO_2–GO composite thin films demonstrated that composites containing 0.25% GO exhibited a crystallinity degree of ≈37%, comparable to the initial TiO_2 layer, suggesting orderly growth. The absence of the GO peak at $2\theta = 11.4°$ in the XRD spectra implies either a low GO content or disruption of the GO layers. Additionally, thermal treatments at 100 and 150 °C were found to have minimal impact on the crystallinity of the TiO_2 matrix (Figure 8c).[202] Moreover, a flexible and reusable photocatalyst was synthesized by polymerizing aniline in hydrochloric acid to form polyaniline (PANI), followed by developing and drying (Figure 8d). MoS_2 was dispersed within the PANI matrix by ultrasonic treatment, and the resulting mixture was cast into thin films to create a conductive material. The conductive MoS_2@PANI film was coated with NiO using direct current sputtering. AFM analysis in Figure 8e–j showed a significant increase in surface roughness after NiO sputtered onto the MoS_2@PANI film. NiO particles, ranging in size from 4.85 to 202 nm with an average diameter of 60 nm, contributed to the increased surface roughness. This increase is expected to boost the photocatalytic activity of the film by providing additional active sites for reactions.[203] Similarly, The MXene–PVA–TiO_2@PVDF membrane exhibits greater surface roughness of 143 nm and a larger surface area of 133.9 μm^2 compared to the MXene@PVDF membrane with 115 nm and 110 μm^2, respectively, as shown in Figure 8k,l. These enhancements were attributed to the integration of TiO_2 nanoparticles. Furthermore, the 2D/3D hierarchical structure created by the MXene and TiO_2 nanoparticles enhances the membrane's structural stability, making it more effective for its intended applications.[204]

3.8. Other Structures

A wide range of metal oxide structures have been developed and are categorized in **Table 1**. These structures included nanowires, leaf-like lamellas, octahedrals, hexagonal bipyramids, nanonuts, rice crust-like forms, decahedrals, spindles, nanobelts, well-defined core/shell configurations, nanoslices, nanofibers, structures, and walnut-like shapes. Each morphology offers unique advantages, such as increased surface area, enhanced light absorption, improved charge carrier mobility, and enhanced catalytic activity, all essential for photocatalysis applications. The selection of synthesis methods, such as hydrothermal processes, sol–gel techniques, coprecipitation, and ultrasonication, demonstrates the flexibility of customizing the morphological characteristics and properties of these metal oxide-based composite materials to meet specific performance requirements.

4. Performance Evaluation

Optimizing design and operational parameters rely on a comprehensive evaluation of photocatalytic performance, which, in turn, drives the formation of efficient and environmentally friendly technologies for diverse applications. The evaluation of photocatalytic performance includes critical indicators such as the reaction rate (*k*), quantum yield (QY), space yield (SY), energy consumption (Ec), and figure of merit (FOM). These metrics parameters provide valuable insights into efficiency, productivity, and sustainability.[47] The reaction rate (*k*), expressed in micromoles per gram per hour (μmol g^{-1} h^{-1}), and represents the speed of chemical transformations within the photocatalytic system (Equation (1)). This parameter plays a crucial role in improving catalyst design and industrial processes.[221] The QY, as defined by Equation (2), quantifies the efficiency of converting absorbed photons into reactive species, which is essential for pollutant degradation. Higher QY values indicate more efficient energy utilization. In contrast, the SY in Equation (3) measures productivity in terms of both time and mass.[222] Equation (4) illustrates Ec in Watt-hours per micromole (Wh μmol^{-1}), indicating efficiency and environmental impact. Achieving lower values is critical to promoting sustainability.[223] The integration of several parameters in evaluating the overall effectiveness, facilitated by utilizing the FOM as defined in Equation (5), allows for direct comparisons among photocatalysts and enables the identification of promising materials for practical applications, considering both efficiency and sustainability.[224] Detailed calculations of these variables are provided in **Table 2**

$$k = \frac{\text{Amount of pollutant removed } (\mu\text{mol})}{\text{Catalyst mass } (\text{g}) * \text{ Time } (\text{h})} \quad (1)$$

$$\text{QY} = \frac{\text{Decay Rate (molecule per second)}}{\text{Photon flux (photon per second)}} \quad (2)$$

$$\text{SY} = \frac{\text{QY (molecule per second)}}{\text{Photocatalyst mass } (\text{mg})} \quad (3)$$

$$\text{Ec} = \frac{\text{Lamp power } (\text{W}) * \text{ Time } (\text{h})}{\text{Amount of pollutant removed } (\mu\text{mol})} \quad (4)$$

$$\text{FOM} = \frac{\text{Product obtained } (\text{mL})}{\text{Catalyst mass } (\text{g}) * \text{ Time } (\text{h}) * \text{ Energy consumption } (\text{Wh mol}^{-1})} \quad (5)$$

© 2024 The Author(s). Advanced Sustainable Systems published by Wiley-VCH GmbH

23667486, 2024, 12, Downloaded from https://advanced.onlinelibrary.wiley.com/doi/10.1002/adsu.202400483 by Nazarbayev University, Wiley Online Library on [08/07/2025]. See the Terms and Conditions (https://onlinelibrary.wiley.com/terms-and-conditions) on Wiley Online Library for rules of use; OA articles are governed by the applicable Creative Commons License

Table 4. Assessing the performance of 2D-metal oxides nanoparticles (2D-MO NPs) in the degradation of organic compounds through photocatalysis: a color mapping-based approach.

No.	2D-metal oxide nanostructures	Pollutants	2D material–metal oxide nanostructure synthesis	Metal oxide morphology	Light source	Catalyst mass [mg]	Reaction time [min]	Pollutant solution [mL]	Pollutant conc. [mg L^{-1}]	Removal eff. [%]	Score					Total score	Remarks	Refs.
											k	QY	SY	Ec	FOM			
Graphene-based metal oxide nanoparticles																		
1	TiO_2–GO	Phenol	Hydrothermal	Irregular	**	2000	120	80	10	48						11	Fair	[225]
2	TiO_2/GO	Dichloroacetic acid	Hydrothermal	Flake-like	*	300	480	800	1000	87						20	Excellent	[126]
3	TiO_2/GO, GR	Phenol	Hydrothermal	Irregular	*	500	180	1000	10	100						19	Excellent	[123]
4	rGO/TiO_2, ZnO, WO_3	Methylene blue	Hydrothermal	Nanotubes ZnO, WO_3: irregular	**	100	60	200	10	88						14	Good	[226]
5	GO/TiO_2, ZnO	Phenol	Hydrothermal	Spherical	***	1250	60	100	40	100						11	Fair	[127]
6	ZnO/rGO	Bisphenol A	Hydrothermal	Spherical	*	25	30	100	10	93						15	Good	[133]
7	WO_3/rGO	Phenol	Hydrothermal	Nanoplates	**	50	60	100	10	91						17	Excellent	[163]
8	TiO_2/GO	Phenol	Chemical reduction	Spherical	**	1000	360	200	50	91						12	Fair	[130]
9	TiO_2–rGO	Phenol	UV-assisted photocatalytic reduction	Irregular	*	50	180	50	50	17						17	Excellent	[227]
10	W-TiO_2/rGO	Phenol	UV-assisted photocatalytic reduction	Big crystal-like	***	10	180	50	10	87						15	Good	[228]
11	TiO_2/GO	Acetaminophen	Hydrothermal	Nanotubes	*	100	180	500	5	96						19	Excellent	[229]
12	rGO/TiO_2	Bisphenol A	Sol–gel and hydrothermal	Film	*	25	180	50	10	95						9	Fair	[164]
13	TiO_2–GO	Atenolol	Hydrothermal	Irregular	**	225	60	150	25	72						11	Fair	[230]
14	TiO_2– rGO	Sulfamethoxazole	Photocatalytic treatment	Irregular	***	30	60	300	0.1	87						6	Poor	[231]
15	TiO_2–GO	Carbamazepine	Microwave-hydrothermal	Spherical	*	25.14	5	200	0.17	100						14	Good	[129]
16	$CoFe_2O_4$–GR	Methylene blue	Hydrothermal	Nanocrystals	**	25	240	100	20	100						10	Fair	[139]
17	$BiVO_4$–GR	Methyl orange	Hydrothermal	Leaf-like lamellas	**	50	180	100	20	94						10	Fair	[206]
18	Ag_3PO_4@rGO	Acid Blue-25	Hydrothermal	Spherical	**	150	60	200	14	100						11	Fair	[144]
19	WO_3/GR	Methylene blue	Hydrothermal	Nanorod	**	2	300	20	10	80						7	Poor	[178]
20	SnO_2–rGO	p-Hitropophenol	Hydrothermal-assisted ultraviolet irradiation	Nanoflakes	*	50	90	200	200	96						20	Excellent	[191]

(*Continued*)

© 2024 The Author(s). Advanced Sustainable Systems published by Wiley-VCH GmbH

23667486, 2024, 12, Downloaded from https://advanced.onlinelibrary.wiley.com/doi/10.1002/adsu.202400483 by Nazarbayev University, Wiley Online Library on [08/07/2025]. See the Terms and Conditions (https://onlinelibrary.wiley.com/terms-and-conditions) on Wiley Online Library for rules of use; OA articles are governed by the applicable Creative Commons License

Table 4. (Continued)

No.	2D-metal oxide nanostructures	Pollutants	2D material–metal oxide nanostructure synthesis	Metal oxide morphology	Light source	Catalyst mass [mg]	Reaction time [min]	Pollutant solution [mL]	Pollutant conc. [mg L^{-1}]	Removal eff. [%]	Score					Total score	Remarks	Refs.
											k	QY	SY	Ec	FOM			
21	g-Fe_3O_4/rGO	Phenol	Hydrothermal	Spherical	**	50	150	50	10	78						11	Fair	[233]
22	$Ce_2Zr_2O_7$@rGO	Ciprofloxacin	Photoreduction	Irregular	**	2	60	20	10	89						12	Fair	[234]
23	Ag_3PO_4/GR hydrogel	Bisphenol A	Impregnation	Spherical	**	150	12	100	10	100						16	Good	[143]
24	WO_3@rGO	Rhodamine B	One-step hydrothermal	Nanoflowers	***	20	240	40	20	75						6	Poor	[163]
25	$ZnSnO_3$/rGO	Metronidazole	Hydrothermal	Hollow nanospheres	*	100	60	200	5	100						14	Good	[235]
26	CoO@GR	Tetrabromobisphenol	Ultrasonication	Spherical	**	1.5	120	150	4	73						11	Fair	[146]
27	$BiVO_4$/rGO aerogel	Formaldehyde	Hydrothermal followed by freeze-drying	Tubular	*	50	15	150	50	60						20	Excellent	[236]
28	rGO/$Bi_{20}TiO_{32}$	Rhodamine B	One-pot hydrothermal	Wire	**	100	210	50	20	87						5	Poor	[205]
29	GO/TiO_2	Methyl orange	Chemical precipitation and heat treatment	Spherical	*	50	9	100	10	95						20	Excellent	[237]
30	Cu_2O–rGO	Methyl orange	UV-assisted reduction	Cubic	**	4	120	20	16	98						9	Fair	[185]
31	GO/TiO_2	Methyl orange	Self-assembly	Irregular	**	50	180	50	12	40						5	Poor	[238]
32	GO/TiO_2	Acid Orange-7	Surface functionalization	Nanorods	*	50	30	90	100	94						20	Excellent	[170]
33	ZnO/GO	Methylene blue	Hydrothermal	Spherical	*	50	55	100	10	75						17	Excellent	[134]
34	ZnO/GO	Methylene blue	Ultrasonication and chemical reduction	Spherical	*	50	40	100	32	90						19	Excellent	[135]
35	BiOI–GO	Methyl orange	One-step hydrothermal	Nanoplates	**	50	240	50	10	88						5	Poor	[197]
36	Ag_3PO_4–rGO	Methyl orange	Solution phase	Spherical	**	20	210	70	10	92						8	Poor	[145]
37	Bi_2O_3–rGO	Methylene blue	Microwave-assisted chemical reduction	Nanorods	**	2000	240	80	5	80						5	Poor	[173]
38	CeO_2–GO	Methylene blue	In situ growth hydrothermal	Spherical	**	2	210	25	5	98						8	Poor	[159]
MXene-based metal oxide nanoparticles																		
39	Bi_2WO_6/Nb_2CT_x	Methylene blue	Hydrothermal	Flower	**	50	12	100	15	93						17	Excellent	[162]

(*Continued*)

© 2024 The Author(s). Advanced Sustainable Systems published by Wiley-VCH GmbH

23667486, 2024, 12, Downloaded from https://advanced.onlinelibrary.wiley.com/doi/10.1002/adsu.202400483 by Nazarbayev University, Wiley Online Library on [08/07/2025]. See the Terms and Conditions (https://onlinelibrary.wiley.com/terms-and-conditions) on Wiley Online Library for rules of use; OA articles are governed by the applicable Creative Commons License

Table 4. (Continued)

No.	2D-metal oxide nanostructures	Pollutants	2D material–metal oxide nanostructure synthesis	Metal oxide morphology	Light source	Catalyst mass [mg]	Reaction time [min]	Pollutant solution [mL]	Pollutant conc. [mg L^{-1}]	Removal eff. [%]	Score					Total score	Remarks	Refs.
											k	QY	SY	Ec	FOM			
40	(111) TiO_2/Ti_3C_2	Methyl orange	Hydrothermal	Octahedral	**	10	140	200	20	99						16	Good	[207]
41	TiO_2/Ti_3C_2	Methylene blue	Hydrothermal and calcination	Granular	*	50	60	50	10	98						15	Good	[239]
42	$TiO_2/Ti_3C_2T_x$	Methylene blue	In situ solvothermal	Polyhedron	*	50	30	50	1	98						6	Poor	[209]
43	$WO_3/Ti_3C_2T_x$	Methylene blue	Sonication	Rod-like	***	5	80	100	5	89						10	Fair	[179]
44	TiO_2/Ti_3C_2	Methyl orange	Hydrothermal	Square nanosheets	*	10	240	200	20	97						15	Good	[188]
45	$TiO_2/Ti_3C_2T_x$	Methyl orange	In situ solvothermal	Irregular	*	50	70	50	10	91						8	Poor	[240]
46	TiO_2/Ti_3C_2	Methyl orange	Hydrothermal	Irregular	*	100	30	100	20	98						17	Excellent	[241]
47	Ti_3C_2/TiO_2	Methyl orange	Hydrothermal	Irregular	***	35	35	60	30	99						15	Good	[242]
48	$BiVO_4/Ti_3C_2$	Methyl orange	Ultrasonication	Spherical	**	100	130	150	10	99						10	Fair	[158]
49	$TiO_2/Ti_3C_2T_x$	Phenol	In situ solvothermal	Irregular	*	5	120	50	15	90						16	Good	[243]
50	$BiOBr/Ti_3C_2$	Rhodamine B	Electrostatic self-assembly	Spherical	**	10	24	50	20	99						17	Excellent	[155]
51	$BiFeO_3/Ti_3C_2T_x$	Congo red	Sol–gel	Irregular	**	100	150	100	30	100						10	Fair	[244]
52	Bi_2MoO_6/Ti_3C_2	Tetracycline	One-step hydrothermal	2D nanosheet	**	10	30	20	15	99						15	Good	[245]
53	CeO_2/Ti_3C_2	Tetracycline	Hydrothermal	Cubes	**	30	60	30	10	80						8	Poor	[186]
54	Ag_3PO_4/Ti_3C_2	Tetracycline	Electrostatically driven self-assembly	Spherical	**	400	5	50	20	80						14	Good	[141]
55	CuO/Ti_3C_2	Methylene blue	Sonication	Spherical	***	50	80	50	10	99						6	Poor	[157]
56	ZnO/Ti_3C_2	Rhodamine B	Chemical reaction	Microrods	*	100	18	40	5	98						10	Fair	[180]
57	$ZnO/Ti_3C_2T_x$	Rhodamine B	Calcination	Rice crust-like	***	30	70	50	100	100						15	Good	[211]
58	$Bi_2O_2CO_3/Ti_3C_2T_x$	Levofloxacin	Hydrothermal	Small flakes	***	50	80	100	20	96						14	Good	[192]
59	$Bi0.9La0.1Fe0.95Mn_{0.05}O_3/Ti_3C_2$	Congo red	Double solvent sol–gel	Irregular	**	100	20	100	100	100						18	Excellent	[246]
60	Bi_2WO_6/Ti_3C_2	Amoxicillin	Hydrothermal	Flake-like	***	20	60	50	20	100						14	Good	[247]
61	α-$Fe_2O_3/Ti_3C_2T_x$	Rhodamine B	Ultrasonic-assisted synthesis	2D nanosheet	**	20	120	100	10	98						10	Fair	[60]
62	Fe–$TiO_2/Ti_3C_2T_x$	Carbamazepine	Hydrothermal acid treatment and Fe sputtering	Decahedral	*	50	60	25	14	99						11	Fair	[212]
63	Nb_2O_5/Nb_2CT_x	Rhodamine B	Hydrothermal	Nanorods	**	25	120	25	10	99						6	Poor	[176]

(*Continued*)

© 2024 The Author(s). Advanced Sustainable Systems published by Wiley-VCH GmbH

23667486, 2024, 12, Downloaded from https://advanced.onlinelibrary.wiley.com/doi/10.1002/adsu.202400483 by Nazarbayev University, Wiley Online Library on [08/07/2025]. See the Terms and Conditions (https://onlinelibrary.wiley.com/terms-and-conditions) on Wiley Online Library for rules of use; OA articles are governed by the applicable Creative Commons License

Table 4. (Continued)

No.	2D-metal oxide nanostructures	Pollutants	2D material–metal oxide nanostructure synthesis	Metal oxide morphology	Light source	Catalyst mass [mg]	Reaction time [min]	Pollutant solution [mL]	Pollutant conc. [mg L^{-1}]	Removal eff. [%]	Score					Total score	Remarks	Refs.
											k	QY	SY	Ec	FOM			
64	$SnNb_2O_6/Ti_3C_2T_x$	Tetracycline	Ultrasonication-assisted Hydrothermal	Nanosheets	**	15	60	60	10	70						10	Fair	[61]
65	$TiO_2/Ti_3C_2T_x$	4-Chlorophenol	Hydrothermal	Nanospheres	*	50	150	100	20	100						14	Good	[248]
66	$CeO_2/Ti_3C_2T_x$	Rhodamine B	One-step hydrothermal	Nanorods	*	50	90	50	20	75						8	Poor	[175]
MoS_2-based metal oxide nanoparticles																		
67	$MoS_2/BiOBr$	Rhodamine B	Solvothermal	Sphere-like	***	20	120	100	10	94						8	Poor	[154]
68	$MoS_2/BiOI$	Rhodamine B	One-step solvothermal	Nanosheets	**	30	50	100	10	95						11	Fair	[249]
69	$MoS_2/Bi_2O_2CO_3$	Rhodamine B	Hydrothermal	2D nanosheets	*	50	10	100	10	100						13	Good	[199]
70	MoS_2/Bi_2MoO_6	Rhodamine B	Exfoliation and solvothermal	2D nanosheets	**	100	150	50	10	100						6	Poor	[250]
71	Ag_3PO_4/MoS_2	Methylene blue	Hydrothermal in situ	Spherical	**	25	30	100	10	100						13	Good	[251]
72	Ag_3PO_4/MoS_2	Methylene blue	Solvent precipitation	Spherical	**	30	60	30	20	100						16	Good	[252]
73	Ag_2VO_4/MoS_2	Methylene blue	Hydrothermal	Spherical	**	50	18	100	10	91						13	Good	[153]
74	MoS_2/ZnO	Methylene blue	Hydrothermal	Spherical	**	20	100	100	20	93						16	Good	[137]
75	MoS_2/ZnO	Methylene blue	Coprecipitation	Irregular	*	50	120	100	10	99						17	Excellent	[124]
76	MoS_2–FeZnO	Methylene blue	Hydrothermal	Flower-like	***	150	140	150	20	93						7	Poor	[165]
77	MoS_2/TiO_2	Methyl orange	Hydrothermal	Nanofibers	*	10	35	100	10	97						17	Excellent	[218]
78	N. TiO_2–x/MoS_2	Methyl orange	Hydrothermal	Nanospheres	**	50	120	50	10	92						6	Poor	[253]
79	ZrO_2/MoS_2	Methyl orange	Precipitation	Spherical	*	50	12	100	10	95						19	Excellent	[152]
80	MoS_2/TiO_2	Phenol	Hydrothermal	Hollow spheres	**	10	150	60	10	78						11	Fair	[254]
81	MoS_2/ZnO	Phenol red	One-step hydrothermal	Nanoflowers	*	20	50	30	10	93						11	Fair	[255]
82	MoS_2/ZnO	Methyl red	One-step hydrothermal	Spherical	**	10	60	25	10	89						11	Fair	[256]
83	MoS_2/N. S. TiO_2	Diclofenac	Hydrothermal	Rectangular sheets	**	100	150	100	5	98						10	Fair	[190]

(*Continued*)

© 2024 The Author(s). Advanced Sustainable Systems published by Wiley-VCH GmbH

23667486, 2024, 12, Downloaded from https://advanced.onlinelibrary.wiley.com/doi/10.1002/adsu.202400483 by Nazarbayev University, Wiley Online Library on [08/07/2025]. See the Terms and Conditions (https://onlinelibrary.wiley.com/terms-and-conditions) on Wiley Online Library for rules of use; OA articles are governed by the applicable Creative Commons License

Table 4. (Continued)

No.	2D-metal oxide nanostructures	Pollutants	2D material–metal oxide nanostructure synthesis	Metal oxide morphology	Light source	Catalyst mass [mg]	Reaction time [min]	Pollutant solution [mL]	Pollutant conc. [mg L^{-1}]	Removal eff. [%]	Score					Total score	Remarks	Refs.
											k	QY	SY	Ec	FOM			
84	$BiOCl/MoS_2$	Rhodamine B	Pulse ultrasonic-assisted	Nanosheet	***	10	30	50	10	99						16	Good	[257]
85	$BiFeWO_6/MoS_2$	Rhodamine B	Hydrothermal	Irregular	**	25	75	75	25	100						9	Fair	[258]
86	Ag_3PO_4/MoS_2	Rhodamine B	Hydrothermal	Spherical	**	100	8	100	20	90						15	Good	[142]
87	MoS_2/Fe_3O_4	Methyl orange	Hydrothermal	Small clusters	**	50	100	50	10	80						7	Poor	[259]
88	MoS_2/Ag_2WO_4	Methyl orange	Hydrothermal	Rod-like	**	10	120	100	3	64						9	Fair	[260]
89	$MoS_2/BiOBr$	Reactive Blue	Hydrothermal	2D flake-like	**	50	180	100	10	72						12	Fair	[261]
90	$MoS_2/MnFe_2O_4$	Acid Blue-113	Hydrothermal	Spherical	**	6.6	42	200	25	99						18	Excellent	[150]
91	$MoS_2/CoFe_2O_4$	Rhodamine B	Hydrothermal	Spherical	**	50	90	50	20	94						6	Poor	[140]
92	$CoFe_2O_4/MoS_2$	Congo red	Electrospinning and hydrothermal	Nanorod	**	30	60	100	20	95						10	Fair	[262]
93	Bi_2O_3/MoS_2	Tetracycline	Deposition and hydrothermal	Irregular	**	50	100	50	30	97						8	Poor	[263]
94	MoS_2/ZnO	Methylene blue	Hydrothermal reduction	Spherical	**	30	80	30	1	82						10	Fair	[264]
95	B-ZnO–MoS_2	Methylene blue	Hydrothermal	Spherical	**	20	180	50	3.2	95						10	Fair	[138]

*UV light; **Visible light; ***Solar light.

© 2024 The Author(s). Advanced Sustainable Systems published by Wiley-VCH GmbH

23667486, 2024, 12, Downloaded from https://advanced.onlinelibrary.wiley.com/doi/10.1002/adsu.202400483 by Nazarbayev University, Wiley Online Library on [08/07/2025]. See the Terms and Conditions (https://onlinelibrary.wiley.com/terms-and-conditions) on Wiley Online Library for rules of use; OA articles are governed by the applicable Creative Commons License

Table 5. Performance assessment of 2D-metal oxide nanocomposites (2D-MO NCs) in the degradation of organic compounds through photocatalysis: a color mapping-based approach.

No.	2D-metal oxide nanostructures and composites	Pollutants	2D material–metal oxide nanostructure synthesis	Metal oxide morphology	Light source	Catalyst mass [mg]	Reaction time [min]	Pollutant Solution [mL]	Pollutant conc. [mg L^{-1}]	Removal eff. [%]	Score					Total score	Remarks	Refs.
											k	QY	SY	Ec	FOM			
Graphene-based metal oxide nanocomposites																		
96	Cr_2S_3–GO/TiO_2	Methylene blue	Coprecipitation	Irregular	**	20	120	50	10	98.3						10	Fair	[265]
97	rGO/TiO_2/ZnO	Bisphenol A	Coprecipitation, sol–gel, and hydrothermal	TiO_2:film ZnO:nanowires	**	25	180	50	10	94.9						9	Fair	[164]
98	g-C_3N_4/rGO/WO_3	Ciprofloxacin	Photoreduction-assisted self-assembly	Spherical	**	10	180	50	20	85						10	Fair	[266]
99	BiOI/Fe_3O_4@GO	2,4-Dinitrophenol	Chemical coprecipitation	BiOI: flower, Fe_3O_4: spherical	**	50	100	50	129	100						20	Excellent	[147]
100	C_3N_4@$MnFe_2O_4$-G	Metronidazole	Impregnation	Irregular	**	50	60	50	20	94.5						14	Good	[267]
101	rGO/SiO_2/ZrO_2	Bisphenol A	Chemical reduction	Irregular	**	75	90	200	10	87						14	Good	[268]
102	Fe_3O_4@TiO_2–GO	Enrofloxacin	Hydrothermal	Well-defined core/shell structure	**	20	240	50	2	96						5	Poor	[216]
103	NiAl LDH/Fe_3O_4–rGO	Ciprofloxacin	One-pot hydrothermal	Spherical	**	10	150	40	10	91						7	Poor	[269]
104	Ag–Cu_2O/rGO	Phenol	Water bath synthesis method at 55 °C	Octahedral	**	50	210	50	10	97						11	Fair	[270]
105	PANI–TiO_2/rGO hydrogel	Bisphenol A	Hydrothermal	Irregular	*	20	100	50	40	60						12	Fair	[149]
106	$MgFe_2O_4$–TiO_2NPs@GO	Methylene blue	Sonication-assisted	TiO_2: hexagonal, $MgFe_2O_4$: spherical	*	50	120	100	50	99						16	Good	[271]
107	$BiVO_4$/$BiPO_4$/GO	Reactive Blue	One-pot controlled hydrothermal	$BiPO_4$: square and rectangular bar, $BiVO_4$: sheet	**	30	60	50	80	99						9	Fair	[272]
108	rGO/NiO/CuO	Brilliant green	One-pot hydrothermal	Irregular	*	50	60	100	10	80						16	Good	[273]
109	CeO_2/Fe_2O_3/rGO	Methyl orange	Hydrothermal	CeO_2: spherical, Fe_2O_3: microspheres	**	100	100	1000	10	86						15	Good	[274]
110	ZnO–Bi_2O_3/GO	Acid Blue-25	Hydrothermal	Spherical	**	50	120	100	100	98.31						14	Good	[132]
111	Ag@AgBr/$BiPO_4$/rGO	Reactive Blue	Hydrothermal-assisted in situ UV reduction	Multifaceted block	***	30	240	50	50	90.1						6	Poor	[275]

(*Continued*)

© 2024 The Author(s). Advanced Sustainable Systems published by Wiley-VCH GmbH

23667486, 2024, 12, Downloaded from https://advanced.onlinelibrary.wiley.com/doi/10.1002/adsu.202400483 by Nazarbayev University, Wiley Online Library on [08/07/2025]. See the Terms and Conditions (https://onlinelibrary.wiley.com/terms-and-conditions) on Wiley Online Library for rules of use; OA articles are governed by the applicable Creative Commons License

Table 5. (Continued)

No.	2D-metal oxide nanostructures and composites	Pollutants	2D material–metal oxide nanostructure synthesis	Metal oxide morphology	Light source	Catalyst mass [mg]	Reaction time [min]	Pollutant Solution [mL]	Pollutant conc. [mg L^{-1}]	Removal eff. [%]	Score					Total score	Remarks	Refs.
											k	QY	SY	Ec	FOM			
112	$Ag/GR/BiVO_4$	Rhodamine B	One-pot solvothermal	Irregular	**	150	180	100	10	100						6	Poor	[276]
113	$Bi_2MoO_6/Ag_3PO_4/rGO$	Reactive Blue	In situ precipitation	Irregular	**	30	180	50	50	98						7	Poor	[277]
114	TiO_2–ZnO–rGO	Methylene blue	Two-step solvothermal approach	Bi_2MoO_6: nanosheets, Ag_3PO_4: cubic	**	10	120	100	0.3	92						5	Poor	[167]
115	CdS–ZnO–rGO	Methyl orange	Hydrothermal	TiO_2: spherical, ZnO: nanorods	***	10	60	50	32	95						14	Good	[278]
116	ZnO–Ag–rGO	Methylene blue	Hydrothermal	Rod-shaped	***	50	120	50	10	94.5						8	Poor	[161]
117	TiO_2–Zr–rGO	Eosin Blue	Modified sol–gel	Spherical	**	25	90	100	20	96						12	Fair	[279]
118	TiO_2–Au–GO	Acid Blue-93	Modified sol–gel	Irregular	*	80	120	100	20	60						5	Poor	[280]
119	TiO_2/Dia/GO	Phenol	Diazotization-assisted hydrothermal	Spherical	**	100	300	100	100	40						16	Good	[232]
MXene-based metal oxide nanocomposites																		
120	$AgNPs/TiO_2/Ti_3C_2T_x$	Methylene blue	Hydrothermal	Spherical	*	10	30	100	10	99						17	Excellent	[128]
121	$Ti_3C_2/TiO_2/CuO$	Methyl orange	Calcination	Irregular	*	100	80	100	20	99						13	Good	[281]
122	$Ag/Ag_3PO_4/Ti_3C_2$	Methyl orange	Electrostatic self-assembly	Spherical	**	50	60	10	20	93						7	Poor	[282]
123	$TiO_2/Ti_3C_2/g\text{-}C_3N_4$	Rhodamine B	Calcination	Irregular	**	100	60	100	10	99.9						7	Poor	[283]
124	$MXene/TiO_2/g\text{-}C_3N_4$	Rhodamine B	Calcination	Irregular	**	60	50	100	20	98						14	Good	[284]
125	$\alpha\text{-}Fe_2O_3/ZnFe_2O_4/Ti_3C_2$	Rhodamine B	Ultrasonic-assisted self-assemble	$\alpha\text{-}Fe_2O_3$: spindle, $ZnFe_2O_4$: irregular	**	20	150	100	10	100						9	Fair	[213]
126	$CdS@Ti_3C_2@TiO_2$	Methylene blue	Hydrothermal	Irregular	**	50	88	200	20	100						14	Good	[285]
127	Ti_3C_2–MXene/NiO/$CsPbI_3$	Crystal violet	Hydrothermal-precipitation	Spherical	**	25	90	100	15	92.8						13	Good	[286]
128	ZnO/TiO_2–Ti_3C_2	Ceftriaxone sodium	Self-assembled	TiO_2: nanorods, ZnO: spherical	***	25	180	500	5	99.4						12	Fair	[136]

(*Continued*)

© 2024 The Author(s). Advanced Sustainable Systems published by Wiley-VCH GmbH

23667486, 2024, 12, Downloaded from https://advanced.onlinelibrary.wiley.com/doi/10.1002/adsu.202400483 by Nazarbayev University, Wiley Online Library on [08/07/2025]. See the Terms and Conditions (https://onlinelibrary.wiley.com/terms-and-conditions) on Wiley Online Library for rules of use; OA articles are governed by the applicable Creative Commons License

Table 5. (Continued)

No.	2D-metal oxide nanostructures and composites	Pollutants	2D material–metal oxide nanostructure synthesis	Metal oxide morphology	Light source	Catalyst mass [mg]	Reaction time [min]	Pollutant Solution [mL]	Pollutant conc. [mg L^{-1}]	Removal eff. [%]	Score					Total score	Remarks	Refs.
											k	QY	SY	Ec	FOM			
129	$CdS/Nb_2O_5/Nb_2C$	Carbamazepine	Hydrothermal	Nanorods	**	5	240	50	10	92						9	Fair	[177]
130	$MXene/NiFe_2O_4/V_2O_5$	Rhodamine B	Hydrothermal	V_2O_5: block-like, $NiFe_2O_4$: irregular	**	10	240	100	10	88.7						11	Fair	[287]
131	$Ti_3C_2T_x/TiO_2/BiOCl$	Tetracycline	Hydrothermal	BiOCl: thick lamellar, TiO_2: irregular	**	50	120	50	20	90						8	Poor	[62]
132	$Ag_3PO_4/MXene–TiO_2$	Rhodamine B	Calcination, precipitation, ultrasound, and thermal treatments	Ag_3PO_4: spherical TiO_2: granular	**	50	120	100	20	94.07						10	Fair	[288]
133	$CoO@TiO_2/Ti_3C_2T_x$	Phenol	Facial sonication–hydrothermal	CoO: spherical, TiO_2: irregular	**	20	15	100	20	96						20	Excellent	[289]
134	$Ti_2CT_x/3\%TiO_2/(1\%Ag, 1\%Ag_2O, 1\%Pd, 1\%PdO, 1\%Au)$	Salicylic acid	Stirring-assisted precipitation and reduction	Ball-shaped	*	250	180	400	14	97.1						15	Good	[290]
135	α-Fe_2O_3@ TiO_2@MXene	Tetracycline	Ultrasonication	Irregular	**	10.8	124	20	39.37	98.36						10	Fair	[291]
136	$ZnS/CuFe_2O_4/MXene$	Direct Black RN	Hydrothermal	Spherical	**	10	30	5	50	100						10	Fair	[292]
137	$Ti_3C_2–OH/Bi_2WO_6:Yb^{3+}, Tm^{3+}$	Rhodamine B	Hydrothermal	Spherical	**	10	30	50	8.16	91						13	Good	[58]
138	$In_2S_3/TiO_2@Ti_3C_2T_x$	Methyl orange	Hydrothermal	Irregular	**	60	60	100	20	92.1						14	Good	[293]
139	$BiOBr/TiO_2/Ti_3C_2T_x$	Rhodamine B	Hydrothermal	BiOBr: nanoplates, TiO_2: Irregular	**	20	30	50	100	99.8						18	Excellent	[194]
MoS_2-based metal oxide nanocomposites																		
140	$ZnO/MoS_2/rGO$	Methylene blue	Hydrothermal	Spherical	***	20	60	50	16	98						9	Fair	[294]
141	$MoS_2/g\text{-}C_3N_4/TiO_2$	Methylene blue	Wet impregnation	Spherical	**	30	45	100	10	99.5						10	Fair	[295]
142	CdS. $MoS_2/HTiO_2$	Tetracycline	Hydrothermal	Nanobelts	**	50	180	100	10	82.6						6	Poor	[296]
143	$MoS_2/Fe_3O_4/rGO$	Rhodamine B	Hydrothermal	Flower-like	**	3	40	50	30	100						12	Fair	[166]
144	$Fe_3O_4–MoS_2@Au$	Rhodamine B	Hydrothermal and sonication	Spherical	**	30	40	200	20	90						12	Fair	[148]

(*Continued*)

© 2024 The Author(s). Advanced Sustainable Systems published by Wiley-VCH GmbH

23667486, 2024, 12, Downloaded from https://advanced.onlinelibrary.wiley.com/doi/10.1002/adsu.202400483 by Nazarbayev University, Wiley Online Library on [08/07/2025]. See the Terms and Conditions (https://onlinelibrary.wiley.com/terms-and-conditions) on Wiley Online Library for rules of use; OA articles are governed by the applicable Creative Commons License

Table 5. (Continued)

No.	2D-metal oxide nanostructures and composites	Pollutants	2D material–metal oxide nanostructure synthesis	Metal oxide morphology	Light source	Catalyst mass [mg]	Reaction time [min]	Pollutant Solution [mL]	Pollutant conc. [mg L^{-1}]	Removal eff. [%]	Score					Total score	Remarks	Refs.
											k	QY	SY	Ec	FOM			
145	rGO–MoS_2–$NiCo_2O_4$	Rhodamine B	Hydrothermal	Spherical	**	4	90	40	500	95						13	Good	[151]
146	MoS_2/SnO_2/CC	Rhodamine B	Hydrothermal	Rod-like	**	100	90	50	15	95						10	Fair	[174]
147	Ag_3PO_4/Ag/MoS_2/TiO_2	Methylene blue	Electrospinning–hydrothermal–chemical codeposition	Ag_3PO_4/Ag: spherical, TiO_2: nanotubes	***	15	12	75	5	95						15	Good	[181]
148	MoS_2@TiO_2@PMMA	Methyl orange	Hydrothermal	Fibrous	*	100	50	100	10	95.7						15	Good	[219]
149	MoS_2/Al_2O_3/g-C_3N_4	Crystal violet	Hydrothermal	Irregular	**	5	90	100	100	97.3						14	Good	[297]
150	$BiVO_4$/Bi_2S_3/MoS_2	Malachite green	In situ hydrothermal	Diamond-shaped	***	100	300	200	25	94						6	Poor	[298]
151	CFs/TiO_2/MoS_2	Acid Orange-7	Hydrothermal	Nanorods	**	150	60	50	10	94.2						7	Poor	[171]
152	MoS_2/g-C_3N_4/$Bi_{24}O_{31}C_{l10}$	Tetracycline	Impregnation–calcination	Irregular	**	10	50	50	20	97.5						12	Fair	[299]
153	Bi_2WO_6@MoS_2/graphene	Rhodamine B	Two-step hydrothermal	Microspheres	**	20	180	60	10	77.31						7	Poor	[300]
154	rGO–Fe_2O_3–MoS_2	Methylene blue	Two-step hydrothermal	Flaky and wrinkled structures	**	5	50	50	10	98						14	Good	[195]
155	Graphene/MoS_2/Fe_2O_3	Methylene blue	Two-step hydrothermal	Spherical	**	7.5	80	15	5	36						10	Fair	[301]
156	MoS_2/CdS/TiO_2	Methylene blue	Solvothermal	Spherical	**	7.5	160	15	5	72						8	Poor	[302]
157	MoS_2/rGO/Cu_2O	Rhodamine B	Hydrothermal and precipitation	Spherical	***	50	45	100	10	98						8	Poor	[303]
158	Ag_3PO_4/TiO_2@MoS_2	Methylene blue	Electrospinning, hydrothermal, and chemical deposition	TiO_2: nanofibers, Ag_3PO_4: spherical	**	250	10	500	2.5	92						12	Fair	[304]
159	g-C_3N_4/WO_3/MoS_2	Methylene blue	Cocalcination and hydrothermal	Square sheet	**	100	60	100	20	83.4						9	Fair	[189]
160	Bi_2S_3/MoS_2/TiO_2	Methylene blue	Microwave-assisted hydrothermal	Nanotubes	***	100	4	200	10	99						19	Excellent	[183]
161	rGO–ZnO-decorated MoS_2	Methylene blue	Hydrothermal	Irregular	***	100	75	100	20	90						7	Poor	[305]

(*Continued*)

© 2024 The Author(s). Advanced Sustainable Systems published by Wiley-VCH GmbH

23667486, 2024, 12, Downloaded from https://advanced.onlinelibrary.wiley.com/doi/10.1002/adsu.202400483 by Nazarbayev University, Wiley Online Library on [08/07/2025]. See the Terms and Conditions (https://onlinelibrary.wiley.com/terms-and-conditions) on Wiley Online Library for rules of use; OA articles are governed by the applicable Creative Commons License

Table 5. (Continued)

No.	2D-metal oxide nanostructures and composites	Pollutants	2D material–metal oxide nanostructure synthesis	Metal oxide morphology	Light source	Catalyst mass [mg]	Reaction time [min]	Pollutant Solution [mL]	Pollutant conc. [mg L^{-1}]	Removal eff. [%]	Score					Total score	Remarks	Refs.
											k	QY	SY	Ec	FOM			
162	MoS_2/TiO_2/HMFs	Methylene blue	Sol–gel method and high-temperature calcination	Irregularly	**	10	120	32	20	98.7						8	Poor	[306]
163	$CaTiO_3/MoS_2$/rGO	Methyl violet	Ultrasonication	Walnut-like	***	10	75	20	15	97						8	Poor	[220]
164	Au/Bi_2WO_6–MoS_2	Tetracycline	Hydrothermal, dispersion, and liquid exfoliation	Nanosheets	**	50	30	50	10	85.8						11	Fair	[200]
165	TiO_2–MoS_2–rGO	Bisphenol A	Hydrothermal	Spherical	*	50	300	50	500	62.4						13	Good	[131]
	ZnO/MoS_2/CNT	Aniline	Hydrothermal	Nanorods	**	1200	120	100	100	76						11	Fair	[169]
167	Ag/MoS_2/TiO_2-x	Bisphenol A	Hydrothermal-photochemical reduction	Nanobelts	**	35	120	20	10	96.7						6	Poor	[215]
168	g-C_3N_4@TiO_2/MoS_2	Methylene blue	Solvothermal-assisted ultrasonication	Sphere	**	30	60	50	10	97.6						10	Fair	[307]
169	TiO_2@MoS_2Au	Methylene blue	Precipitation, hydrothermal	Microtubes	**	5	120	40	10	89.73						10	Fair	[308]

*UV light; **Visible light; ***Solar light.

© 2024 The Author(s). Advanced Sustainable Systems published by Wiley-VCH GmbH

23667486, 2024, 12, Downloaded from https://advanced.onlinelibrary.wiley.com/doi/10.1002/adsu.202400483 by Nazarbayev University, Wiley Online Library on [08/07/2025]. See the Terms and Conditions (https://onlinelibrary.wiley.com/terms-and-conditions) on Wiley Online Library for rules of use; OA articles are governed by the applicable Creative Commons License

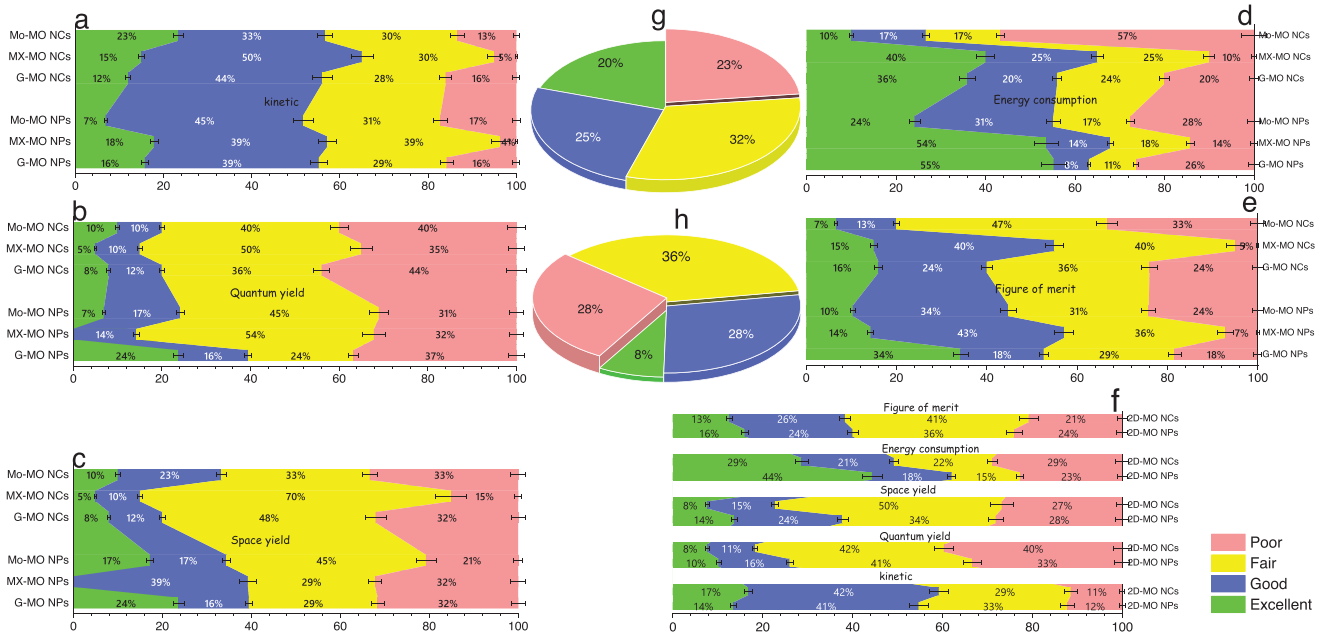

Figure 9. A comparative analysis of performance metrics of the 2D composite materials.

From the analysis of 169 composites, as detailed in **Tables 4** and **5**, and the scores assigned after evaluation, the quartile method was used to categorize the data into four groups. By using this method, data are evenly split into quartiles, enhancing the clarity of the analysis. Quartiles are obtained by sorting the data in ascending order and dividing it into four equal parts. The first quartile (Q1) marks the value below which 25% of the data falls, while the second quartile (Q2), or median, represents the midpoint, with 50% of the data below it. The third quartile (Q3) indicates the value below which 75% of the data falls. Based on these quartiles, the data is divided into four groups: Group 1 includes values $\leq$ Q1, Group 2 includes values $>$ Q1 and $\leq$ Q2, Group 3 includes values $>$ Q2 and $\leq$ Q3, and Group 4 includes values $>$ Q3. Using the example of energy consumption, Q1 was 110, Q2 was 290, and Q3 was 800. **Table 3** summarizes the performance evaluation criterion intervals. Each row represents a different performance metric, allowing for comparison.

4.1. Parameters Affecting the Photocatalytic Removal of Organic Compounds

2D composite materials display strong kinetic properties, particularly in the excellent and good categories (**Figure 9a**). Mo–Mo nanocrystals (NCs) exhibit superior kinetics, with MX–Mo nanoparticles (NPs) closely following. A similar pattern is seen in FOM performance (Figure 9e), where G-MO NPs stand out, followed by G-MO NCs and MX–MO NCs. However, as shown in Figure 9b,c, the quantum and space yields are less remarkable. G-MO NPs lead in quantum yield, with Mo–MO NCs in second place. For space yield, G-MO NPs again perform well, followed by Mo–MO NPs. Notably, these nanocomposites are highly energy-efficient, requiring less energy, as depicted in Figure 9d. G-MO NPs and MX–MO NPs demonstrate good energy efficiency, whereas Mo–MO NCs fall short. These composites excel in kinetics and energy efficiency, while their quantum yield, space yield, and FOM are acceptable (Figure 9f). Across all parameters except for kinetics, 2D-MO NPs outperform 2D-MO NCs. Importantly, Figure 9g,h underscores the superiority of single metal oxides–2D materials over their composites. In this context, 20% and 23% of these single metal oxides–2D materials attained "excellent" and "poor" ratings, respectively, compared to 8% and 28% for their composites.

Table 6 comprehensively compares the photocatalytic degradation behaviors of various nanocomposites. This highlights the key factors influencing the performance of 23 specific materials among the 169 samples analyzed. By examining this table, we gain a deeper understanding of the parameters that may affect the photocatalytic activity of these metal oxide-supported 2D materials.

4.2. Influence of Morphology

The morphology of nanoparticles plays a crucial role in determining their effectiveness in the photodegradation of organic pollutants, as variations in their shape directly influence properties such as crystalline facets, surface composition, and overall geometry. For example, octahedral Cu_2O nanocrystals demonstrate superior methyl orange degradation efficiency by optimizing surface interactions via [110] facet exposure, outperforming their cubic and decahedral counterparts (**Figure 10a,b**). Similarly, disk-shaped Fe_2O_3 nanoparticles, as shown in Figure 10c, exhibit enhanced Rhodamine B degradation relative to cubic and mixed cubic-disk morphologies, driven by high-energy crystal planes and surface hydroxyl functionalities.[309,310] The g-C_3N_4/TiO_2 nanocomposite, featuring various morphologies such as nanotubes, exhibits enhanced Rhodamine B degradation due to

© 2024 The Author(s). Advanced Sustainable Systems published by Wiley-VCH GmbH

23667486, 2024, 12, Downloaded from https://advanced.onlinelibrary.wiley.com/doi/10.1002/adsu.202400483 by Nazarbayev University, Wiley Online Library on [08/07/2025]. See the Terms and Conditions (https://onlinelibrary.wiley.com/terms-and-conditions) on Wiley Online Library for rules of use; OA articles are governed by the applicable Creative Commons License

Table 6. Characteristics of 23 excellent performing materials out of the 169 analyzed.

No.	Photocatalysts	Synthesis	Light source	% of adsorption	Main active species	Mechanism	Refs.
1	TiO_2/GO	Hydrothermal	UV	–	O_2•–	–	[126]
2	TiO_2/GO, GR	Hydrothermal	UV	–	–	–	[123]
3	WO_3/rGO	Hydrothermal	Visible	–	HO•	Direct electron transfer	[163]
4	TiO_2–rGO	UV-assisted photocatalytic reduction	UV	–	–	–	[227]
5	TiO_2/GO	Hydrothermal	UV	≤5	h+, HO•, and HOO•	–	[229]
6	SnO_2–rGO	Hydrothermal-assisted ultraviolet Irradiation	UV	–	HO• and O_2•–	Direct electron transfer	[191]
7	$BiVO_4$/rGO aerogel	Hydrothermal followed by freeze-drying	UV	–	–	Direct electron transfer	[236]
8	GO/TiO_2	Chemical precipitation and heat treatment	UV	–	–	–	[237]
9	GO/TiO_2	Surface functionalization	UV	–	–	–	[170]
10	ZnO/GO	Hydrothermal	UV	–	–	–	[134]
11	ZnO/GO	Ultrasonication and chemical reduction	UV	–	•OH and O_2•–	Direct electron transfer	[135]
12	Bi_2WO_6/Nb_2CT_x	Hydrothermal	Visible	–	h+, •OH, and O_2•–	Schottky junction	[162]
13	TiO_2/Ti_3C_2	Hydrothermal	UV	≤5	–	–	[241]
14	BiOBr/Ti_3C_2	Electrostatic self-assembly	Visible	20	h+, •OH, and O_2•–	Schottky junction	[155]
15	$Bi_{0.9}La_{0.1}Fe_{0.95}Mn_{0.05}O_3$/$Ti_3C_2$	Double solvent sol–gel	Visible	93	•OH and O_2•–	Direct electron transfer	[246]
16	MoS_2/ZnO	Hydrothermal	UV	–	h+, HO•, and HOO•	Heterojunction Type II	[124]
17	MoS_2/TiO_2	Hydrothermal	UV	40	h+, •OH, and O_2•–	Direct electron transfer	[218]
18	ZrO_2/MoS_2	Precipitation	UV	0	h+ and O_2•–	Heterojunction Type I	[152]
19	MoS_2/$MnFe_2O_4$	Hydrothermal	Visible	–	h+, •OH, and O_2•–	Electrons and holes transfer	[150]
20	BiOI/Fe_3O_4@GO	Chemical coprecipitation	Visible	30	h+ and •OH	Electrons and holes transfer aided by GO	[147]
21	AgNPs/TiO_2/$Ti_3C_2T_x$	Hydrothermal	UV	0	h+ and O_2•–	Charge transfers from TiO_2 to MXene and then to AgNPs	[128]
22	CoO@TiO_2/$Ti_3C_2T_x$	Facial sonication–hydrothermal	Visible	–	SO_4•–, O_2•–, and $^1O_2$	Z-scheme heterojunction	[289]
23	Bi_2S_3/MoS_2/TiO_2	Microwave-assisted hydrothermal	Natural sunlight	0	O_2•–	Dual Z-scheme heterojunction	[183]

increased surface area and light absorption. Similarly, Ag_3PO_4 particles with rhombic dodecahedron and branched shapes demonstrate superior performance under visible light, attributed to their reactive facets and an optimal Ag^0 to Ag^+ surface ratio, surpassing spherical, cubic, and tetrahedral forms.[311,312] Hexagonal and spherical ZnO nanoparticles enhance methyl orange photodegradation due to increased interstitial spaces.[313] Similarly, TiO_2 nanozigzag structures improve organic dye degradation through their large surface area and oxygen vacancies,[314] while WO_3 nanoplates with cubic shapes nearly achieve complete Rhodamine B degradation by increasing reactive site density (Figure 10d). This increased activity is attributed to the exposure of a more significant proportion of polar (001) and (001) faces on the plate-like particles, which are more active than the nonpolar faces found on the rod-shaped particles, as depicted in Figure 10e.[315] Furthermore, hexagonal plate-like ZnO nanoparticles decompose methylene blue more effectively by exposing polar faces that boost hydroxyl radical production, as shown in Figure 10f,g.[316] In addition, daisy-shaped TiO_2 composites excel in Direct Blue degradation due to their hierarchical structure and lower bandgap energy.[317] Finally, flower-like TiO_2 structures with high rutile content enhance methylene blue degradation by improving charge separation and reducing electron–hole recombination.[318] This study reveals that irregularly shaped 2D-MO NPs (Figure 10h), with their asymmetric surfaces, excel in pollutant degradation due to their larger surface area, enhanced light scattering, and better charge carrier separation, which collectively reduce electron–hole recombination. Conversely, 2D-MO NCs, as depicted in Figure 10i, with regular shapes, particularly spherical ones, show superior performance by facilitating efficient charge transfer, providing structural stability, and ensuring uniform light absorption, which boosts their overall effectiveness. In contrast, rod-shaped composites exhibit the poorest performance, likely because of the challenges in light penetration and uneven charge transport, resulting in higher recombination rates.

4.3. Light Source

Photocatalytic processes depend on light energy to generate electron–hole pairs within a photocatalytic material's conduction and valence bands. This occurs when photons with energy equal to or greater than the material's bandgap are absorbed.[319,320] The

© 2024 The Author(s). Advanced Sustainable Systems published by Wiley-VCH GmbH

23667486, 2024, 12, Downloaded from https://advanced.onlinelibrary.wiley.com/doi/10.1002/adsu.202400483 by Nazarbayev University, Wiley Online Library on [08/07/2025]. See the Terms and Conditions (https://onlinelibrary.wiley.com/terms-and-conditions) on Wiley Online Library for rules of use; OA articles are governed by the applicable Creative Commons License

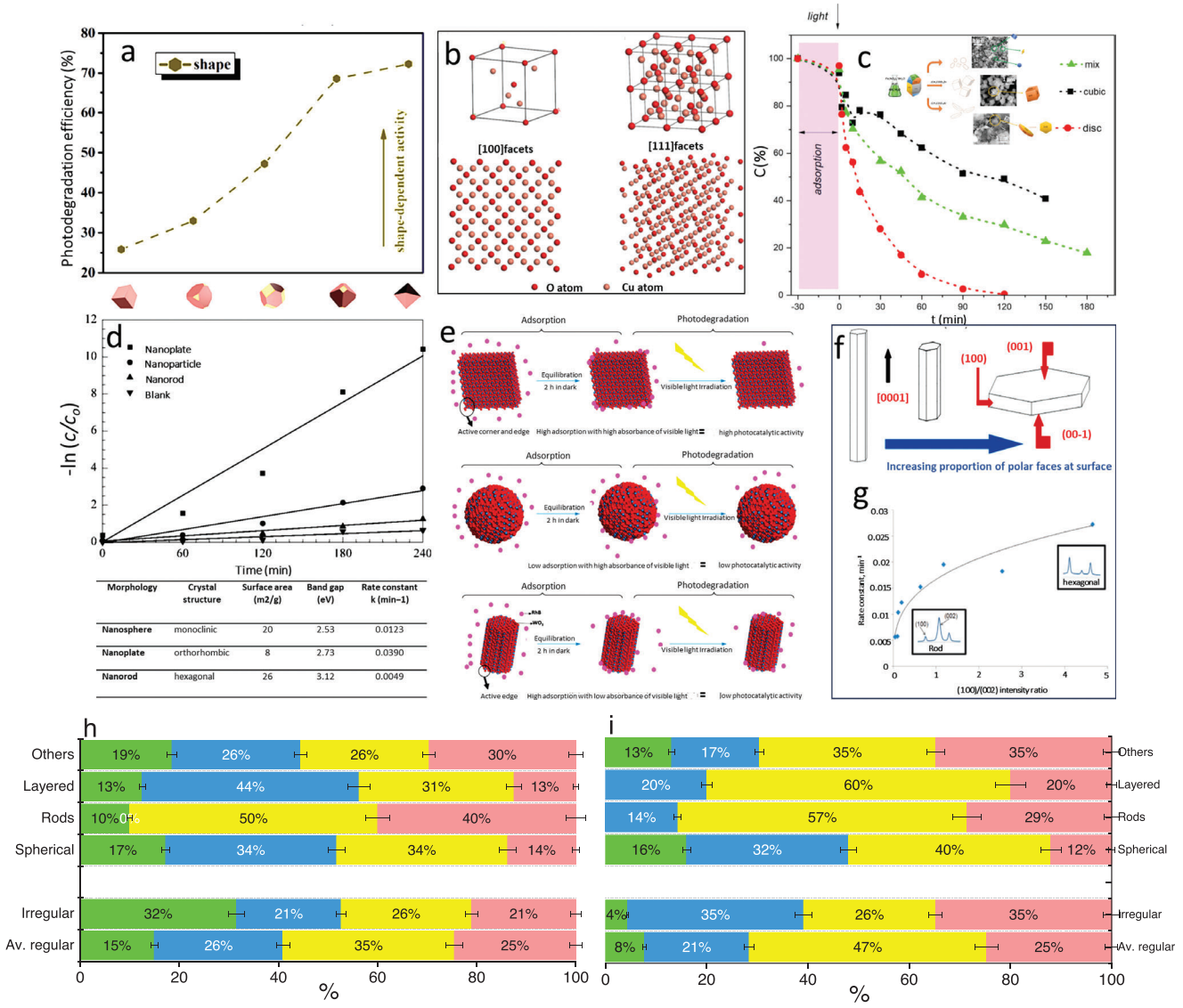

Figure 10. a,b) Shape-dependent photocatalytic activity and crystal structure of Cu_2O: crystal models of the [99] and [110] facets. Reproduced with permission.[309] Copyright 2023, Elsevier. c) Photocatalytic activity of various shaped Fe_2O_3 nanoparticles. Reproduced with permission.[310] Copyright 2023, Elsevier. d) Kinetic analysis of RhB photodegradation: Rate constant (k) determination using WO_3 nanoarchitectures and their physical properties, and e) schematic illustration of shape influence on WO_3 nanostructures' photocatalytic activity. Reproduced with permission.[315] Copyright 2015, Elsevier. f) Diagram showing dominant facets on the surfaces of NPs with different shapes, and g) plot of rate constants versus (100)/(002) intensity ratio. Reproduced with permission.[316] Copyright 2009, American Chemical Society. h,i) Shape-dependent photocatalytic activity of 169 2D-metal oxide nanoparticles (NPs) and nanocrystals (NCs).

choice of a light source is crucial in photocatalysis as it determines the wavelength and intensity of light that interacts with the photocatalyst, thus significantly affecting its performance. UV light is often favored owing to its high energy and the efficient activation of various photocatalysts. Additionally, solar light, which includes a broad spectrum of UV (5%), visible (45%), and infrared light (50%), is precious due to its resemblance to natural sunlight and practical usability.[321,322] In their experimental studies conducted under UV and solar light, Othman et al. chose ratios of 2.5:1 and 20:1 for the photocatalyst to methylene blue and Rhodamine B, respectively. It is worth noting that despite using a significantly more significant amount of photocatalyst, the reaction rate was slower in the solar light experiments compared to the UV light experiments, as shown in **Figure 11**a,b.[128] Two main factors contribute to this phenomenon. The configuration used in UV light experiments enables more efficient light capture than those utilizing a solar simulator, and the synthesized catalysts show stronger absorption in the UV spectrum than in the visible range.[323] Similarly, the investigation conducted by Simsek et al. demonstrated the effectiveness of $rGO/TiO_2/ZnO$ in decomposing bisphenol A, Ibuprofen, and flurbiprofen under both UV-A and visible light. The apparent rate constant (k_{app}) values range from 5.286×10^{-2} to 9.356×10^{-2} min^{-1}. It is worth noting that the performance is slightly superior under UV-A light, as

© 2024 The Author(s). Advanced Sustainable Systems published by Wiley-VCH GmbH

23667486, 2024, 12, Downloaded from https://advanced.onlinelibrary.wiley.com/doi/10.1002/adsu.202400483 by Nazarbayev University, Wiley Online Library on [08/07/2025]. See the Terms and Conditions (https://onlinelibrary.wiley.com/terms-and-conditions) on Wiley Online Library for rules of use; OA articles are governed by the applicable Creative Commons License

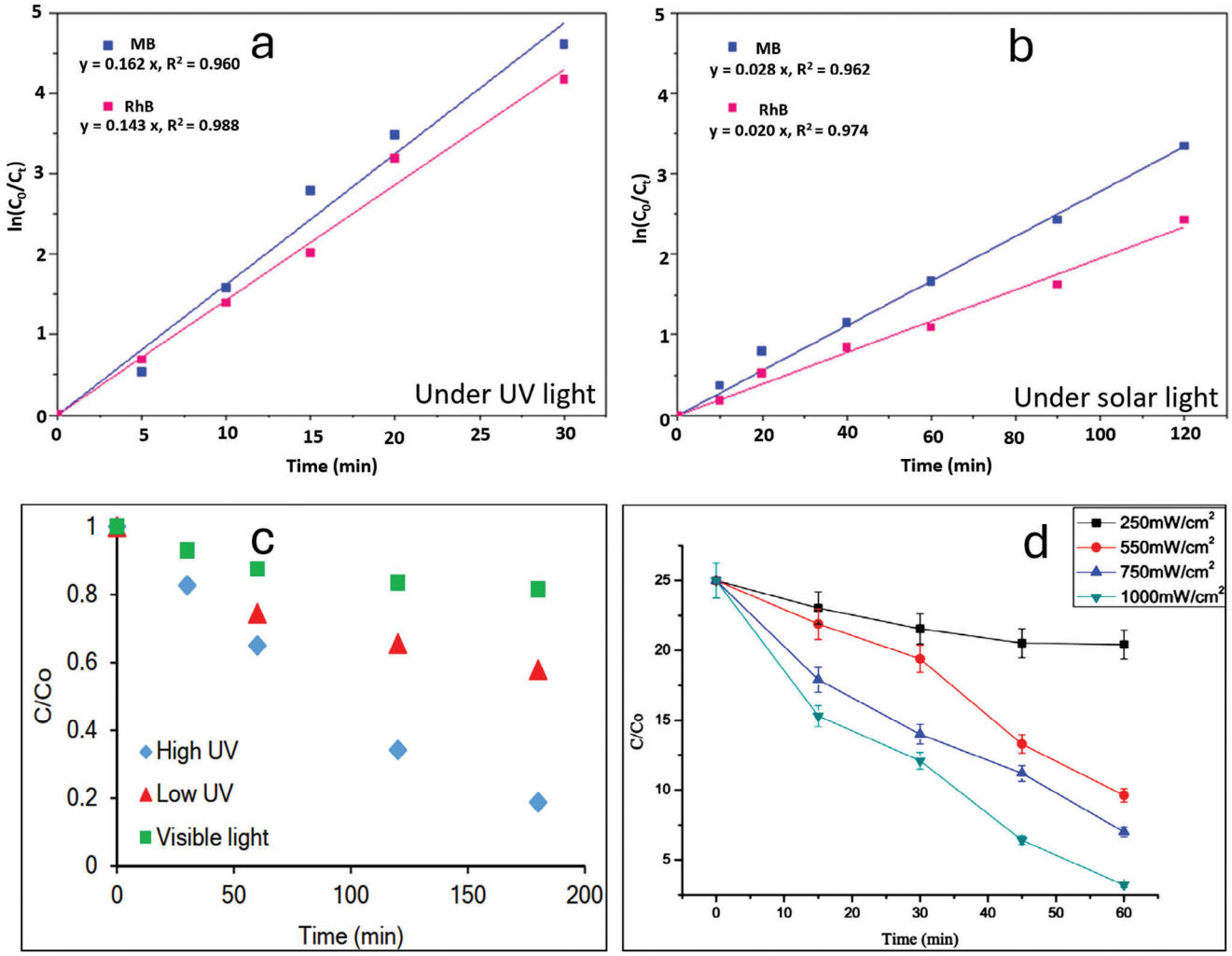

Figure 11. Comparative kinetic trends of methylene blue and Rhodamine B photodegradation under a) UV and b) solar light using AgNPs/TiO_2/$Ti_3C_2T_x$. Reproduced with permission.[128] Copyright 2021, ACS. c) Effect of light sources and intensity on the photoremoval of ibuprofen using TiO_2–rGO/SOFs composites and d) influence of light conditions on atenolol photoremoval with TiO_2–GO nanostructures. Reproduced with permission.[230,324] Copyright 2017, Elsevier.

higher k_{app} values are observed for the degradation of ibuprofen and flurbiprofen compared to visible light irradiation.[164] In their study, Lin et al. observed a significant enhancement in removing ibuprofen when exposed to high-intensity UV light conditions (Figure 11c).[324] In addition, Bhatia et al. reported a considerable increase in the photodegradation of atenolol with higher light intensity (Figure 11d).[230] In this study, the materials that performed in the "excellent" category, UV light sources, played a significant role in driving these catalytic reactions. Table 6 shows that 67% of the composites worked better under UV, 29% under visible, and 4% under sunlight.

4.4. Loading, Composition, and Intermediates

The functional groups and the abundance of both species influence the interaction between a pollutant molecule and a photocatalyst. The specific type of the pollutant determines the optimal concentration. Higher pollutant concentrations can hinder the degradation efficiency by competing for active sites. Furthermore, elevated pollutant concentrations can impede photocatalysis by absorbing a more significant amount of light, thereby limiting the penetration of photons to the catalyst surface. Consequently, the presence of free radicals, crucial for degrading dye molecules, is reduced.[35] The presence of metal ions in dye solutions significantly impacts the performance of photocatalysts. The efficiency of dye treatment depends on the specific structural characteristics of the dye, as outlined in **Table 7**. This variability is influenced by the ionic nature of the dye molecules, which directly affects the adsorption of metal ions onto the surface of the photocatalyst. As a result, the charge of the photocatalyst is modified, leading to changes in the interaction between the dye molecules and the catalyst surface. Ultimately, this modification affects the catalyst's capacity to enhance or hinder the degradation of the dye.[139,325] Furthermore, these variations in degradation rates can likely be ascribed to how they

© 2024 The Author(s). Advanced Sustainable Systems published by Wiley-VCH GmbH

23667486, 2024, 12, Downloaded from https://advanced.onlinelibrary.wiley.com/doi/10.1002/adsu.202400483 by Nazarbayev University, Wiley Online Library on [08/07/2025]. See the Terms and Conditions (https://onlinelibrary.wiley.com/terms-and-conditions) on Wiley Online Library for rules of use; OA articles are governed by the applicable Creative Commons License

Table 7. Variation in dye treatment efficiency based on dye characteristics by $CoFe_2O_4$–GR nanostructure.

Pollutants	Structure	Removal efficiency [%]	Kinetic Rxn rate	QY	Energy consumption	FOM	Refs.
Rhodamine B	$C_{28}H_{31}ClN_2O_3$	94	39	1.3×10^{-7}	510	1.96	[139]
Methyl orange	$C_{14}H_{14}N_3NaO_3S$	71	43	1.4×10^{-7}	461	2.17	
Active black	$C_{69}H_{117}N_9O_6RuS_3$	66	13	4×10^{-8}	1503	0.67	
Active red	$C_{18}H_{14}N_2Na_2O_8S_2$	61	20	7×10^{-8}	1009	0.99	
Methylene blue	$C_{16}H_{18}N_3SCl$	100	63	2.1×10^{-7}	320	3.13	

interact with metal nanoparticles. Methylene blue, renowned for its core composed of nitrogen and sulfur atoms, exhibits a notable affinity toward metals. Conversely, Rhodamine B tends to adhere to metal surfaces and carbon materials owing to the existence of its carboxylic and amino groups.[326,327] Othman et al. highlighted the augmented negative charge density of MXene composites in an aqueous solution, thereby enhancing the effective uptake of cationic dyes such as methylene blue. In contrast, both positive and negative charges in the structure of Rhodamine B may lead to less robust electrostatic interactions with MXene composites.[128] Moreover, the research findings suggest that the degradation of these dyes leads to the formation of intermediate compounds. In the case of methylene blue dye, the intermediate compounds produced include azure A, azure B, azure C, and thionin. Similarly, Rhodamine B dye generates ethanedioic acid, 1,2-benzenedicarboxylic acid, 4-hydroxybenzoic acid, and benzoic acid as intermediate products. These intermediate substances then compete with the initial dyes for binding sites on the surface of the photocatalyst.[328,329] **Figure 12** shows that 2D-MO NPs perform better than 2D-MO NCs in all scenarios. Also, the graph indicates that these composites excel at removing smaller pollutants such as formaldehyde, dichloroacetic acid, phenol, salicylic acid, aniline, and bisphenol. Conversely, dyes and antibiotics, which are larger and more complex, are more difficult to remove, with antibiotics being the most challenging.

4.5. Impact and Dynamics of Catalysts on Adsorption

The photocatalyst concentration in a wastewater suspension significantly impacts the reaction rate and dye degradation efficiency. Balarabe et al. conducted experiments using different concentrations (0.05, 0.15, 0.25, 0.5, and 0.75 ppm) of rGO-modified Ag@ZnO nanocomposite. The results showed that higher catalyst concentrations resulted in increased methylene blue removal.[35] The drop-in removal rate at higher composite concentrations is attributed to increased turbidity, resulting in more significant light scattering and reduced penetration into the reaction mixture. Higher photocatalyst loading accelerates dye molecule degradation by generating additional electron–hole pairs. However, excessively high concentrations may induce nanoparticle coagulation, leading to decreased surface area and hindrance of the process.[159,279] Furthermore, degradation's efficacy relies on the catalyst surface's adsorptive capacity toward dye molecules, governed by electrostatic interactions and binding affinity. Maintaining a moderate level of adsorption is crucial to maximize the synergistic effects between adsorption and photocatalysis, thereby optimizing the degradation process. Composite materials possessing favorable adsorptive properties exploit this interaction, enabling the concurrent adsorption and degradation of dye molecules.[330] For example, graphene nanocomposites demonstrate remarkable adsorption capabilities due to

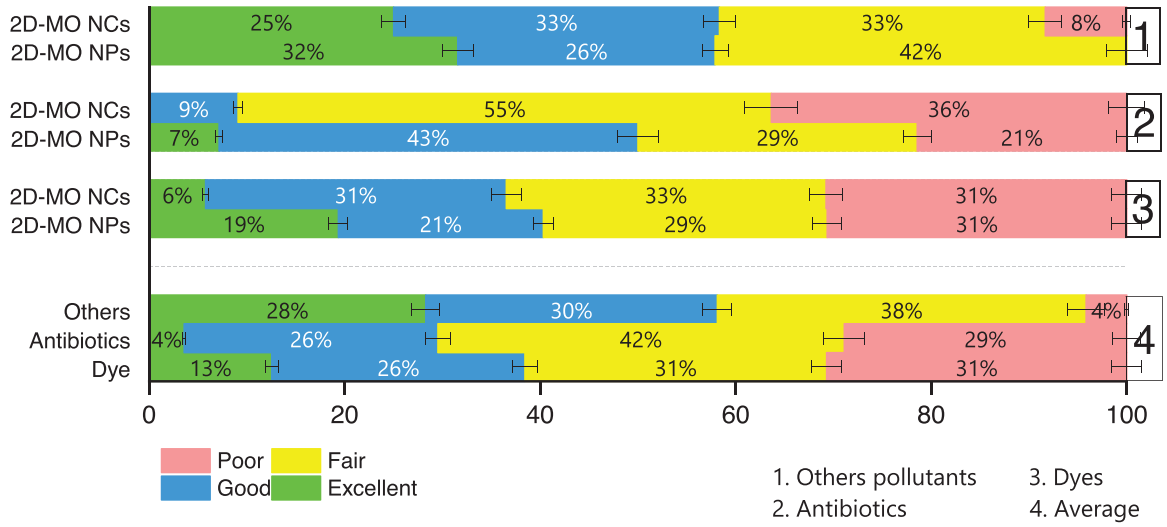

Figure 12. Comparison of 2D-MO NPs and NCs in removing small versus large pollutants.

© 2024 The Author(s). Advanced Sustainable Systems published by Wiley-VCH GmbH

23667486, 2024, 12, Downloaded from https://advanced.onlinelibrary.wiley.com/doi/10.1002/adsu.202400483 by Nazarbayev University, Wiley Online Library on [08/07/2025]. See the Terms and Conditions (https://onlinelibrary.wiley.com/terms-and-conditions) on Wiley Online Library for rules of use; OA articles are governed by the applicable Creative Commons License

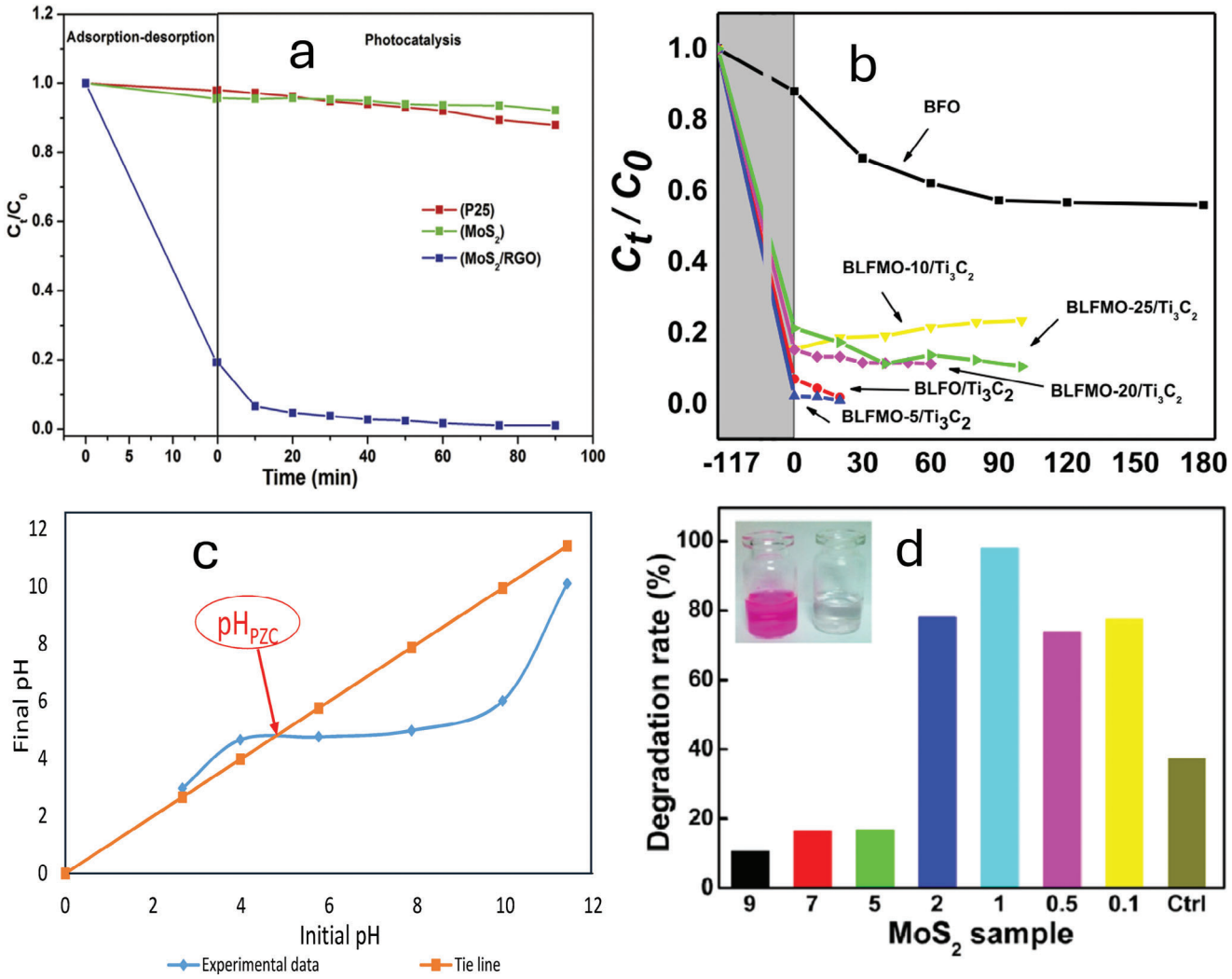

Figure 13. a,b) Proportion of total removal attributed to methylene blue and Congo red adsorption by respectively rGO/MoS_2. Reproduced with permission.[333] Copyright 2017, Elsevier. $Bi_{0.9}La_{0.1}Fe_{0.90}Mn_{0.10}O_3$. Reproduced with permission.[246] Copyright 2019, ACS Omega. c) pH_{PZC} determination technique using the pH drift method. Reproduced under the terms of the CC-BY license.[339] Copyright 2020, The Authors, published by MDPI. d) RhB degradation rates of MoS_2 photocatalyst produced under different pH values. Reproduced with permission.[341] Copyright 2017, Elsevier.

residual oxygen functional groups and defect vacancies.[331] The study conducted by Anwer and Park demonstrated that the nanocomposite consisting of rGO/ZrO_2/Ag_3PO_4 exhibited the capability to remove ≈50% of 4-nitrophenol through the process of adsorption. Moreover, including rGO in the ZrO_2/Ag_3PO_4 composite led to a notable improvement of 16% in the adsorption efficiency.[332] Yuan et al. conducted a study demonstrating the superior adsorption efficiency of reduced graphene oxide when combined with MoS_2 (**Figure 13a**),[333] which showed an adsorption rate of 80% for methylene blue. Similarly, MXene was also highly effective in reducing the concentration of Congo red, achieving a reduction of ≈93% even without exposure to light. Figure 13b illustrates emphasizes the efficacy of MXene as an adsorbent in photocatalysis.[246] Hence, the absence of adsorption data in some cases suggests it may not always be necessary for material performance. Photodegradation results are influenced by the wide range of composite adsorption, which varies between 0% and 93%. While surface adsorption of dyes is crucial for dye degradation in photocatalysis, excessive concentration can have negative consequences. Beyond a specific concentration, it hinders the accessibility of photons to active sites on the surface. Moreover, dye molecules can act as sensitizers, absorbing and deflecting electrons in unfavorable directions.[334]

4.6. Effect of pH

pH plays a complex role in the photocatalytic degradation of organic pollutants, as different dyes impact the reaction uniquely. To maximize degradation efficiency, it is essential to determine the optimal pH for each system.[335] The degradation of dyes is significantly influenced by the pH of the solution, with the pollutant's point of zero charges (pH_{pzc}) playing a critical role in determining the outcome.[336] Below the pH_{pzc}, the surface of the pollutant becomes positively charged, facilitating its interaction with anionic dyes. Beyond this limit, the surface charge is reversed.[36]

© 2024 The Author(s). Advanced Sustainable Systems published by Wiley-VCH GmbH

23667486, 2024, 12, Downloaded from https://advanced.onlinelibrary.wiley.com/doi/10.1002/adsu.202400483 by Nazarbayev University, Wiley Online Library on [08/07/2025]. See the Terms and Conditions (https://onlinelibrary.wiley.com/terms-and-conditions) on Wiley Online Library for rules of use; OA articles are governed by the applicable Creative Commons License

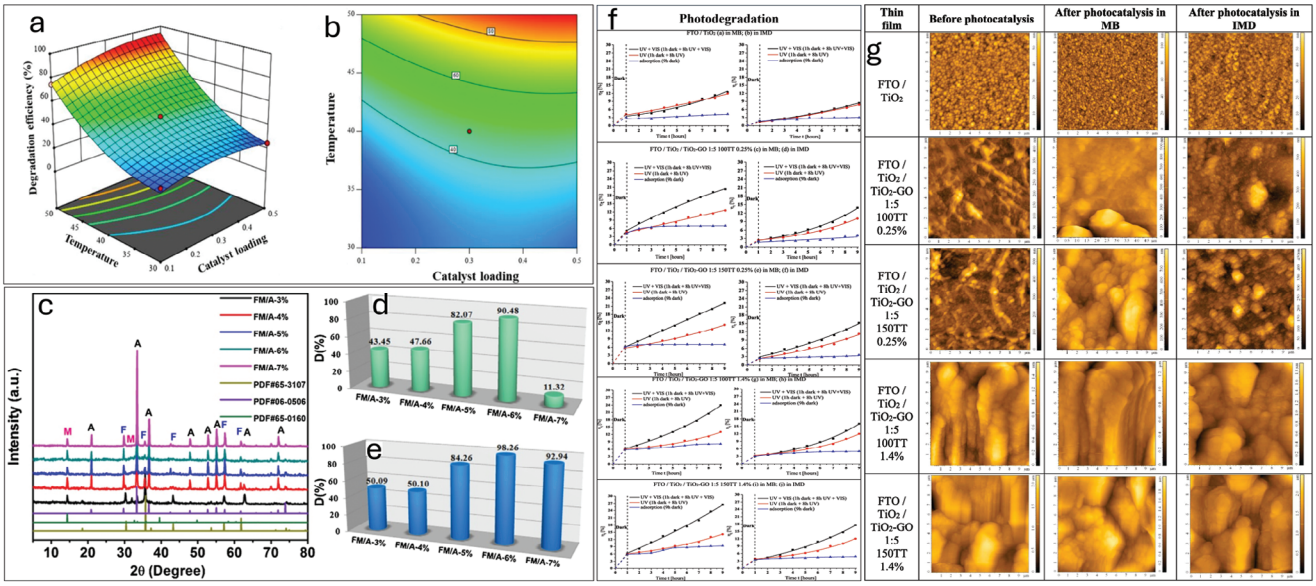

Figure 14. a,b) Temperature optimization for tartrazine degradation with response surface methodology. Reproduced with permission.[343] Copyright 2017, Elsevier. c) XRD patterns of FM/A-*x*% (*x*: 3–7%, M: MoS_2, F: Fe_3O_4, A: Ag_3PO_4), and d,e) effect of Ag_3PO_4-loaded content on the degradation of Congo red and Rhodamine B, respectively. Reproduced with permission.[214] Copyright 2016, Elsevier. f,g) Efficiency of MB and IMD removal on thin films under different light conditions and the corresponding AFM images showing the composites roughness. Reproduced with permission.[202] Copyright 2021, Elsevier.

Balarabe et al. determined that the pH_{pzc} of Ag@ZnO@rGO is ≈8, resulting in a positive surface charge. At pH values below 8, the presence of reduced H_3O^+ ions enhances the adsorption of MB. Conversely, at pH values above 8, the increased concentration of OH^- ions decreases it. The optimal pH for MB adsorption was identified as 10.[35] The study conducted by Mzimela et al. examined the pH-dependent adsorption and photodegradation mechanisms of Rhodamine B.[337] The pH_{PZC} on a catalyst surface can be determined using various techniques, including mass titration, potentiometric titration, immersion technique, and pH drift method.[338] Among them, the pH drift method is widely used and considered reliable based on previous research. In the pH drift method, the pH of a NaCl solution is adjusted from pH 2 to 11 using either NaOH or HCl. A specific volume of this solution is then mixed with a predetermined amount of the material in Erlenmeyer flasks. The flasks are sealed and agitated for 4 h at 150 rpm. The final pH (pHf) is recorded, and the difference between the initial (pHi) and final pH values (ΔpH = pHi − pHf) is plotted against pHi to determine the pH_{PZC}, as shown in Figure 13c.[339,340] Subsequently, the pH level is considered a crucial factor in determining the morphology of the nanocomposites. For instance, Wang et al. conducted a study to examine this correlation and found that a decrease in pH led to a reduction in the size of MoS_2 microflowers. This alteration significantly impacted the degradation of RhB, as depicted in Figure 13d of their research.[341]

4.7. Other Parameters

Temperature has a significant impact on the degradation of dyes in photocatalytic processes. As the temperature increases, various factors are affected, such as the solubility and mobility of dye molecules and the interaction with adsorbents.[342] Soufi et al. conducted a study to examine the effect of temperature on the efficiency of tartrazine degradation. They applied response surface methodology with a Box-Behnken design to create and confirm a quadratic model. This optimization process revealed that the most effective degradation occurred at a temperature of 49.92 °C (**Figure 14**a,b).[343] In addition, the catalyst loading composition has an impact on the properties of the nanostructure.[344] It is crucial to determine the optimal loading, as it directly affects the enhancement of photocatalytic activity and ensures efficient degradation of pollutants. The X-ray diffraction analysis of Fe_3O_4@MoS_2/Ag_3PO_4 nanocomposites (Figure 14c) revealed distinct peaks corresponding to Ag_3PO_4, Fe_3O_4, and MoS_2. The photocatalytic performance improved with increasing Ag_3PO_4 content by up to 6%. However, further increments reduced efficiency due to challenges separating electron–hole pairs (Figure 14d,e).[214] Tismanar et al. estimate that a higher GO content (1.4%w) in the composites led to increased crystallinity, improving charge carrier mobility and reducing electron–hole recombination.[202] However, Mzimela et al. present an alternative perspective, emphasizing the importance of temperature optimization in promoting the process of photocatalytic degradation. In their investigation of the photodegradation of Rhodamine B at various temperatures (300, 500, and 700 °C), they found that the most efficient removal of the dye (78.4%) was achieved at 300 °C, with only limited photodegradation observed at higher temperatures.[337] Although higher crystallinity is typically linked to better photocatalytic performance, exceeding a specific limit can reduce effectiveness.[345] In addition, the photocatalytic efficiency of the composite is closely related to its surface roughness. For instance, TiO_2–GO films

© 2024 The Author(s). Advanced Sustainable Systems published by Wiley-VCH GmbH

23667486, 2024, 12, Downloaded from https://advanced.onlinelibrary.wiley.com/doi/10.1002/adsu.202400483 by Nazarbayev University, Wiley Online Library on [08/07/2025]. See the Terms and Conditions (https://onlinelibrary.wiley.com/terms-and-conditions) on Wiley Online Library for rules of use; OA articles are governed by the applicable Creative Commons License

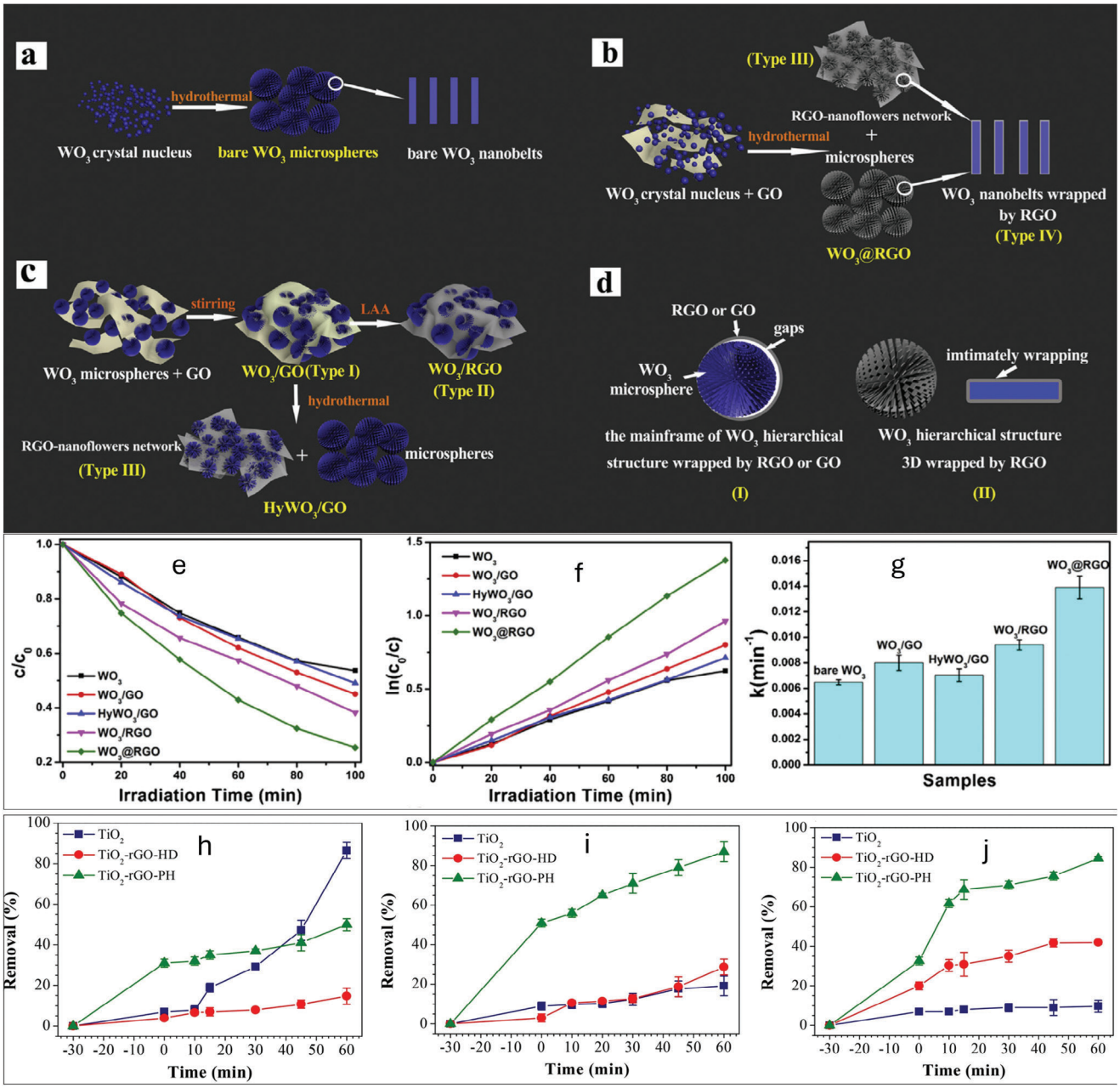

Figure 15. Exploring contact interfaces between rGO/GO and WO_3: formation mechanisms of a) bare WO_3, b) 1.2% WO_3@rGO, c) WO_3/GO, WO_3/rGO, and $HyWO_3$/GO, d) hierarchical structures of WO_3 wrapped by rGO or GO (I) and 3D wrapped WO_3 by rGO (II), and e–g) photocatalytic removal of Rhodamine B by various composites. Reproduced with permission.[163] Copyright 2016, Elsevier. Photocatalytic degradation of h) sulfamethoxazole, i) clarithromycin, and j) erythromycin. Reproduced with permission.[231] Copyright 2018, Elsevier.

with a higher GO content (1.4%w) develop rougher surfaces, with roughness values ranging from 82.0 to 313.1 nm. This increased roughness enhances the films' ability to adsorb pollutants like methylene blue (MB) and imidacloprid (IMD), resulting in better removal efficiency under UV and visible light. Conversely, films with a lower GO content (0.25%w) have smoother surfaces, leading to less effective pollutant removal, as shown in Figure 14f,g.[202] Similarly, integrating TiO_2 nanoparticles in the MXene–PVA–TiO_2@PVDF membrane boosts its roughness, producing better photocatalytic performance.[204] Likewise, the NiO–MoS_2@PANI film sees a rise in photocatalytic activity attributed to the added reaction sites generated by increased surface roughness.[203]

The synthesis method is also a crucial factor that can significantly impact efficiency. Li et al. conducted a study to investigate the influence of different synthesis methods on the pollutant removal efficiency of graphene-based composite materials. Four types of graphene-based composites, namely,

© 2024 The Author(s). Advanced Sustainable Systems published by Wiley-VCH GmbH

23667486, 2024, 12, Downloaded from https://advanced.onlinelibrary.wiley.com/doi/10.1002/adsu.202400483 by Nazarbayev University, Wiley Online Library on [08/07/2025]. See the Terms and Conditions (https://onlinelibrary.wiley.com/terms-and-conditions) on Wiley Online Library for rules of use; OA articles are governed by the applicable Creative Commons License

Table 8. Different heterojunction mechanisms in photocatalysis using 2D nanomaterials.

Mechanism	Graphene-based materials		MXene-based materials		MoS_2-based materials	
Heterojunction Type I	NiO–CuO–RGO Brilliant green, UV–vis	[273]	$CuFe_2O_4$/MXene Methylene blue, vis	[210]	CDs/MoS_2@H-TiO_2 Tetracycline, near-infrared	[296]
	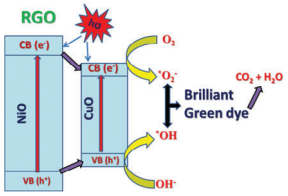		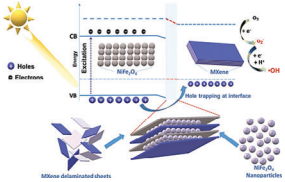		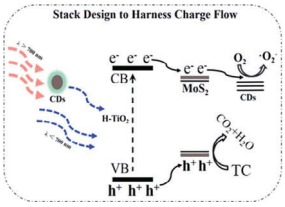	
Heterojunction Type II	$BiVO_4$/$BiPO_4$/GO Reactive Blue-19, vis	[272]	BiOBr/TiO_2/$Ti_3C_2T_x$ Rhodamine B, vis	[194]	MoS_2/BiOBr Rhodamine B, vis	[154]
	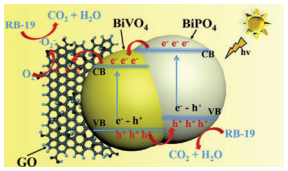		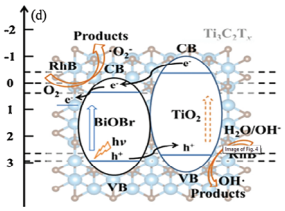		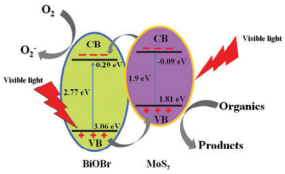	
Z-scheme heterojunction	g-C_3N_4/rGO/WO_3 Ciprofloxacin, vis	[265]	CoO@TiO_2/MXene Phenol, vis	[289]	Ag_3PO_4/MoS_2 Phenol, simulated solar	[252]
	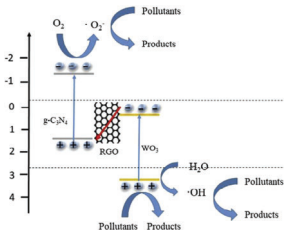		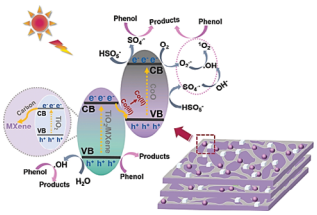		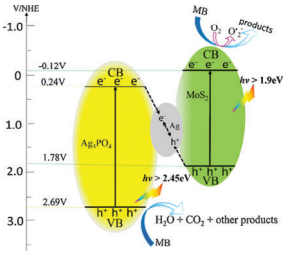	
Diode junction	Cu_2O–rGO Methyl orange, vis n-Type Schottky junction	[185]	Ag_3PO_4/Ti_3C_2 Tetracycline, vis n-Type Schottky junction	[141]	MoS_2/BiOBr Reactive Black 5, saving bulb n-Type Schottky junction	[261]
	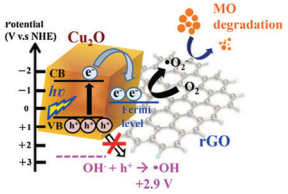		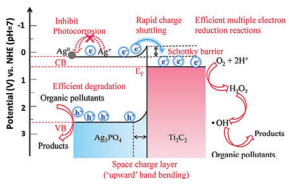		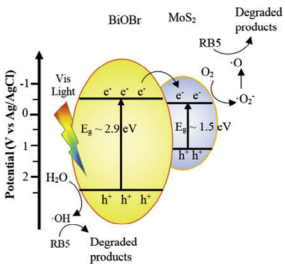	
	Au@TiO_2–GR Acid Blue-92, vis n-Type Schottky junction	[280]	(001)TiO_2/Ti_3C_2 Methyl orange, UV p-Type Schottky junction	[188]	Bi_2WO_6@MoS_2/graphene Rhodamine B, vis p-Type Schottky junction	[300]
	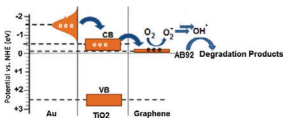		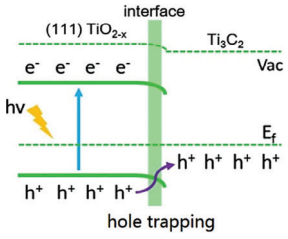		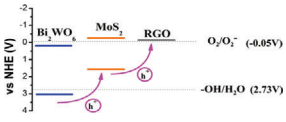	

(*Continued*)

© 2024 The Author(s). Advanced Sustainable Systems published by Wiley-VCH GmbH

23667486, 2024, 12, Downloaded from https://advanced.onlinelibrary.wiley.com/doi/10.1002/adsu.202400483 by Nazarbayev University, Wiley Online Library on [08/07/2025]. See the Terms and Conditions (https://onlinelibrary.wiley.com/terms-and-conditions) on Wiley Online Library for rules of use; OA articles are governed by the applicable Creative Commons License

Table 8. (Continued)

Mechanism	Graphene-based materials	MXene-based materials	MoS_2-based materials
			MoS_2@ZnO [137] Methylene blue, UV–vis p–n junction 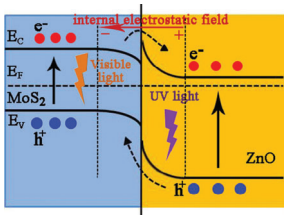

Table 9. Different modified heterojunction mechanisms in photocatalysis using 2D nanomaterials.

Heterojunction Type II	$BiVO_4/TiO_2$/rGO [351] Tetracycline, vis 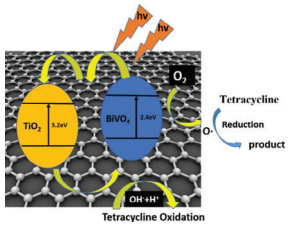	α-$Fe_2O_3/ZnFe_2O_4@Ti_3C_2$ [213] Rhodamine B, vis 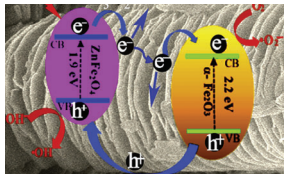	$Bi_2S_3/MoS_2/Bi_2MoO_6$ film electrode [352] Rhodamine B, vis 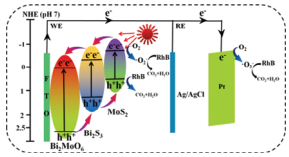	
Z-scheme heterojunction	MoS_2/g-$C_3N_4/Bi_{24}O_{31}Cl_{10}$ [299] Tetracycline, vis 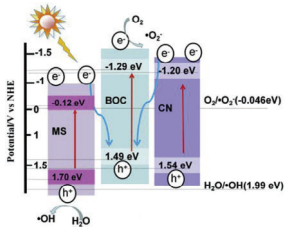	$Ag_3PO_4/Ag/MoS_2/TiO_2$ [181] Methylene blue, sunlight 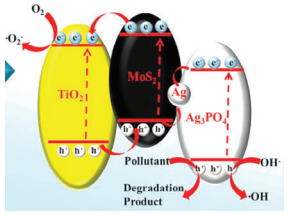	Ag@AgBr/$BiPO_4$/rGO [275] Reactive Blue-19, vis 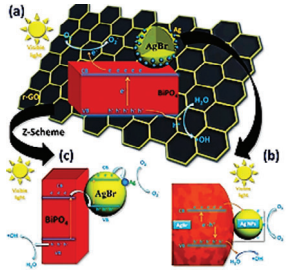	
Diode junction	$BiVO_4/Bi_2S_3/MoS_2$ Rhodamine B, sunlight 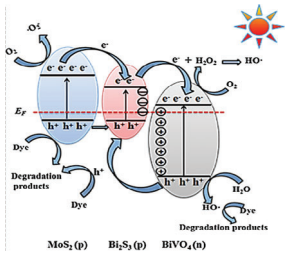	$Ti_3C_2T_x/TiO_2$–BP [53] Rhodamine B, vis 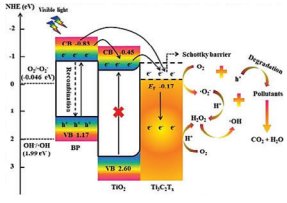	TiO_2@Ti_3C_2/g-C_3N_4 [283] Rhodamine B, vis 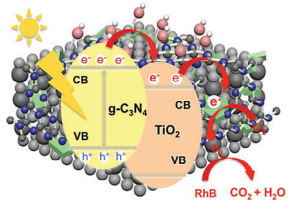	

© 2024 The Author(s). Advanced Sustainable Systems published by Wiley-VCH GmbH

23667486, 2024, 12, Downloaded from https://advanced.onlinelibrary.wiley.com/doi/10.1002/adsu.202400483 by Nazarbayev University, Wiley Online Library on [08/07/2025]. See the Terms and Conditions (https://onlinelibrary.wiley.com/terms-and-conditions) on Wiley Online Library for rules of use; OA articles are governed by the applicable Creative Commons License

WO_3/GO, HyWO_3/GO, $WO_3/_R$GO, and $WO_3@_R$GO, were examined. These composites were synthesized using simple mixing, hydrothermal, chemical reduction, and one-step hydrothermal reaction techniques. $WO_3@_R$GO demonstrated the highest efficiency in degrading Rhodamine B (**Figure 15e–g**). It is important to note that conventional methods of preparing graphene composites may not fully exploit the advantages of reduced graphene oxide.[346,347] Encapsulating WO_3 microspheres or nanoflowers with rGO or GO has limitations (Types I–III in Figure 15a–c). However, WO_3@rGO composites (Type IV in Figure 15d) have been found to enhance electron transfer and reduce recombination, thereby promoting closer contact between components.[163] In a study by Karaolia et al., hydrothermal (HD) and photocatalytic (PH) treatments were compared for synthesizing TiO_2–rGO composites. It was discovered that TiO_2–rGO–PH was more effective in degrading antibiotics such as sulfamethoxazole, clarithromycin, and erythromycin, as shown in Figure 15h–j. This was attributed to the increased presence of active sites and improved electron transfer.[231] The results in Table 6 indicate that 65% of the well-performing composites were produced using hydrothermal or hydrothermal-assisted methods, making these the most utilized techniques. Ribao et al., in their study on the removal of dichloroacetic acid using GO/TiO_2 nanocomposites under visible light, suggest that the hydrothermal method allows for more effective coupling, resulting in improved structural properties that could enhance photocatalytic performance.[348]

5. Photodegradation Mechanisms of Organic Pollutants by 2D Materials

Understanding the complex processes involved in the photocatalytic removal of organic pollutants is essential for improving environmental remediation efforts and creating more precise and sustainable pollution control methods. Scavengers are crucial in studying intricate mechanisms involved in photocatalytic degradation processes. In various studies involving different photocatalysts and nanocomposites, researchers have utilized scavengers such as ethylenediaminetetraacetic acid, isopropanol, benzoquinone, oxalic acid, ammonium oxalate, potassium dichromate ($K_2Cr_2O_7$), and others. These scavengers are selectively chosen to target and neutralize specific reactive species, including hydroxyl radicals ($HO^•$), superoxide radicals ($O_2^{•-}$), sulfate radicals ($SO_4^{•-}$), holes (h+), electrons (e_{CB}), and singlet oxygen ($^1O_2$). By observing the impact of scavenger addition on the degradation rates of target pollutants or dyes, researchers gain insights into the roles played by different reactive species in driving photocatalytic degradation processes.[147,218,289] Table 6 outlines the reactive species that play a crucial role in enhancing the performance of these composites. Several classifications have been proposed in the field of degradation mechanisms in 2D materials, each providing valuable insights into different processes and interactions. These classifications include simple charge transfer, Type I heterojunctions, Type II heterojunctions, diode junctions, and Z-scheme heterojunctions. Understanding these mechanisms is essential for interpreting the intricate pathways by which 2D-metal oxides operate. Table 8 presents a range of heterojunction mechanisms proposed for choosing composites made of 2D metal oxides.

- In Type I heterojunction scenarios, semiconductor 1 has higher valence band (VB) and conduction band (CB) positions. The process involves a distinct photocatalytic mechanism where holes and photogenerated electrons from the VB and CB of semiconductor 1 (S1) are transferred to semiconductor 2, leading to efficient charge carrier separation.[349] The studies in **Table 8** focus on Type I heterojunction pathways for the degradation of photocatalytic pollutants, each utilizing specific materials and configurations. Sree et al. use metal oxide–rGO composites to generate radicals through electron excitation. Alsafari et al. emphasize the creation of hole reservoirs using $CuFe_2O_4/Ti_3C_2$ to form hydroxyl radicals. Liu et al. highlight interfacial charge transfer using CDs–MoS_2–H-TiO_2 for enhanced degradation. Despite variations, they all prioritize charge separation, radical generation, and light absorption for effective photocatalysis.[210,273,296]
- In Type II heterojunctions, electrons transition to lower energy levels within the conduction band upon excitation. At the same time, holes move to lower potentials in the valence band within a semiconductor with a different bandgap. The internal electric field plays a crucial role in enhancing the separation and mobility of photogenerated charge carriers.[350] Analysis of Table 8 reveals that all Type II heterojunctions emphasize the importance of synergistic effects resulting from interfacial contact. However, they vary in terms of the combinations of semiconductors and mechanisms involved. Di et al. highlight the synergy between MoS_2 and BiOBr for charge transfer, Xu et al. discuss BiOBr/TiO_2/$Ti_3C_2T_x$ composites, focusing on the wider bandgap of TiO_2 and the role of $Ti_3C_2T_x$. On the other hand, Wang et al. explore $BiVO_4$/$BiPO_4$ heterojunctions with an emphasis on the influence of graphene oxide.[154,194,272]
- In the field of Z-scheme heterojunctions, researchers explore two different approaches: mediator-free and mediated schemes.[289] These schemes involve the integration of electrons from the lower conduction band of semiconductor 2 with the valence band of semiconductor 1. Plasmonic metals, such as Ag and Au, well-known for their exceptional electrical conductivity, are commonly used as electron mediators to facilitate the formation of the Z-scheme.[252,349] Importantly, Lu et al. highlight the enhanced removal process in a Z-scheme g-C_3N_4/rGO/WO_3 composite, where rGO serves as the driving force (Table 8).[266]
- A diode junction, whether a p–n heterojunction or a Schottky junction (Table 8), refers to the interface between two semiconductor materials. Typically, one material is p-type while the other is n-type. When an external electric field is applied, these junctions separate and direct charge carriers (electrons and holes) to flow in a preferred direction. The mechanisms outlined in the section on diode junctions present various strategies for enhancing the degradation of photocatalytic dyes. These strategies include scavenging photoexcited electrons in Cu_2O–rGO,[185] promoting efficient carrier transfer in Ag_3PO_4/Ti_3C_2,[141] and the contribution of specific reactive species in MoS_2/BiOBr photocatalysts.[261] Additionally, the discussion covers surface plasmon resonance-induced electron transfer in Au@TiO_2–GR,[280] spatial separation of electron–hole pairs in (001) TiO_2/Ti_3C_2,[188] and the synergistic effects of graphene with MoS_2 or ZnO.[137,300]

© 2024 The Author(s). Advanced Sustainable Systems published by Wiley-VCH GmbH

23667486, 2024, 12, Downloaded from https://advanced.onlinelibrary.wiley.com/doi/10.1002/adsu.202400483 by Nazarbayev University, Wiley Online Library on [08/07/2025]. See the Terms and Conditions (https://onlinelibrary.wiley.com/terms-and-conditions) on Wiley Online Library for rules of use; OA articles are governed by the applicable Creative Commons License

Several integrated techniques have been developed to enhance the photocatalytic degradation of organic pollutants by incorporating multiple mechanisms, as summarized in **Table 9**. For instance, one practical approach is using nanocomposites based on $BiVO_4/TiO_2/rGO$, employing a modified heterojunction type II strategy. The addition of rGO serves various purposes, such as facilitating electron transfer, minimizing charge recombination, and optimizing pollutant removal.[351] In another study, Kang et al. introduced dual Z-scheme $MoS_2/g\text{-}C_3N_4/Bi_{24}O_{31}Cl_{10}$ ternary heterojunction photocatalysts to enhance the visible light photodegradation of antibiotics. This configuration significantly improves the efficiency of the photocatalytic process, especially under visible light irradiation.[299] Additionally, Shao et al. developed an innovative approach that integrates black phosphorus nanosheets into MXene. This modification enhances visible light photocatalytic activity by employing a modified diode junction mechanism. The strategic modification improves the generation and separation of charge carriers, resulting in enhanced photocatalytic performance.[53] The study investigated the complex interplay between metal oxide nanoparticles, graphene, MXene, and MoS_2. The results unveiled a prominent mechanism of direct charge transfer from metal oxide nanoparticles to graphene. In contrast, MXene composites strongly tended to form Schottky junctions, significantly impacting the composite structures' electronic and optical properties. Moreover, the present study emphasized the prevalence of heterojunction type II and Z-scheme mechanisms in MoS_2 composites, demonstrating the diverse and effective separation and utilization of charge carriers.

6. Conclusion and Perspective

Despite advancements in developing regular morphology metal oxides supported on 2D materials, the efficiency of these metal oxide composites is still not as effective as desired. The study underscores the importance of operational parameters in photocatalytic processes, focusing on the interaction between 2D materials and critical variables. It reveals that the nanoparticle composition is crucial in influencing performance metrics, especially within composite structures. A comprehensive analysis highlighted the benefits of hydrothermal synthesis as a method for precise control of reaction parameters. This technique ensures consistent size, crystallinity, and the desired morphology of metal oxides, enhancing photocatalytic efficiency in removing organic pollutants with 2D-metal oxide nanostructures. Additionally, this synthesis approach yields exceptionally pure products. Although it is time-consuming, lasting up to 24 h, it is relatively simple and offers superior reproducibility compared to alternative methods.

Efforts to improve efficiency in light-harvesting also face various challenges. Despite extensive research on 2D-metal oxide composites and light source optimization, significant advancements have not been achieved. The complex properties of these composites hinder the attainment of optimal configurations. Furthermore, limitations in light energy conversion and the restricted range of available light sources impede the overall performance of the system. To overcome these challenges, innovative strategies are necessary to expand the spectrum of light sources, thereby enabling efficiency improvements. Additionally, the development of high-capacity adsorbent materials with effective pollutant capture and degradation capabilities presents a promising solution to these obstacles.

Despite efforts to enhance the performance of 2D-metal oxide nanocomposites by combining multiple catalysts, most composites have not met the desired standards, indicating a need for further research and development. Exceptions are noted in Table 6, including successful configurations such as $BiOI/Fe_3O_4@GO$,[147] $AgNPs/TiO_2/Ti_3C_2T_x$,[128] $CoO@TiO_2/Ti_3C_2T_x$,[289] and $Bi_2S_3/MoS_2/TiO_2$.[183] In contrast, the superior efficiency of 2D-metal oxide nanoparticles in pollutant removal is likely due to their unique morphology, extensive surface area, heightened reactivity, and improved dispersion, enhancing their interaction and removal of organic pollutants. The graphene configuration has been proven to be superior as compared to alternatives. Incorporating graphene enhances photocatalytic efficiency by improving light absorption and dye degradation. The remarkable efficiency of the composites presented in Table 6 is likely due to the inclusion of titanium dioxide (TiO_2). TiO_2 nanoparticles offer key advantages such as a high surface area, stability, and, particularly, effectiveness in light capture. When integrated with graphene, MoS_2, and MXene, which enhances electrical conductivity and adds structural support, TiO_2 helps create a composite that significantly boosts the performance of light-harvesting systems.

The translation of laboratory research into practical applications is significantly impacted by the development of multifunctional materials. To achieve this, the development of high-performance materials and a comprehensive investigation of degradation mechanisms are essential. The adoption of tailored design strategies to enhance the effectiveness of metal oxide nanocomposites is crucial. However, there are notable challenges that must be overcome in this pursuit. Overcoming these obstacles is imperative for the successful implementation of environmental remediation techniques, emphasizing the significance of 2D material–metal oxide composites. These hybrid materials exhibit immense potential in addressing environmental concerns and advancing global sustainability.

Acknowledgements

This research was funded by the Science Committee of the Ministry of Science and Higher Education of the Republic of Kazakhstan (Grant No. AP19676347). This research was also funded by Nazarbayev University FD-CRDG (Grant No. 20122022FD4111).

Conflict of Interest

The authors declare no conflict of interest.

Keywords

graphene, metal oxide, MoS_2, MXene, organic pollutants, photocatalysis

Received: July 6, 2024
Revised: August 30, 2024
Published online: September 27, 2024

© 2024 The Author(s). Advanced Sustainable Systems published by Wiley-VCH GmbH

23667486, 2024, 12, Downloaded from https://advanced.onlinelibrary.wiley.com/doi/10.1002/adsu.202400483 by Nazarbayev University, Wiley Online Library on [08/07/2025]. See the Terms and Conditions (https://onlinelibrary.wiley.com/terms-and-conditions) on Wiley Online Library for rules of use; OA articles are governed by the applicable Creative Commons License

[1] M. Li, W. Liu, Z. Yin, H. Yang, Y. Chen, C. Yang, Y. Luo, Z. Hong, C. Xie, M. Xue, *Sens. Actuators, A* **2023**, *363*, 114750.
[2] Z. Yin, F. Yuan, M. Li, M. Xue, D. Zhou, Y. Chen, X. Liu, Y. Luo, Z. Hong, C. Xie, J. Ou, *Prog. Org. Coat.* **2021**, *157*, 106311.
[3] X. Chen, Z. Yin, Y. Deng, Z. Li, M. Xue, Y. Chen, Y. Xie, W. Liu, P. He, Y. Luo, Z. Hong, C. Xie, *Sens. Actuators, A* **2023**, *362*, 114630.
[4] Z. Yin, F. Yuan, M. Xue, Y. Xue, Y. Xie, J. Ou, Y. Luo, Z. Hong, C. Xie, *J. Colloid Interface Sci.* **2022**, *611*, 93.
[5] Z. Yin, X. Chen, T. Zhou, M. Xue, M. Li, K. Liu, D. Zhou, J. Ou, Y. Xie, Z. Ren, Y. Luo, Z. Hong, *Sep. Purif. Technol.* **2022**, *286*, 120504.
[6] Z. Li, Z. Yin, W. Xiao, Y. Chen, C. Yang, Y. Luo, Z. Hong, M. Xue, *Ind. Crops Prod.* **2024**, *209*, 118001.
[7] Z. Yin, Y. Cheng, Y. Deng, Z. Li, K. Liu, M. Li, X. Chen, M. Xue, J. Ou, S. Lei, Y. Luo, C. Xie, Z. Hong, *Surf. Coat. Technol.* **2022**, *445*, 128714.
[8] M. Li, W. Xiao, Z. Yin, Y. Chen, Y. Luo, Z. Hong, M. Xue, *Prog. Org. Coat.* **2024**, *186*, 108086.
[9] Z. Yin, Z. Li, Y. Deng, M. Xue, Y. Chen, J. Ou, Y. Xie, Y. Luo, C. Xie, Z. Hong, *Ind. Crops Prod.* **2023**, *197*, 116672.
[10] Z. Yin, M. Li, Z. Li, Y. Deng, M. Xue, Y. Chen, J. Ou, S. Lei, Y. Luo, C. Xie, *J. Environ. Manage.* **2023**, *342*, 118127.
[11] K. Anand, V. Murugan, S. Mohana Roopan, T. V. Surendra, A. A. Chuturgoon, S. Muniyasamy, *J. Inorg. Organomet. Polym. Mater.* **2018**, *28*, 2241.
[12] E. Brillas, C. A. Martínez-Huitle, *Appl. Catal., B* **2015**, *166–167*, 603.
[13] S. Zhang, M. Zeng, J. Li, J. Li, J. Xu, X. Wang, *J. Mater. Chem. A* **2014**, *2*, 4391.
[14] K. Liu, Z. Yin, R. Luo, B. Qiu, Y. Chen, C. Yang, Y. Luo, Z. Hong, M. Xue, *Ind. Crops Prod.* **2023**, *203*, 117190.
[15] B. Y. Balarabe, *Hybrid Adv.* **2023**, *4*, 100107.
[16] B. Y. Balarabe, S. Paria, D. S. Keita, A. Razak Ibrahim Baraze, E. Kalugendo, G. Nii Tetteh Tetteh, M. Merycleopha Meringo, M. Nasser Illiassou Oumarou, *Inorg. Chem. Commun.* **2022**, *146*, 110204.
[17] B. Y. Balarabe, P. Bomokayi, I. Adjama, A. Ayouba Mahamane, M. O. Daramola, S. A. Iwarere, *Nanotechnol. Environ. Eng.* **2024**, *9*, 239.
[18] E. Haritha, S. M. Roopan, G. Madhavi, G. Elango, N. A. Al-Dhabi, M. V. Arasu, *J. Clust. Sci.* **2017**, *28*, 1225.
[19] J. Wen, J. Xie, X. Chen, X. Li, *Appl. Surf. Sci.* **2017**, *391*, 72.
[20] M. Nasrollahzadeh, M. Sajjadi, S. Iravani, R. S. Varma, *J. Hazard. Mater.* **2021**, *401*, 123401.
[21] A. B. Djurišić, Y. He, A. M. C. Ng, *APL Mater.* **2020**, *8*, 030903.
[22] S. K. Loeb, P. J. J. Alvarez, J. A. Brame, E. L. Cates, W. Choi, J. Crittenden, D. D. Dionysiou, Q. Li, G. Li-Puma, X. Quan, D. L. Sedlak, T. D Waite, P. Westerhoff, J. H. Kim, *Environ. Sci. Technol.* **2019**, *53*, 2937.
[23] E. Haritha, S. M. Roopan, G. Madhavi, G. Elango, N. A. Al-Dhabi, M. V. Arasu, *J. Photochem. Photobiol., B* **2016**, *162*, 441.
[24] M. Pelaez, N. T. Nolan, S. C. Pillai, M. K. Seery, P. Falaras, A. G. Kontos, P. S. M. Dunlop, J. W. J. Hamilton, J. A. Byrne, K. O'Shea, M. H. Entezari, D. D. Dionysiou, *Appl. Catal., B* **2012**, *125*, 331.
[25] X. Hu, G. Li, J. C. Yu, *Langmuir* **2010**, *26*, 3031.
[26] B. Y. Balarabe, P. Maity, *J. Photochem. Photobiol., A* **2024**, *449*, 115405.
[27] B. Parasuraman, V. Vasudevan, B. Kandasamy, H. Rangaraju, P. Thangavelu, *Environ. Sci. Pollut. Res.* **2024**, *31*, 40245.
[28] A. Fujishima, K. Honda, *Nature* **1972**, *238*, 37.
[29] Y. Deng, H. Chen, G. Wang, Z. Yin, Z. Li, Y. Chen, C. Yang, Y. Luo, C. Xie, M. Xue, *Colloids Surf., A* **2024**, *696*, 134375.
[30] X. Chen, Z. Yin, J. Yan, M. Xue, Y. Chen, C. Yang, Y. Luo, *Surf. Coat. Technol.* **2023**, *467*, 129701.
[31] Z. Yin, F. Yuan, D. Zhou, M. Xue, Y. Luo, Z. Hong, C. Xie, *Chem. Phys. Lett.* **2021**, *771*, 138558.
[32] Y. Deng, Z. Li, Z. Yin, Y. Chen, C. Yang, Y. Luo, M. Xue, *Ind. Crops Prod.* **2024**, *216*, 118732.
[33] Z. Yin, M. Xue, Y. Luo, Z. Hong, C. Xie, Z. Ren, H. Wang, *Chem. Phys. Lett.* **2020**, *755*, 137806.
[34] B. Y. Balarabe, I. Adjama, M. W. Abdoulrazak, H. Moussa, A. B. I. Awali, M. N. Illiassou Oumarou, *NanoEra* **2024**, *3*, 61.
[35] B. Y. Balarabe, A. Irédon, M. Hassimi, M. N. Illiassou Oumarou, V. Masiyambiri, T. J. Gunda, *Hybrid Adv.* **2023**, *4*, 100114.
[36] A. Sarkar, S. Sharma, B. Y. Balarabe, S. Vadivel, T. Tyagi, D. Das, S. Kumar, A. Puzari, B. Paul, *Int. J. Hydrogen Energy* **2024**, *59*, 1174.
[37] A. Molkenova, S. Sarsenov, S. Atabaev, L. Khamkhash, T. S. Atabaev, *Environ. Nanotechnol., Monit. Manage.* **2021**, *16*, 100507.
[38] T. S. Atabaev, *J. Adv. Ceram.* **2015**, *4*, 61.
[39] K. Rustembekkyzy, M. Sabyr, Y. N. Kanafin, L. Khamkhash, T. S. Atabaev, *RSC Adv.* **2024**, *14*, 16293.
[40] S. Mergenbayeva, T. S. Atabaev, J. Vakros, D. Mantzavinos, S. G. Poulopoulos, *Catalysts* **2022**, *12*, 1523.
[41] A. Zaleska, *Recent Pat. Eng.* **2008**, *2*, 157.
[42] X. Zhang, X. Liu, S. Dong, J. Yang, Y. Liu, *Appl. Mater. Today* **2019**, *16*, 315.
[43] P. Zhang, Q. Ru, H. Yan, X. Hou, F. Chen, S. Hu, L. Zhao, *J. Mater. Sci. Technol.* **2019**, *35*, 1840.
[44] F. He, A. Meng, B. Cheng, W. Ho, J. Yu, *Chin. J. Catal.* **2020**, *41*, 9.
[45] Q. Yan, G. F. Huang, D. F. Li, M. Zhang, A. L. Pan, W. Q. Huang, *J. Mater. Sci. Technol.* **2018**, *34*, 2515.
[46] N. Zhang, X. Jiang, J. Fan, W. Luo, Y. Xiang, W. Wu, M. Ren, X. Zhang, W. Cai, J. Xu, *Nanotechnology* **2019**, *30*, 505201.
[47] B. Y. Balarabe, P. Maity, A. C. S. C. Teixeira, S. A. Iwarere, *Inorg. Chem. Commun.* **2023**, *158*, 111560.
[48] M. Chhowalla, H. S. Shin, G. Eda, L. J. Li, K. P. Loh, H. Zhang, *Nat. Chem.* **2013**, *5*, 263.
[49] P. Song, J. Du, X. Ma, Y. Shi, X. Fang, D. Liu, S. Wei, Z. Liu, Y. Cao, B. Lin, J. Di, Y. Wang, J. Cui, T. Kong, C. Gao, Y. Xiong, *EcoEnergy* **2023**, *1*, 197.
[50] H. Wang, C. Cao, D. Li, Y. Ge, R. Chen, R. Song, W. Gao, X. Wang, X. Deng, H. Zhang, B. Ye, Z. Li, C. Li, *J. Am. Chem. Soc.* **2023**, *145*, 16852.
[51] P. Song, J. Du, Y. Shi, X. Fang, X. Ma, D. Liu, D. Cao, J. Li, R. Chen, C. Wu, J. Cui, Y. Wang, J. Di, J. Low, T. Kong, R. Long, H. Zhang, Y. Xiong, *ACS Mater. Lett.* **2024**, *6*, 427.
[52] P. Song, X. Fang, W. Jiang, Y. Cao, D. Liu, S. Wei, J. Du, L. Sun, L. Zhao, S. Liu, Y. Zhou, J. Di, C. Lv, B. Tang, J. Yang, T. Kong, Y. Xiong, *Trans. Tianjin Univ.* **2024**, *30*, 211.
[53] B. Shao, J. Wang, Z. Liu, G. Zeng, L. Tang, Q. Liang, Q. He, T. Wu, Y. Liu, X. Yuan, *J. Mater. Chem. A* **2020**, *8*, 5171.
[54] D. H. Keum, S. Cho, J. H. Kim, D. H. Choe, H. J. Sung, M. Kan, H. Kang, J. Y. Hwang, S. W. Kim, H. Yang, K. J. Chang, Y. H. Lee, *J. Phys. Chem. Lett.* **2015**, *11*, 482.
[55] Y. Xu, M. A. A. Schoonen, *Am. Mineral.* **2000**, *85*, 543.
[56] Y. Liu, Y. Li, F. Peng, Y. Lin, S. Yang, S. Zhang, H. Wang, Y. Cao, H. Yu, *Appl. Catal., B* **2019**, *241*, 236.
[57] L. Cheng, X. Li, H. Zhang, Q. Xiang, *ACS J. Phys. Chem. Lett.* **2019**, *10*, 3488.
[58] H. Fang, Y. Pan, M. Yin, C. Pan, *Mater. Res. Bull.* **2020**, *121*, 110618.
[59] F. Xu, D. Zhang, Y. Liao, G. Wang, X. Shi, H. Zhang, Q. Xiang, *J. Am. Ceram. Soc.* **2020**, *103*, 849.
[60] H. Zhang, M. Li, J. Cao, Q. Tang, P. Kang, C. Zhu, M. Ma, *Ceram. Int.* **2018**, *44*, 19958.
[61] H. Wang, L. Chen, Y. Sun, J. Yu, Y. Zhao, X. Zhan, H. Shi, *Sep. Purif. Technol.* **2021**, *265*, 118516.
[62] H. Liu, C. Yang, X. Jin, J. Zhong, J. Li, *Colloids Surf., A* **2020**, *603*, 125239.
[63] A. K. Geim, *Science* **2009**, *324*, 1530.
[64] F. Zou, X. Hu, L. Qie, Y. Jiang, X. Xiong, Y. Qiao, Y. Huang, *Nanoscale* **2014**, *6*, 924.
[65] H. Wang, L. F. Cui, Y. Yang, H. Sanchez Casalongue, J. T. Robinson, Y. Liang, Y. Cui, H. Dai, *J. Am. Chem. Soc.* **2010**, *132*, 13978.

© 2024 The Author(s). Advanced Sustainable Systems published by Wiley-VCH GmbH

23667486, 2024, 12, Downloaded from https://advanced.onlinelibrary.wiley.com/doi/10.1002/adsu.202400483 by Nazarbayev University, Wiley Online Library on [08/07/2025]. See the Terms and Conditions (https://onlinelibrary.wiley.com/terms-and-conditions) on Wiley Online Library for rules of use; OA articles are governed by the applicable Creative Commons License

[66] S. Stankovich, D. A. Dikin, G. H. B. Dommett, K. M. Kohlhaas, E. J. Zimney, E. A. Stach, R. D. Piner, S. B. T. Nguyen, R. S. Ruoff, *Nature* **2006**, *442*, 282.
[67] H. Li, G. Zhao, H. Zhang, *Materials* **2023**, *16*, 3783.
[68] A. Kommu, J. K. Singh, *Soft Mater* **2020**, *18*, 297.
[69] S. Chowdhury, R. Balasubramanian, *Adv. Colloid Interface Sci.* **2014**, *204*, 35
[70] J. D. Renteria, S. Ramirez, H. Malekpour, B. Alonso, A. Centeno, A. Zurutuza, A. I. Cocemasov, D. L. Nika, A. A. Balandin, *Adv. Funct. Mater.* **2015**, *25*, 4664.
[71] P. Majumder, R. Gangopadhyay, *RSC Adv.* **2022**, *12*, 5686.
[72] R. K. Upadhyay, N. Soin, S. S. Roy, *RSC Adv.* **2014**, *4*, 3823.
[73] H. Wang, X. Mi, Y. Li, S. Zhan, *Adv. Mater.* **2020**, *32*, 1806843.
[74] M. Hammad, P. Fortugno, S. Hardt, C. Kim, S. Salamon, T. C. Schmidt, H. Wende, C. Schulz, H. Wiggers, *Environ. Technol. Innovation* **2021**, *21*, 101239.
[75] C. N. R. Rao, A. K. Sood, K. S. Subrahmanyam, A. Govindaraj, *Angew. Chem., Int. Ed.* **2009**, *48*, 7752.
[76] Y. Zhu, S. Murali, W. Cai, X. Li, J. W. Suk, J. R. Potts, R. S. Ruoff, *Adv. Mater.* **2010**, *22*, 3906.
[77] L. Luo, X. Gu, J. Wu, S. Zhong, J. Chen, *Adv. Mater. Res.* **2012**, *550–553*, 2121.
[78] X. Zhan, C. Si, J. Zhou, Z. Sun, *Nanoscale Horiz.* **2020**, *5*, 235.
[79] Y. Li, L. Ding, Z. Liang, Y. Xue, H. Cui, J. Tian, *Chem. Eng. J.* **2020**, *383*, 123178.
[80] B. Anasori, M. R. Lukatskaya, Y. Gogotsi, *Eng. Technol.* **2017**, *2*, 46.
[81] J. Peng, X. Chen, W. J. Ong, X. Zhao, N. Li, *Chem.* **2019**, *5*, 18.
[82] H. Zou, B. He, P. Kuang, J. Yu, K. Fan, *ACS Appl. Mater. Interfaces* **2018**, *10*, 22311.
[83] J. Pang, R. G. Mendes, A. Bachmatiuk, L. Zhao, H. Q. Ta, T. Gemming, H. Liu, Z. Liu, M. H. Rummeli, *Chem. Soc. Rev.* **2019**, *48*, 72.
[84] Z. Li, Y. Wu, *Small* **2019**, *15*, 1804736.
[85] Z. Guan, X. Wang, T. Li, Q. Zhu, M. Jia, B. Xu, *J. Mater. Sci. Technol.* **2019**, *35*, 1977.
[86] H. Wang, R. Zhao, J. Qin, H. Hu, X. Fan, X. Cao, D. Wang, *ACS Appl. Mater. Interfaces* **2019**, *11*, 44249.
[87] Z. Zeng, Y. Yan, J. Chen, P. Zan, Q. Tian, P. Chen, *Adv. Funct. Mater.* **2019**, *29*, 1806500.
[88] Y. Zhuang, Y. Liu, X. Meng, *Appl. Surf. Sci.* **2019**, *496*, 143647.
[89] X. Cheng, L. Zu, Y. Jiang, D. Shi, X. Cai, Y. Ni, S. Lin, Y. Qin, *Chem. Commun.* **2018**, *54*, 11622.
[90] P. Kuang, J. Low, B. Cheng, J. Yu, J. Fan, *J. Mater. Sci. Technol.* **2020**, *56*, 18.
[91] A. D. Handoko, S. N. Steinmann, Z. W. Seh, *Nanoscale Horiz.* **2019**, *4*, 809.
[92] X. An, W. Wang, J. Wang, H. Duan, J. Shi, X. Yu, *Phys. Chem. Chem. Phys.* **2018**, *20*, 11405.
[93] M. Sokol, V. Natu, S. Kota, M. W. Barsoum, *Trends Chem.* **2019**, *1*, 210.
[94] X. Wang, X. Shen, Y. Gao, Z. Wang, R. Yu, L. Chen, *J. Am. Chem. Soc.* **2015**, *137*, 2715.
[95] Y. Li, H. Shao, Z. Lin, J. Lu, L. Liu, B. Duployer, P. O. Å. Persson, P. Eklund, L. Hultman, M. Li, K. Chen, X. H. Zha, S. Du, P. Rozier, Z. Chai, E. Raymundo-Piñero, P. L. Taberna, P. Simon, Q. Huang, *Nat. Mater.* **2020**, *19*, 894.
[96] I. Persson, L. Å. Näslund, J. Halim, M. W. Barsoum, V. Darakchieva, J. Palisaitis, J. Rosen, P. O. Å. Persson, *2D Mater.* **2018**, *5*, 015002.
[97] M. A. Hope, A. C. Forse, K. J. Griffith, M. R. Lukatskaya, M. Ghidiu, Y. Gogotsi, C. P. Grey, *Phys. Chem. Chem. Phys.* **2016**, *18*, 5099.
[98] V. Kamysbayev, A. S. Filatov, H. Hu, X. Rui, F. Lagunas, D. Wang, R. F. Klie, D. V Talapin, *Science* **2020**, *369*, 979.
[99] M. Khazaei, A. Ranjbar, K. Esfarjani, D. Bogdanovski, R. Dronskowski, S. Yunoki, *Phys. Chem. Chem. Phys.* **2018**, *20*, 8579.
[100] M. Naguib, M. Kurtoglu, V. Presser, J. Lu, J. Niu, M. Heon, L. Hultman, Y. Gogotsi, M. W. Barsoum, *Adv. Mater.* **2011**, *23*, 4248.
[101] W. Hong, B. C. Wyatt, S. K. Nemani, B. Anasori, *MRS Bull.* **2020**, *45*, 850.
[102] L. Britnell, R. M. Ribeiro, A. Eckmann, R. Jalil, B. D. Belle, A. Mishchenko, Y.-J. Kim, R. V Gorbachev, T. Georgiou, S. V Morozov, A. N. Grigorenko, A. K. Geim, C. Casiraghi, A. H. Castro Neto, K. S. Novoselov, *Science* **2013**, *340*, 1311.
[103] R. Zan, Q. M. Ramasse, R. Jalil, T. Georgiou, U. Bangert, K. S. Novoselov, *ACS Nano* **2013**, *7*, 10167.
[104] A. Molina-Sánchez, K. Hummer, L. Wirtz, *Surf. Sci. Rep.* **2015**, *70*, 554.
[105] Q. H. Wang, K. Kalantar-Zadeh, A. Kis, J. N. Coleman, M. S. Strano, *Nat. Nanotechnol.* **2012**, *7*, 699.
[106] H. Zeng, J. Dai, W. Yao, D. Xiao, X. Cui, *Nat. Nanotechnol.* **2012**, *7*, 490.
[107] M. Mortazavi, C. Wang, J. Deng, V. B. Shenoy, N. V. Medhekar, *J. Power Sources* **2014**, *268*, 279.
[108] W. Bao, X. Cai, D. Kim, K. Sridhara, M. S. Fuhrer, *Appl. Phys. Lett.* **2013**, *102*, 042104.
[109] J. N. Coleman, M. Lotya, A. O'neill, S. D. Bergin, P. J. King, U. Khan, K. Young, A. Gaucher, S. De, R. J. Smith, I. V. Shvets, S. K. Arora, G. Stanton, H.-Y. Kim, K. Lee, G. T. Kim, G. S. Duesberg, T. Hallam, J. J. Boland, J. J. Wang, J. F. Donegan, J. C. Grunlan, G. Moriarty, A. Shmeliov, R. J. Nicholls, J. M. Perkins, E. M. Grieveson, K. Theuwissen, D. W. Mccomb, P. D. Nellist, et al., *Science* **2011**, *331*, 568.
[110] A. Jawaid, D. Nepal, K. Park, M. Jespersen, A. Qualley, P. Mirau, L. F. Drummy, R. A. Vaia, *Chem. Mater.* **2016**, *28*, 337.
[111] D. Dumcenco, D. Ovchinnikov, K. Marinov, P. Lazić, M. Gibertini, N. Marzari, O. L. Sanchez, Y. C. Kung, D. Krasnozhon, M. W. Chen, S. Bertolazzi, P. Gillet, A. Fontcuberta I Morral, A. Radenovic, A. Kis, *ACS Nano* **2015**, *9*, 4611.
[112] Y. Zhan, Z. Liu, S. Najmaei, P. M. Ajayan, J. Lou, *Small* **2012**, *8*, 966.
[113] Y. Shi, W. Zhou, A. Y. Lu, W. Fang, Y. H. Lee, A. L. Hsu, S. M. Kim, K. K. Kim, H. Y. Yang, L. J. Li, J. C. Idrobo, J. Kong, *Nano Lett.* **2012**, *12*, 2784.
[114] Y. C. Lin, W. Zhang, J. K. Huang, K. K. Liu, Y. H. Lee, C. Te Liang, C. W. Chu, L. J. Li, *Nanoscale* **2012**, *4*, 6637.
[115] A. Behera, D. Kandi, S. Martha, K. Parida, *Inorg. Chem.* **2019**, *58*, 16592.
[116] L. Shi, T. Wang, H. Zhang, K. Chang, X. Meng, H. Liu, J. Ye, *Adv. Sci.* **2015**, *2*, 1500006.
[117] K. M. Garadkar, A. A. Patil, P. P. Hankare, P. A. Chate, D. J. Sathe, S. D. Delekar, *J. Alloys Compd.* **2009**, *487*, 786.
[118] W. Zhou, Z. Yin, Y. Du, X. Huang, Z. Zeng, Z. Fan, H. Liu, J. Wang, H. Zhang, *Small* **2013**, *9*, 140.
[119] X. Feng, Q. Tang, J. Zhou, J. Fang, P. Ding, L. Sun, L. Shi, *Cryst. Res. Technol.* **2013**, *48*, 363.
[120] S. Mohana Roopan, M. A. Khan, *Catal. Rev.: Sci. Eng.* **2023**, *65*, 620.
[121] S. Gulati, M. Sachdeva, K. K. Bhasin, *AIP Conf. Proc.* **2018**, *1953*, 030215.
[122] Z. Sun, T. Liao, L. Kou, *Sci. China Mater.* **2017**, *60*, 1.
[123] R. Shahbazi, A. Payan, M. Fattahi, *J. Photochem. Photobiol., A* **2018**, *364*, 564.
[124] R. Selvaraj, K. R. Kalimuthu, V. Kalimuthu, *Mater. Lett.* **2019**, *243*, 183.
[125] Y. Fang, Y. Cao, Q. Chen, *Ceram. Int.* **2019**, *45*, 22298.
[126] P. Ribao, M. J. Rivero, I. Ortiz, *Environ. Sci. Pollut. Res.* **2017**, *24*, 12628.

© 2024 The Author(s). Advanced Sustainable Systems published by Wiley-VCH GmbH

23667486, 2024, 12, Downloaded from https://advanced.onlinelibrary.wiley.com/doi/10.1002/adsu.202400483 by Nazarbayev University, Wiley Online Library on [08/07/2025]. See the Terms and Conditions (https://onlinelibrary.wiley.com/terms-and-conditions) on Wiley Online Library for rules of use; OA articles are governed by the applicable Creative Commons License

[127] G. Malekshoar, K. Pal, Q. He, A. Yu, A. K. Ray, *Ind. Eng. Chem. Res.* **2014**, *53*, 18824.
[128] Z. Othman, A. Sinopoli, H. R. MacKey, K. A. Mahmoud, *ACS Omega* **2021**, *6*, 33325.
[129] I. Amalraj Appavoo, J. Hu, Y. Huang, S. F. Y. Li, S. L. Ong, *Water Res.* **2014**, *57*, 270.
[130] E. Rafiee, E. Noori, A. A. Zinatizadeh, H. Zanganeh, *RSC Adv.* **2016**, *6*, 96554.
[131] L. jun Luo, J. Li, J. Dai, L. Xia, C. J. Barrow, H. Wang, J. Jegatheesan, M. Yang, *Process Saf. Environ. Prot.* **2017**, *112*, 274.
[132] G. Y. He, J. Huang, W. F. Liu, X. Wang, H. Q. Chen, X. Q. Sun, *Mater. Technol.* **2012**, *27*, 278.
[133] C. Liu, M. Yue, L. Liu, Y. Rui, W. Cui, *RSC Adv.* **2018**, *8*, 22402.
[134] H. Fan, X. Zhao, J. Yang, X. Shan, L. Yang, Y. Zhang, X. Li, M. Gao, *Catal. Commun.* **2012**, *29*, 29.
[135] T. Xu, L. Zhang, H. Cheng, Y. Zhu, *Appl. Catal., B* **2011**, *101*, 382.
[136] K. K. Abbas, A. M. H. Abdulkadhimal-Ghaban, E. H. Rdewi, *J. Environ. Chem. Eng.* **2022**, *10*, 108111.
[137] Y. H. Tan, K. Yu, J. Z. Li, H. Fu, Z. Q. Zhu, *J. Appl. Phys.* **2014**, *116*, 064305.
[138] S. Kumar, V. Maivizhikannan, J. Drews, V. Krishnan, *Vacuum* **2019**, *163*, 88.
[139] Y. Fu, H. Chen, X. Sun, X. Wang, *Appl. Catal., B* **2012**, *111–112*, 280.
[140] Y. Zeng, N. Guo, Y. Song, Y. Zhao, H. Li, X. Xu, J. Qiu, H. Yu, *J. Colloid Interface Sci.* **2018**, *514*, 664.
[141] T. Cai, L. Wang, Y. Liu, S. Zhang, W. Dong, H. Chen, X. Yi, J. Yuan, X. Xia, C. Liu, S. Luo, *Appl. Catal., B* **2018**, *239*, 545.
[142] P. Wang, P. Shi, Y. Hong, X. Zhou, W. Yao, *Mater. Res. Bull.* **2015**, *62*, 24.
[143] C. Mu, Y. Zhang, W. Cui, Y. Liang, Y. Zhu, *Appl. Catal., B* **2017**, *212*, 41.
[144] M. Al Kausor, D. Chakrabortty, *J. Nanopart. Res.* **2020**, *22*, 93.
[145] P. Dong, Y. Wang, B. Cao, S. Xin, L. Guo, J. Zhang, F. Li, *Appl. Catal., B* **2013**, *132–133*, 45.
[146] Y. Tang, L. Dong, S. Mao, H. Gu, T. Malkoske, B. Chen, *ACS Appl. Energy Mater.* **2018**, *1*, 2698.
[147] P. Singh, A. Sudhaik, P. Raizada, P. Shandilya, R. Sharma, A. Hosseini-Bandegharaei, *Mater. Today Chem.* **2019**, *12*, 85.
[148] H. Lai, G. Ma, W. Shang, D. Chen, Y. Yun, X. Peng, F. Xu, *Chemosphere* **2019**, *223*, 465.
[149] J. Kaur, M. Kaur, *Ceram. Int.* **2019**, *45*, 8646.
[150] S. Samakchi, N. Chaibakhsh, Z. Moradi-Shoeili, *J. Photochem. Photobiol., A* **2018**, *367*, 420.
[151] S. Chakrabarty, A. Mukherjee, S. Basu, *ACS Sustainable Chem. Eng.* **2018**, *6*, 5238.
[152] S. V. Prabhakar Vattikuti, C. Byon, C. V. Reddy, *Electron. Mater. Lett.* **2016**, *12*, 812.
[153] T. Zhu, L. Huang, Y. Song, Z. Chen, H. Ji, Y. Li, Y. Xu, Q. Zhang, H. Xu, H. Li, *New J. Chem.* **2016**, *40*, 2168.
[154] J. Di, J. Xia, Y. Ge, L. Xu, H. Xu, J. Chen, M. He, H. Li, *Dalton Trans.* **2014**, *43*, 15429.
[155] Q. Huang, Y. Liu, T. Cai, X. Xia, *J. Photochem. Photobiol., A* **2019**, *375*, 201.
[156] T. Rasheed, A. Rasheed, S. Munir, S. Ajmal, Z. M Shahzad, I. A. Alsafari, S. A. Ragab, P. O. Agboola, I. Shakir, *Adv. Powder Technol.* **2021**, *32*, 2248.
[157] I. A. Alsafari, *Ceram. Int.* **2022**, *48*, 10960.
[158] M. M. Sajid, S. B. Khan, Y. Javed, N. Amin, Z. Zhang, N. A. Shad, H. Zhai, *Environ. Sci. Pollut. Res.* **2021**, *28*, 35911.
[159] M. E. Khan, M. M. Khan, M. H. Cho, *Sci. Rep.* **2017**, *7*, 5928.
[160] L. Chen, S. Yang, L. Mu, P. C. Ma, *J. Colloid Interface Sci.* **2018**, *512*, 647.
[161] X. Yu, Z. Li, K. Dang, Z. Zhang, L. Gao, L. Duan, Z. Jiang, J. Fan, P. Zhao, *J. Mater. Sci.: Mater. Electron.* **2018**, *29*, 8729.
[162] C. Cui, R. Guo, H. Xiao, E. Ren, Q. Song, C. Xiang, X. Lai, J. Lan, S. Jiang, *Appl. Surf. Sci.* **2020**, *505*, 144595.
[163] Y. Li, Z. Tang, J. Zhang, Z. Zhang, *Appl. Catal., A* **2016**, *522*, 90.
[164] E. B. Simsek, B. Kilic, M. Asgin, A. Akan, *J. Ind. Eng. Chem.* **2018**, *59*, 115.
[165] A. Ghalajkhani, M. Haghighi, M. Shabani, *J. Photochem. Photobiol., A* **2018**, *359*, 145.
[166] D. Mu, Z. Chen, H. Shi, N. Tan, *RSC Adv.* **2018**, *8*, 36625.
[167] N. Raghavan, S. Thangavel, G. Venugopal, *Mater. Sci. Semicond. Process.* **2015**, *30*, 321.
[168] Y. Tang, Z. Zheng, X. Sun, X. Li, L. Li, *Chem. Eng. J.* **2019**, *368*, 448.
[169] P. Ghasemipour, M. Fattahi, B. Rasekh, F. Yazdian, *Sci. Rep.* **2020**, *10*, 4414.
[170] J. Liu, L. Liu, H. Bai, Y. Wang, D. D. Sun, *Appl. Catal., B* **2011**, *106*, 76.
[171] Z. Shi, P. Xu, X. Shen, Y. Zhang, L. Luo, G. Duoerkun, L. Zhang, *Mater. Res. Bull.* **2019**, *112*, 354.
[172] V. Shanmugam, K. S. Jeyaperumal, P. Mariappan, A. L. Muppudathi, *New J. Chem.* **2020**, *44*, 13182.
[173] X. Liu, L. Pan, T. Lv, Z. Sun, C. Q. Sun, *J. Colloid Interface Sci.* **2013**, *408*, 145.
[174] S. Jia, M. Xu, S. Chen, J. Yan, J. Yun, Z. Deng, Z. Zhang, W. Zhao, Y. Wang, X. Ma, *Mater. Lett.* **2019**, *236*, 697.
[175] W. Zhou, J. Zhu, F. Wang, M. Cao, T. Zhao, *Mater. Lett.* **2017**, *206*, 237.
[176] C. Cui, R. Guo, E. Ren, H. Xiao, X. Lai, Q. Qin, S. Jiang, H. Shen, M. Zhou, W. Qin, *Environ. Res.* **2021**, *193*, 110587.
[177] D. Zu, H. Song, Y. Wang, Z. Chao, Z. Li, G. Wang, Y. Shen, C. Li, J. Ma, *Appl. Catal., B* **2020**, *277*, 119140.
[178] M. E. Khan, M. M. Khan, M. H. Cho, *RSC Adv.* **2016**, *6*, 20824.
[179] A. Z. Warsi, F. Aziz, S. Zulfiqar, S. Haider, I. Shakir, P. O. Agboola, *Nanomaterials* **2022**, *12*, 713.
[180] M. F. Khadidja, J. Fan, S. Li, S. Li, K. Cui, J. Wu, W. Zeng, H. Wei, H. G. Jin, N. Naik, Z. Chao, D. Pan, Z. Guo, *Colloids Surf., A* **2021**, *628*, 127230.
[181] J. Pan, C. Chi, M. You, Z. Jiang, W. Zhao, M. Zhu, C. Song, Y. Zheng, C. Li, *Mater. Lett.* **2018**, *227*, 205.
[182] H. Feng, N. Tang, S. Zhang, B. Liu, Q. Cai, *J. Colloid Interface Sci.* **2017**, *486*, 58.
[183] Q. A. Drmosh, A. Hezam, A. H. Y. Hendi, M. Qamar, Z. H. Yamani, K. Byrappa, *Appl. Surf. Sci.* **2020**, *499*, 143938.
[184] H. Feng, W. Zhou, X. Zhang, S. Zhang, B. Liu, D. Zhen, *Adv. Compos. Lett.* **2019**, *28*, 1.
[185] Y. C. Pu, H. Y. Chou, W. S. Kuo, K. H. Wei, Y. J. Hsu, *Appl. Catal., B* **2017**, *204*, 21.
[186] J. Shen, J. Shen, W. Zhang, X. Yu, H. Tang, M. Zhang, Zulfiqar, Q. Liu, *Ceram. Int.* **2019**, *45*, 24146.
[187] S. Luo, R. Wang, J. Yin, T. Jiao, K. Chen, G. Zou, L. Zhang, J. Zhou, L. Zhang, Q. Peng, *ACS Omega* **2019**, *4*, 3946.
[188] C. Peng, X. Yang, Y. Li, H. Yu, H. Wang, F. Peng, *ACS Appl. Mater. Interfaces* **2016**, *8*, 6051.
[189] A. Beyhaqi, Q. Zeng, S. Chang, M. Wang, S. M. Taghi Azimi, C. Hu, *Chemosphere* **2020**, *247*, 125784.
[190] M. Irandost, R. Akbarzadeh, M. Pirsaheb, A. Asadi, P. Mohammadi, M. Sillanpää, *J. Mol. Liq.* **2019**, *291*, 111342.
[191] Y. Chen, F. Sun, Z. Huang, H. Chen, Z. Zhuang, Z. Pan, J. Long, F. Gu, *Appl. Catal., B* **2017**, *215*, 8.
[192] L. Zhang, L. Tan, Z. Yuan, B. Xu, W. Chen, Y. Tang, L. Li, J. Wang, *Chem. Eng. J.* **2023**, *452*, 139327.
[193] T. Naz, A. Rasheed, S. Ajmal, N. Sarwar, T. Rasheed, M. M. Baig, M. S. Zafar, D. J. Kang, G. Dastgeer, *Ceram. Int.* **2021**, *47*, 33454.
[194] T. Xu, J. Wang, Y. Cong, S. Jiang, Q. Zhang, H. Zhu, Y. Li, X. Li, *Chin. Chem. Lett.* **2020**, *31*, 1022.
[195] L. Chen, F. He, N. Zhao, R. Guo, *Appl. Surf. Sci.* **2017**, *420*, 669.

© 2024 The Author(s). Advanced Sustainable Systems published by Wiley-VCH GmbH

23667486, 2024, 12, Downloaded from https://advanced.onlinelibrary.wiley.com/doi/10.1002/adsu.202400483 by Nazarbayev University, Wiley Online Library on [08/07/2025]. See the Terms and Conditions (https://onlinelibrary.wiley.com/terms-and-conditions) on Wiley Online Library for rules of use; OA articles are governed by the applicable Creative Commons License

[196] J. Ke, J. Liu, H. Sun, H. Zhang, X. Duan, P. Liang, X. Li, M. O. Tade, S. Liu, S. Wang, *Appl. Catal., B* **2017**, *200*, 47.
[197] H. Liu, W. R. Cao, Y. Su, Z. Chen, Y. Wang, *J. Colloid Interface Sci.* **2013**, *398*, 161.
[198] L. Sun, Y. Wang, F. Raziq, Y. Qu, L. Bai, L. Jing, *Sci. Rep.* **2017**, *7*, 1303.
[199] Q. Wang, G. Yun, Y. Bai, N. An, J. Lian, H. Huang, B. Su, *Appl. Surf. Sci.* **2014**, *313*, 537.
[200] J. Wan, Y. Zhang, R. Wang, L. Liu, E. Liu, J. Fan, F. Fu, *J. Hazard. Mater.* **2020**, *384*, 121484.
[201] H. N. T. Phung, N. D. Truong, P. A. Duong, L. V. Tuan Hung, *Curr. Appl. Phys.* **2018**, *18*, 737.
[202] I. Tismanar, A. C. Obreja, O. Buiu, A. Duta, *Appl. Surf. Sci.* **2021**, *538*, 147833.
[203] M. O. Ansari, R. Kumar, M. S. Abdel-wahab, M. Abu Taleb, M. A. Barakat, *J. Taiwan Inst. Chem. Eng.* **2021**, *129*, 370.
[204] J. Sun, M. U. Farid, M. W. Boey, Y. Sato, G. Chen, A. K. An, *Chem. Eng. J.* **2023**, *468*, 143744.
[205] D. Fu, L. Zhang, R. Xie, H. Xu, Y. Zhong, X. Sui, Z. Mao, *J. Photochem. Photobiol., A* **2016**, *329*, 18.
[206] Y. Fu, X. Sun, X. Wanga, *Mater. Chem. Phys.* **2011**, *131*, 325.
[207] C. Peng, H. Wang, H. Yu, F. Peng, *Mater. Res. Bull.* **2017**, *89*, 16.
[208] M. Guo, Z. Xing, T. Zhao, Y. Qiu, B. Tao, Z. Li, W. Zhou, *Appl. Catal., B* **2020**, *272*, 118978.
[209] H. Zheng, X. Meng, J. Chen, M. Que, W. Wang, X. Liu, L. Yang, Y. Zhao, *Appl. Surf. Sci.* **2021**, *545*, 149031.
[210] I. A. Alsafari, S. Munir, S. Zulfiqar, M. S. Saif, M. F. Warsi, M. Shahid, *Ceram. Int.* **2021**, *47*, 28874.
[211] Q. T. H. Ta, N. M. Tran, J. S. Noh, *Catalysts* **2020**, *10*, 1140.
[212] A. Grzegórska, P. Głuchowski, J. Karczewski, J. Ryl, I. Wysocka, K. Siuzdak, G. Trykowski, K. Grochowska, A. Zielińska-Jurek, *Chem. Eng. J.* **2021**, *426*, 130801.
[213] H. Zhang, M. Li, C. Zhu, Q. Tang, P. Kang, J. Cao, *Ceram. Int.* **2020**, *46*, 81.
[214] N. Guo, H. Li, X. Xu, H. Yu, *Appl. Surf. Sci.* **2016**, *389*, 227.
[215] T. Zhao, Z. Xing, Z. Xiu, Z. Li, P. Chen, Q. Zhu, W. Zhou, *J. Hazard. Mater.* **2019**, *364*, 117.
[216] Y. Yu, L. Yan, J. Cheng, C. Jing, *Chem. Eng. J.* **2017**, *325*, 647.
[217] H. Li, K. Yu, X. Lei, B. Guo, C. Li, H. Fu, Z. Zhu, *Dalton Trans.* **2015**, *44*, 10438.
[218] X. Zhang, C. Shao, X. Li, F. Miao, K. Wang, N. Lu, Y. Liu, *J. Alloys Compd.* **2016**, *686*, 137.
[219] Y. Li, Z. Wang, H. Zhao, X. Huang, M. Yang, *J. Colloid Interface Sci.* **2019**, *557*, 709.
[220] A. Kumar, V. Navakoteswara Rao, A. Kumar, M. Venkatakrishnan Shankar, V. Krishnan, *ChemPhotoChem* **2020**, *4*, 427.
[221] K. Vikrant, C. M. Park, K. H. Kim, S. Kumar, E. C. Jeon, *J. Photochem. Photobiol., C* **2019**, *41*, 100316.
[222] N. Raza, W. Raza, H. Gul, M. Azam, J. Lee, K. Vikrant, K. H. Kim, *J. Clean. Prod.* **2020**, *254*, 120031.
[223] H. Anwer, A. Mahmood, J. Lee, K. H. Kim, J. W. Park, A. C. K. Yip, *Nano Res.* **2019**, *12*, 955.
[224] A. Bathla, S. A. Younis, K. H. Kim, X. Li, *Mater. Horiz.* **2023**, *10*, 1559.
[225] S. Dharwadkar, Y. Achari, *ENV44-1 CSCE Annual Conf., Laval (Greater Montreal)*, Canadian Society for Civil Engineering, Quebec **2019**.
[226] K. Ramesh, B. Gnanavel, M. Shkir, *Diam. Relat. Mater.* **2021**, *118*, 108514.
[227] N. S. Alim, H. O. Lintang, L. Yuliati, *IOP Conf. Ser.: Mater. Sci. Eng.* **2016**, *107*, 012001.
[228] M. Yadav, A. Yadav, R. Fernandes, Y. Popat, M. Orlandi, A. Dashora, D. C. Kothari, A. Miotello, B. L. Ahuja, N. Patel, *J. Environ. Manage.* **2017**, *203*, 364.
[229] H. Tao, X. Liang, Q. Zhang, C. T. Chang, *Appl. Surf. Sci.* **2015**, *324*, 258.
[230] V. Bhatia, G. Malekshoar, A. Dhir, A. K. Ray, *J. Photochem. Photobiol., A* **2017**, *332*, 182.
[231] P. Karaolia, I. Michael-Kordatou, E. Hapeshi, C. Drosou, Y. Bertakis, D. Christofilos, G. S. Armatas, L. Sygellou, T. Schwartz, N. P. Xekoukoulotakis, D. Fatta-Kassinos, *Appl. Catal., B* **2018**, *224*, 810.
[232] D. K. Padhi, T. K. Panigrahi, K. Parida, S. K. Singh, P. M. Mishra, *ACS Sustainble Chem. Eng.* **2017**, *5*, 10551.
[233] S. Mansingh, R. Acharya, S. Martha, K. M. Parida, *Phys. Chem. Chem. Phys.* **2018**, *20*, 9872.
[234] S. Dong, J. Sun, Y. Li, C. Yu, Y. Li, J. Sun, *Appl. Catal., B* **2014**, *144*, 386.
[235] J. Yang, Q. Shi, R. Zhang, M. Xie, X. Jiang, F. Wang, X. Cheng, W. Han, *Carbon* **2018**, *138*, 118.
[236] G. Jiang, Z. Lin, C. Chen, L. Zhu, Q. Chang, N. Wang, W. Wei, H. Tang, *Carbon* **2011**, *49*, 2693.
[237] C. Chen, W. Cai, M. Long, B. Zhou, Y. Wu, D. Wu, Y. Feng, *ACS Nano* **2010**, *4*, 6425.
[238] Q. Luo, B. Chai, M. Xu, Q. Cai, *Appl. Phys. A: Mater. Sci. Process.* **2018**, *124*, 495.
[239] J. Chen, H. Zheng, Y. Zhao, M. Que, W. Wang, X. Lei, *Ceram. Int.* **2020**, *46*, 20088.
[240] Y. Gao, L. Wang, A. Zhou, Z. Li, J. Chen, H. Bala, Q. Hu, X. Cao, *Mater. Lett.* **2015**, *150*, 62.
[241] V. Q. Hieu, T. K. Phung, T. Q. Nguyen, A. Khan, V. D. Doan, V. A. Tran, V. T. Le, *Chemosphere* **2021**, *276*, 130154.
[242] Z. Miao, G. Wang, X. Zhang, X. Dong, *Appl. Surf. Sci.* **2020**, *528*, 146929.
[243] A. Tariq, M. A. Iqbal, S. I. Ali, M. Z. Iqbal, D. Akinwande, S. Rizwan, *ACS Omega* **2019**, *4*, 20530.
[244] D. Zhao, C. Cai, *Inorg. Chem. Front.* **2020**, *7*, 2799.
[245] M. A. Iqbal, S. I. Ali, F. Amin, A. Tariq, M. Z. Iqbal, S. Rizwan, *ACS Omega* **2019**, *4*, 8661.
[246] D. Xu, Y. Ma, J. Wang, W. Chen, Y. Tang, X. Li, L. Li, *Chem. Eng. J.* **2021**, *426*, 131246.
[247] L. Zhang, P. Ma, L. Dai, S. Li, W. Yu, J. Guan, *Catal. Sci. Technol.* **2021**, *11*, 3834.
[248] X. Li, J. Xia, W. Zhu, J. Di, B. Wang, S. Yin, Z. Chen, H. Li, *Colloids Surf., A* **2016**, *511*, 1.
[249] Y. Chen, G. Tian, Y. Shi, Y. Xiao, H. Fu, *Appl. Catal., B* **2015**, *164*, 40.
[250] L. Wang, Y. Chai, J. Ren, J. Ding, Q. Liu, W. L. Dai, *Dalton Trans.* **2015**, *44*, 14625.
[251] C. Zhu, L. Zhang, B. Jiang, J. Zheng, P. Hu, S. Li, M. Wu, W. Wu, *Appl. Surf. Sci.* **2016**, *377*, 99.
[252] X. Liu, Z. Xing, Y. Zhang, Z. Li, X. Wu, S. Tan, X. Yu, Q. Zhu, W. Zhou, *Appl. Catal., B* **2017**, *201*, 119.
[253] J. Wang, B. Wei, L. Xu, H. Gao, W. Sun, J. Che, *Mater. Lett.* **2016**, *179*, 42.
[254] G. P. Awasthi, S. P. Adhikari, S. Ko, H. J. Kim, C. H. Park, C. S. Kim, *J. Alloys Compd.* **2016**, *682*, 208.
[255] R. Rathnasamy, M. Santhanam, V. Alagan, *Mater. Sci. Semicond. Process.* **2018**, *85*, 59.
[256] D. Wu, X. Wang, H. Wang, F. Wang, D. Wang, Z. Gao, X. Wang, F. Xu, K. Jiang, *J. Colloid Interface Sci.* **2019**, *533*, 539.
[257] R. A. Senthil, S. Osman, J. Pan, Y. Sun, T. R. Kumar, A. Manikandan, *Ceram. Int.* **2019**, *45*, 18683.
[258] X. Lin, X. Wang, Q. Zhou, C. Wen, S. Su, J. Xiang, P. Cheng, X. Hu, Y. Li, X. Wang, X. Gao, R. Nözel, G. Zhou, Z. Zhang, J. Liu, *ACS Sustainable Chem. Eng.* **2019**, *7*, 1673.
[259] S. Thangavel, S. Thangavel, N. Raghavan, R. Alagu, G. Venugopal, *J. Phys. Chem. Solids* **2017**, *110*, 266.
[260] W. P. C. Lee, F. H. Wong, N. K. Attenborough, X. Y. Kong, L. L. Tan, S. Sumathi, S. P. Chai, *J. Environ. Manage.* **2017**, *197*, 63.
[261] B. Ren, W. Shen, L. Li, S. Wu, W. Wang, *Appl. Surf. Sci.* **2018**, *447*, 711.

© 2024 The Author(s). Advanced Sustainable Systems published by Wiley-VCH GmbH

23667486, 2024, 12, Downloaded from https://advanced.onlinelibrary.wiley.com/doi/10.1002/adsu.202400483 by Nazarbayev University, Wiley Online Library on [08/07/2025]. See the Terms and Conditions (https://onlinelibrary.wiley.com/terms-and-conditions) on Wiley Online Library for rules of use; OA articles are governed by the applicable Creative Commons License

[262] Z. Ma, L. Hu, X. Li, L. Deng, G. Fan, Y. He, *Ceram. Int.* **2019**, *45*, 15824.
[263] U. Krishnan, M. Kaur, G. Kaur, K. Singh, A. R. Dogra, M. Kumar, A. Kumar, *Mater. Res. Bull.* **2019**, *111*, 212.
[264] J. Hasan, H. Li, G. Tian, C. Qin, *Chem. Phys.* **2020**, *539*, 110950.
[265] N. Lu, P. Wang, Y. Su, H. Yu, N. Liu, X. Quan, *Chemosphere* **2019**, *215*, 444.
[266] X. Wang, A. Wang, J. Ma, *J. Hazard. Mater.* **2017**, *336*, 81.
[267] N. S. Hassan, A. A. Jalil, N. F. Khusnun, M. W. Ali, S. Haron, *J. Alloys Compd.* **2019**, *789*, 221.
[268] J. Ni, J. Xue, L. Xie, J. Shen, G. He, H. Chen, *Phys. Chem. Chem. Phys.* **2017**, *20*, 414.
[269] Q. Wei, Y. Wang, H. Qin, J. Wu, Y. Lu, H. Chi, F. Yang, B. Zhou, H. Yu, J. Liu, *Appl. Catal., B* **2018**, *227*, 132.
[270] F. Chen, W. An, Y. Li, Y. Liang, W. Cui, *Appl. Surf. Sci.* **2018**, *427*, 123.
[271] Y. Wang, K. Ding, R. Xu, D. Yu, W. Wang, P. Gao, B. Liu, *J. Cleaner Prod.* **2020**, *247*, 119108.
[272] G. S. Sree, S. M. Botsa, B. J. M. Reddy, K. V. B. Ranjitha, *Arab. J. Chem.* **2020**, *13*, 5137.
[273] A. Gomathi, T. Prabhuraj, S. Gokilapriya, G. Vasanthi, P. Maadeswaran, K. A. Ramesh Kumar, *Dyes Pigm.* **2023**, *218*, 111473.
[274] K. Ding, D. Yu, W. Wang, P. Gao, B. Liu, *Appl. Surf. Sci.* **2018**, *445*, 39.
[275] L. Xu, Y. Wei, W. Guo, Y. Guo, Y. Guo, *Appl. Surf. Sci.* **2015**, *332*, 682.
[276] Z. Zhu, Y. Li, C. Wang, L. Liang, D. Yu, J. Sun, P. Gao, B. Liu, *Mater. Lett.* **2018**, *227*, 296.
[277] S. Kumar, R. Sharma, V. Sharma, G. Harith, V. Sivakumar, V. Krishnan, *Beilstein J. Nanotechnol.* **2016**, *7*, 1684.
[278] N. Prabhakarrao, M. R. Chandra, T. S. Rao, *J. Alloys Compd.* **2017**, *694*, 596.
[279] S. Ghasemi, S. J. Hashemian, A. A. Alamolhoda, I. Gocheva, S. R Setayesh, *Mater. Res. Bull.* **2017**, *87*, 40.
[280] N. T. V. Hoan, N. N. Minh, T. T. K. Nhi, N. Van Thang, V. A. Tuan, V. T. Nguyen, N. M. Thanh, N. Van Hung, D. Q. Khieu, *J. Nanomater.* **2020**, *2020*, 350125.
[281] Y. Lu, M. Yao, A. Zhou, Q. Hu, L. Wang, *J. Nanomater.* **2017**, *2017*, 978764.
[282] B. Sun, F. Tao, Z. Huang, W. Yan, Y. Zhang, X. Dong, Y. Wu, G. Zhou, *Appl. Surf. Sci.* **2021**, *535*, 147354.
[283] X. Ding, Y. Li, C. Li, W. Wang, L. Wang, L. Feng, D. Han, *J. Mater. Sci.* **2019**, *54*, 9385.
[284] Z. Wu, Y. Liang, X. Yuan, D. Zou, J. Fang, L. Jiang, J. zhang, H. Yang, Z. Xiao, *J. Chem. Eng.* **2020**, *394*, 124921.
[285] Q. Liu, X. Tan, S. Wang, F. Ma, H. Znad, Z. Shen, L. Liu, S. Liu, *Environ. Sci.: Nano* **2019**, *6*, 3158.
[286] A. A. Alothman, M. R. Khan, M. D. Albaqami, S. Mohandoss, Z. A. Alothman, N. Ahmad, K. N. Alqahtani, *Nanomaterials* **2023**, *13*, 3026.
[287] S. M. Lam, M. K. Choong, J. C. Sin, H. Zeng, L. Huang, L. Hua, H. Li, Z. H. Jaffari, K. H. Cho, *J. Environ. Chem. Eng.* **2022**, *10*, 108284.
[288] Q. Tan, Z. Yu, R. Long, N. He, Y. Huang, Y. Liu, *Opt. Mater.* **2022**, *131*, 112685.
[289] M. Ding, W. Ao, H. Xu, W. Chen, L. Tao, Z. Shen, H. Liu, C. Lu, Z. Xie, *J. Hazard. Mater.* **2021**, *420*, 126686.
[290] T. Wojciechowski, A. Rozmysłowska-Wojciechowska, G. Matyszczak, M. Wrzecionek, A. Olszyna, A. Peter, A. Mihaly-Cozmuta, C. Nicula, L. Mihaly-Cozmuta, S. Podsiadło, D. Basiak, W. Ziemkowska, A. Jastrzębska, *Inorg. Chem.* **2019**, *58*, 7602.
[291] Y. Pajouhan, S. Sabbaghi, S. Sabbaghi, K. Rasouli, J. Rasouli, W. Dastyar, E. Andiroglu, E. Andiroglu, *Process Saf. Environ. Prot.* **2024**, *190*, 1149.
[292] H. Yang, J. Lin, Z. Wen, Z. Li, J. Zeng, L. Wang, Y. Tao, D. Gao, D. Wang, *Chemosphere* **2023**, *339*, 139797.
[293] H. Wang, Y. Wu, T. Xiao, X. Yuan, G. Zeng, W. Tu, S. Wu, H. Y. Lee, Y. Z. Tan, J. W. Chew, *Appl. Catal., B* **2018**, *233*, 213.
[294] S. Kumar, V. Sharma, K. Bhattacharyya, V. Krishnan, *New J. Chem.* **2016**, *40*, 5185.
[295] W. K. Jo, T. Adinaveen, J. J. Vijaya, N. C. Sagaya Selvam, *RSC Adv.* **2016**, *6*, 10487.
[296] C. Liu, J. Chen, H. Che, K. Huang, P. A. Charpentier, W. Z. Xu, W. Shi, H. J. Dong, *RSC Adv.* **2017**, *7*, 8429.
[297] S. V. P. Vattikuti, C. Byon, *Mater. Res. Bull.* **2017**, *96*, 233.
[298] J. Wang, J. Jin, X. Wang, S. Yang, Y. Zhao, Y. Wu, S. Dong, J. Sun, J. Sun, *J. Colloid Interface Sci.* **2017**, *505*, 805.
[299] J. Kang, C. Jin, Z. Li, M. Wang, Z. Chen, Y. Wang, *J. Alloys Compd.* **2020**, *825*, 153975.
[300] M. Liu, X. Xue, S. Yu, X. Wang, X. Hu, H. Tian, H. Chen, W. Zheng, *Sci. Rep.* **2017**, *7*, 3637.
[301] S. Sun, M. Sun, Y. Kong, Y. Fang, Y. Yao, *J. Sol-Gel Sci. Technol.* **2016**, *80*, 719.
[302] M. Jahurul Islam, D. Amaranatha Reddy, N. S. Han, J. Choi, J. K. Song, T. K. Kim, *Phys. Chem. Chem. Phys.* **2016**, *18*, 24984.
[303] A. Gopalakrishnan, S. Pratap Singh, S. Badhulika, *ChemistrySelect* **2020**, *5*, 1997.
[304] N. Shao, J. Wang, D. Wang, P. Corvini, *Appl. Catal., B* **2017**, *203*, 964.
[305] A. Priyadharsan, S. Shanavas, V. Vasanthakumar, B. Balamuralikrishnan, P. M. Anbarasan, *Colloids Surf., A* **2018**, *559*, 43.
[306] Y. Yu, J. Wan, Z. Yang, Z. Hu, *J. Colloid Interface Sci.* **2017**, *502*, 100.
[307] M. Karpuraranjith, Y. Chen, S. Rajaboopathi, M. Ramadoss, K. Srinivas, D. Yang, B. Wang, *J. Colloid Interface Sci.* **2022**, *605*, 613.
[308] Y. Zhang, S. He, Z. He, Y. Zhang, Y. Feng, Y. Wang, M. Zhang, *Int. J. Electrochem. Sci.* **2022**, *17*, 220210.
[309] Y. Zhang, Z. Zhang, Y. Zhang, Y. Li, Y. Yuan, *J. Colloid Interface Sci.* **2023**, *651*, 117.
[310] A. Kusior, K. Michalec, P. Jelen, M. Radecka, *Appl. Surf. Sci.* **2019**, *476*, 342.
[311] J. Zwara, E. Grabowska, T. Klimczuk, W. Lisowski, A. Zaleska-Medynska, *J. Photochem. Photobiol., A* **2018**, *367*, 240.
[312] D. Monga, S. Basu, *J. Powder Technol.* **2019**, *30*, 1089.
[313] S. Sharma, K. Kumar, N. Thakur, S. Chauhan, M. S. Chauhan, *Bull. Mater. Sci.* **2020**, *43*, 20.
[314] S. B. Khan, M. Hou, S. Shuang, Z. Zhang, *Appl. Surf. Sci.* **2017**, *400*, 184.
[315] M. Farhadian, P. Sangpout, G. Hosseinzadeh, *Energy Chem.* **2015**, *24*, 171.
[316] A. Mclaren, T. Valdes-Solis, G. Li, S. C. Tsang, *J. Am. Chem. Soc.* **2009**, *131*, 12540.
[317] H. Zhang, H. Zhang, P. Zhu, F. Huang, *ChemistrySelect* **2017**, *2*, 3282.
[318] T. D. Nguyen-Phan, E. W. Shin, *Ind. Eng. Chem. Res.* **2011**, *17*, 397.
[319] A. E. Cassano, O. M. Alfano, *Catal. Today* **2000**, *58*, 167.
[320] Z. Xie, X. Liu, W. Wang, C. Liu, Z. Li, Z. Zhang, *Sci. Technol. Adv. Mater.* **2014**, *15*, 055006.
[321] B. Y. Balarabe, P. Maity, *Colloids Surf., A* **2022**, *655*, 130247.
[322] K. Li, F. Zhang, H. Wang, Y. Zhou, L. Zhao, J. Du, Y. Gao, W. Wang, D. J. Kang, *Nano* **2018**, *13*, 1850110.
[323] O. Sacco, V. Vaiano, D. Sannino, *J. Chem. Technol. Biotechnol.* **2020**, *95*, 2608.
[324] L. Lin, H. Wang, P. Xu, *J. Chem. Eng.* **2017**, *310*, 389.
[325] S. Bhandari, J. Vardia, R. K. Malkani, S. C. Ameta, *Toxicol. Environ. Chem.* **2006**, *88*, 35.
[326] S. Rani, M. Aggarwal, M. Kumar, S. Sharma, D. Kumar, *Water Sci.* **2016**, *30*, 51.
[327] R. Uma, K. Ravichandran, S. Sriram, B. Sakthivel, *Mater. Chem. Phys.* **2017**, *201*, 147.

© 2024 The Author(s). Advanced Sustainable Systems published by Wiley-VCH GmbH

23667486, 2024, 12, Downloaded from https://advanced.onlinelibrary.wiley.com/doi/10.1002/adsu.202400483 by Nazarbayev University, Wiley Online Library on [08/07/2025]. See the Terms and Conditions (https://onlinelibrary.wiley.com/terms-and-conditions) on Wiley Online Library for rules of use; OA articles are governed by the applicable Creative Commons License

[328] J.-Y. Li, M. A. Wan-Hong, L. Peng-Xiang, J.-C. Zhao, *J. Environ. Sci.* **2007**, *19*, 892.
[329] S. Zhou, Z. Du, X. Li, Y. Zhang, Y. He, Y. Zhang, *R. Soc. Open Sci.* **2019**, *6*, 190351.
[330] A. Ajmal, I. Majeed, R. N. Malik, H. Idriss, M. A. Nadeem, *RSC Adv.* **2014**, *4*, 37003.
[331] C. R. Minitha, M. Lalitha, Y. L. Jeyachandran, L. Senthilkumar, R. T. Rajendra Kumar, *Mater. Chem. Phys.* **2017**, *194*, 243.
[332] H. Anwer, J. W. Park, *J. Hazard. Mater.* **2018**, *358*, 416.
[333] Y. Yuan, P. Shen, Q. Li, G. Chen, H. Zhang, L. Zhu, B. Zou, B. Liu, *J. Alloys Compd.* **2017**, *700*, 12.
[334] W. Zhang, C. Hu, W. Zhai, Z. Wang, Y. Sun, F. Chi, S. Ran, X. Liu, Y. Lv, *Mater. Res.* **2016**, *19*, 673.
[335] Y. Yuan, R.-t. Guo, L.-f. Hong, X.-y. Ji, Z.-s. Li, Z.-d. Lin, W.-g. Pan, *Colloids Surf., A* **2021**, *611*, 125836.
[336] G. Zhou, X. Xu, J. Yu, B. Feng, Y. Zhang, J. Hu, Y. Zhou, *CrystEngComm* **2014**, *16*, 9025.
[337] N. Mzimela, S. Tichapondwa, E. Chirwa, *RSC Adv.* **2022**, *12*, 34652.
[338] N. Fiol, I. Villaescusa, *Environ. Chem. Lett.* **2009**, *7*, 79.
[339] N. Saha, M. Volpe, L. Fiori, R. Volpe, A. Messineo, M. T. Reza, *Energies* **2020**, *13*, 4686.
[340] H. N. Tran, S. J. You, H. P. Chao, *Waste Manage. Res.* **2016**, *34*, 129.
[341] J. Wang, S. Dong, T. Guo, J. Jin, J. Sun, *Mater. Lett.* **2017**, *191*, 22.
[342] B. Y. Balarabe, M. N. Illiassou Oumarou, A. S. Koroney, I. Adjama, A. R. Ibrahim Baraze, *J. Nanotechnol.* **2023**, *2023*, 1292762.
[343] A. Soufi, H. Hajjaoui, R. Elmoubarki, M. Abdennouri, S. Qourzal, N. Barka, *Appl. Surf. Sci.* **2022**, *9*, 100251.
[344] S.-m. Fu, G.-s. Li, X. Wen, C.-m. Fan, J.-x. Liu, X.-c. Zhang, R. Li, *Trans. Nonferrous Met. Soc. China* **2020**, *30*, 765.
[345] M. Bellardita, A. Di Paola, B. Megna, L. Palmisano, *Appl. Catal., B* **2017**, *201*, 150.
[346] Y. Zhang, Z. R. Tang, X. Fu, Y. J. Xu, *ACS Nano* **2011**, *5*, 7426.
[347] N. Zhang, Y. Zhang, Y. J. Xu, *Nanoscale* **2012**, *4*, 5792.
[348] P. Ribao, M. J. Rivero, I. Ortiz, *Environ. Sci. Pollut. Res. Int.* **2018**, *25*, 34893.
[349] P. Murugesan, J. A. Moses, C. Anandharamakrishnan, *J. Mater. Sci.* **2019**, *54*, 12206.
[350] Z. Teng, N. Yang, H. Lv, S. Wang, M. Hu, C. Wang, D. Wang, G. Wang, *Chem* **2019**, *5*, 664.
[351] W. Wang, Q. Han, Z. Zhu, L. Zhang, S. Zhong, B. Liu, *Adv. Powder Technol.* **2019**, *30*, 1882.
[352] Y. Chen, G. Wang, H. Li, F. Zhang, H. Jiang, G. Tian, *J. Colloid Interface Sci.* **2019**, *555*, 214.

Bachir Yaou Balarabe is a postdoctoral fellow at Department of Chemistry of Nazarbayev University, Kazakhstan. He completed his Ph.D. at the National Forensic Sciences University in India, where he focused on developing efficient catalytic strategies for environmental remediation. His research focuses on development of advanced nanocomposites for organic pollutants removal in water bodies. He is currently a senior researcher working on a project aimed at developing efficient 2D-TiO_2 photocatalytic structures.

Timur Sh. Atabaev earned his Ph.D. degree in 2012 at Pusan National University (South Korea) under the supervision of Prof. Hyung Kook Kim and Prof. Yoon-Hwae Hwang. From 2012 to 2017, he employed as a postdoctoral scholar and research professor at Seoul and Pusan National Universities. He joined Nazarbayev University as an assistant professor in 2017 and was promoted to associate professor in 2022. His research focuses on advanced nanostructures for biomedical, optical, energy, sensing, and photocatalytic applications. He is a member of the American Chemical Society (ACS) and Materials Research Society (MRS).

© 2024 The Author(s). Advanced Sustainable Systems published by Wiley-VCH GmbH

23667486, 2024, 12, Downloaded from https://advanced.onlinelibrary.wiley.com/doi/10.1002/adsu.202400483 by Nazarbayev University, Wiley Online Library on [08/07/2025]. See the Terms and Conditions (https://onlinelibrary.wiley.com/terms-and-conditions) on Wiley Online Library for rules of use; OA articles are governed by the applicable Creative Commons License